Candela Vidal-Abarca Garrido

"MATERIALES PARA BATERÍAS DE IÓN LITIO E IÓN SODIO: ÓXIDOS MIXTOS PARA ÁNODOS DE CONVERSIÓN Y FOSFATOS PARA CÁTODOS DE INSERCIÓN"

Tesis doctoral

DIRECTORES

Dr. D. José Luis Tirado Coello

Catedrático de Universidad

Dr. D. Pedro Lavela Cabello

Profesor Titular

DEPARTAMENTO DE QUÍMICA INORGÁNICA E INGENIERÍA QUÍMICA

UNIVERSIDAD DE CÓRDOBA

2012

D. José Luis Tirado Coello, Catedrático de Universidad, y D. Pedro Lavela Cabello, Profesor Titular, miembros del Departamento de Química Inorgánica e Ingenieria Química, y en la calidad de la Tesis Doctoral presentada por Candela Vidal-Abarca Garrido.

CERTIFICAN: Que la Tesis Doctoral titulada **"MATERIALES PARA BATERÍAS DE IÓN LITIO E IÓN SODIO: ÓXIDOS MIXTOS PARA ÁNODOS DE CONVERSIÓN Y FOSFATOS PARA CÁTODOS DE INSERCIÓN"** ha sido desarrollada en los laboratorios del Departamento de Química Inorgánica e Ingeniería Química de la Universidad de Córdoba, y que a su juicio reúne todos los requisitos exigidos a este tipo de trabajo.

Y para que conste y surta efectos oportunos, expiden el presente certificado en la ciudad de Córdoba a 15 de Marzo de 2012.

Firmas:

Dr. D. José Luis Tirado Coello Dr. D. Pedro Lavela Cabello

Mediante la defensa de esta memoria se pretende optar a la obtención de la **mención de "Doctorado Internacional"**, habida cuenta que el doctorando reúne los requisitos exigidos para tal mención:

1. Se cuenta con los informes favorables de dos doctores pertenecientes a instituciones de Enseñanza Superior, o instituto de investigación, de países europeos distintos al nuestro.

2. En el Tribunal, que ha de evaluar la Tesis, existe un miembro de un centro de Enseñanza Superior de un país europeo distinto al nuestro.

3. Parte de la redacción y defensa de la Memoria se realizará en la lengua oficial de un país europeo distinto al nuestro.

4. El doctorando ha realizado una parte del trabajo experimental en las instalaciones del LRCS de Amiens (Francia). Esta estancia, de un trimestre de duración, se ha realizado gracias a la concesión de ayuda para estancias breves en el extranjero asociada a la beca de Formación de Personal de Investigación del Ministerio de Ciencia e Innovación.

El trabajo que engloba la presente Memoria se ha realizado durante el periodo de disfrute de una Beca de Formación de Personal Investigador del Ministerio de Ciencia e Innovación, asociada al proyecto "Oxisales para los electrodos de inserción/conversión de baterías de ión litio e ión sodio" MAT2008-05880"

Informe del Journal Citation Report

Los artículos que se exponen en la presente memoria han sido publicados en revistas cuya información de impacto según el Journal Citation Reports de ISI web of Knowledge del último año están recogidos en la siguiente tabla:

Journal	Impact factor	Category	Total Journals in Category	Journal Rank in Category	Quartile in Category
Solid State Ionics	2.496	Chemistry, Physical	127	51	Q2
		Physics, Condensed Matter	68	16	Q1
Journal of Physical Chemistry C	4.524	Chemistry, Physical	127	27	Q1
		Materials Science, Multidisciplainary	225	22	Q1
		Nanoscience & Technology	64	14	Q1
Journal of Power Sources	4.290	Electrochemistry	26	2	Q1
		Energy & Fuels	79	10	Q1
Electrochimica Acta	3.650	Electrochemistry	25	5	Q1

"MATERIALES PARA BATERÍAS DE IÓN LITIO E IÓN SODIO: ÓXIDOS MIXTOS PARA ÁNODOS DE CONVERSIÓN Y FOSFATOS PARA CÁTODOS DE INSERCIÓN"

Trabajo presentado para aspirar al grado de Doctor en Química por:

Candela Vidal-Abarca Garrido

Dirigido por:

Dr. D. José Luis Tirado Coello

Dr. D. Pedro Lavela Cabello

AGRADECIMIENTOS

Me gustaría expresar mi más profunda gratitud a los directores de la tesis, los profesores. D. José Luis Tirado Coello y D. Pedro Lavela Cabello por ofrecerme la posibilidad de realizar la presente tesis doctoral y por sus pautas a la hora de desarrollar mi trabajo.

Agradezco enormemente a todas las personas e instituciones que han contribuido a la realización de esta tesis.

Al departamento de Química Inorgánica e Ingeniería Química, que me ha permitido realizar mi labor investigadora y formar parte de él como estudiante de postgrado.

A las diferentes instituciones que han financiado este trabajo: Ministerio de Ciencia e Innovación (proyecto MAT2008-05880) y Junta de Andalucía a través del grupo de investigación FQM-288 del plan Andaluz de investigación y de los proyectos de excelencia FQM6017 y FQM1447.

A los servicios centrales de Apoyo a la Investigación (SCAI) de la Universidad de Córdoba.

Al Dr. Alan Chadwick y la Dra. Maria Alfredsson de la Universidad de Kent (Canterbury, Reino Unido) y al Dr. Erik Kelder de la Universidad de Delf (Holanda) por su ayuda en la realización e interpretación de las medidas de Absorción de Rayos X.

Al Dr. Christian Masquelier y a Jean Marcel Ateba de la Universidad de Picardie Jules Verne (Amiens, Francia) por su confianza en mis habilidades, sus sugerencias y ayuda durante la realización de mi estancia en LRCS "Laboratoire de Reactivité et Chimie des Solides" de Amiens.

Un agradecimiento especial a los compañeros del laboratorio de Química Inorgánica, al Dr. Ricardo Alcántara Román, al Dr. Carlos Pérez Vicente por resolver muchas de mis dudas teóricas, al Dr. Gregorio Ortiz, a la Dra. Inés Rodríguez Sánchez, al Dr. Bernardo León, a la Dra. Mª José Aragón Algarra, a Mª Carmen Mohedano Campos, a Francisco José Nacimiento Cobos, a Mayka Zafra, a José Ramón González Jiménez y a Carmen López Luna.

Mi más sincero agradecimiento a Shadi Mirhashemi Haghighi, Nareerat Plylahan y Marina Sierra Rodero por los maravillosos momentos compartidos durante tantos desayunos y almuerzos, por escucharme y aconsejarme en el largo camino de la experiencia doctoral.

A todos los colegas del departamento de Química Inorgánica e Ingeniería Química que no he mencionado por su presencia y buena compañía.

Un agradecimiento muy especial a mis amigos y familia que aún sin entender nada nunca dejaron de preguntar *qué tal iban mis pilas* y de animarme en todo momento.

El agradecimiento más exclusivo a Rosauro, fundamento de mi motivación para superarme cada día, y porque pese a la distancia física que nos ha separado he sentido intensamente su apoyo, amor y aliento cada segundo durante todos estos años.

No hay suficientes palabras de agradecimiento para mi madre y mi padre, mi tía Ana y mi hermana por su educación en la vida, el amor y el trabajo, por sus esfuerzos por ayudarme y comprenderme y por ser tan increíbles.

A mi padre

ÍNDICE

Capítulo 1

Introducción

La energía ha demostrado ser el sustento fundamental para el desarrollo de la sociedad moderna. El aprovechamiento de la energía y la búsqueda de energías limpias exigen el desarrollo de sistemas de almacenamiento energético de alto rendimiento, versátiles y de bajo coste. Las baterías poseen características muy adecuadas para satisfacer dichos requisitos. Entre los diversos sistemas que se desarrollan actualmente, las baterías de ión litio parecen ser las más prometedoras. Los años de investigación en este campo están consiguiendo baterías de ión litio de elevada densidad de energía, bajo peso y buena ciclabilidad. En la actualidad ya se comercializan algunas baterías de ión litio para su uso en pequeños aparatos electrónicos y grandes esfuerzos se están llevando a cabo para el desarrollo de sistemas de almacenamiento para vehículos o compensadores de carga basados en la electroquímica del litio.[1]

Sin embargo algunos autores en los últimos años han señalado la importancia de desarrollar paralelamente las baterías de ión sodio debido a la gran abundancia terrestre y el coste extracción y producción de dicho elemento en comparación con el litio cuyas reservas disminuyen o se encuentran en áreas geográficas sensibles en términos políticos.[2,3]

1.1 Celda electroquímica

Una celda electroquímica es un dispositivo que convierte la energía química contenida en sus materiales activos directamente en energía eléctrica por medio de una reacción redox. Para aplicaciones tecnológicas de interés se requiere que la reacción sea reversible, como ocurre en las celdas de ión-litio actuales. Las celdas se pueden ensamblar en serie o en paralelo para obtener el voltaje o la capacidad requeridos en una

aplicación determinada. De este modo se obtiene una batería. La celda electroquímica consta de tres componentes principales, el ánodo o electrodo negativo, el cátodo o electrodo positivo y el electrólito. En un proceso habitual de descarga, el cátodo sufre una reducción y el ánodo una oxidación de parte de sus elementos químicos constitutivos. Contrariamente, se produce la reacción inversa durante la carga.[4] El electrólito debe ser un buen conductor iónico y aislante eléctrico

Los procesos redox que ocurren dentro de la celda electroquímica están representados en la figura 1.1.

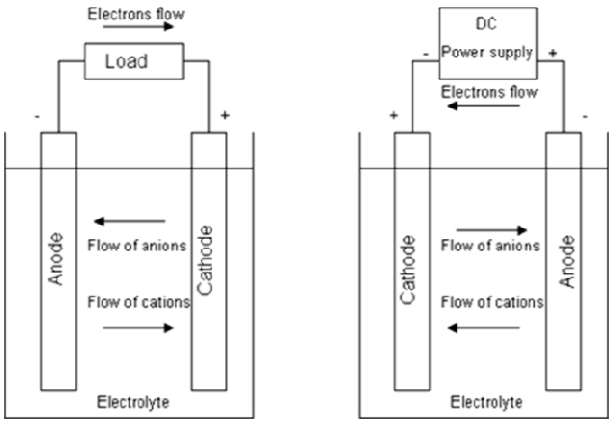

Figura 1.1 Operación electroquímica de una celda durante la descarga (a la izquierda) y durante la carga (a la derecha).

La cantidad de energía eléctrica, o densidad de energía, ya sea expresado por unidad de peso ($Wh.Kg^{-1}$) o por unidad de volumen ($Wh.L^{-1}$), que una batería es capaz de generar es una función del potencial de la pila (V) y la capacidad ($Ah.Kg^{-1}$), ambos ligados directamente a la química del sistema.[5]

El litio metálico combina un potencial redox muy negativo con un peso equivalente bajo, lo cual lo convierte en un candidato muy atractivo

para los electrodos negativos de baterías de alta densidad de energía. Combinado con un material de electrodo positivo, como un óxido de metal de transición o calcogenuro, capaz de insertar litio de manera reversible (por ejemplo, MnO_2, MoS_2, o TiS_2) forman una batería recargable de litio.

El electrodo positivo generalmente exhibe ciclabilidad suficiente debido al mecanismo de inserción reversible, pero la disolución periódica y la deposición de litio metálico durante el ciclo del electrodo negativo formando dendritas es un problema grave. El ciclo de litio metálico está asociado con cambios en la forma, y se producen reacciones colaterales también con el electrolito (corrosión de litio). Dichas reacciones generan problemas importantes de seguridad y reducen el número de ciclos de los electrodos de litio metálico de forma significativa. La sustitución del litio metálico por compuestos de inserción de litio en su forma iónica en la década de 1980 ha dado lugar a las baterías de ión litio.[6]

1.1.1 *Baterías de ión litio*

En este concepto, el litio sólo aparece en su forma iónica en movimiento desde el ánodo al cátodo durante la descarga y en sentido inverso, desde el cátodo al ánodo, durante el proceso de carga. La empresa Sony Energytech desarrolló la primera patente de baterías de ión litio y las comercializó en 1993.[7]

Una batería de ión litio clásica contiene $LiCoO_2$ como electrodo positivo, un material basado en carbono como electrodo negativo, y un electrólito no acuoso, teniendo un voltaje medio de aproximadamente 3,7 V.[8] En la

figura 1.2 se muestra el esquema del funcionamiento de una batería de ión litio.

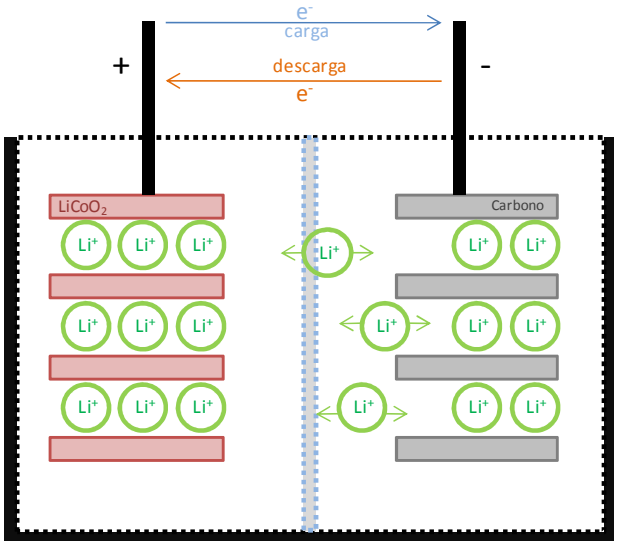

Figura 1.2. Funcionamiento batería ion litio comercial.

La densidad de energía gravimétrica (~150$Wh.kg^{-1}$) y la densidad de energía volumétrica (~400$Wh.L^{-1}$) de las baterías de ion litio son superiores a otras baterías recargables tradicionales como las de Plomo/Acido, Níquel/Cadmio y Níquel/Hidruro metálico por lo tanto son buenas candidatas para aplicaciones que estén limitadas por peso o volumen. Además, las baterías de ion litio ofrecen una baja auto-descarga (2% a 8% al mes), larga vida en ciclos (largo (más de 1000 ciclos) y una amplia gama de temperaturas de operación (en carga de -20 ° C a 60 ° C, en descarga de -40 ° C a 65 ° C), lo que permite su utilización en una amplia variedad de aplicaciones.[5]

La figura 1.3 muestra la capacidad frente al potencial de algunos de los materiales más representativos para electrodos positivos y negativos que se utilizan actualmente o se consideran para su uso en baterías recargables de ión litio. Se representan los voltajes de celda tanto para las baterías de ión litio como para las baterías de litio metal ya que la

enorme diferencia en la capacidad entre el litio metal y otros electrodos negativos es la razón por la cual sigue habiendo un gran interés en buscar una solución del problema de crecimiento de dendritas en el caso de las baterías de litio. Se puede observar que la sustitución del electrodo de grafito, el cual opera por debajo de 1.0 *V*, por otros materiales anódicos implica el uso de materiales para cátodos que presenten potenciales mayores a $LiCoO_2$ con el fin de no disminuir el potencial global de la batería.

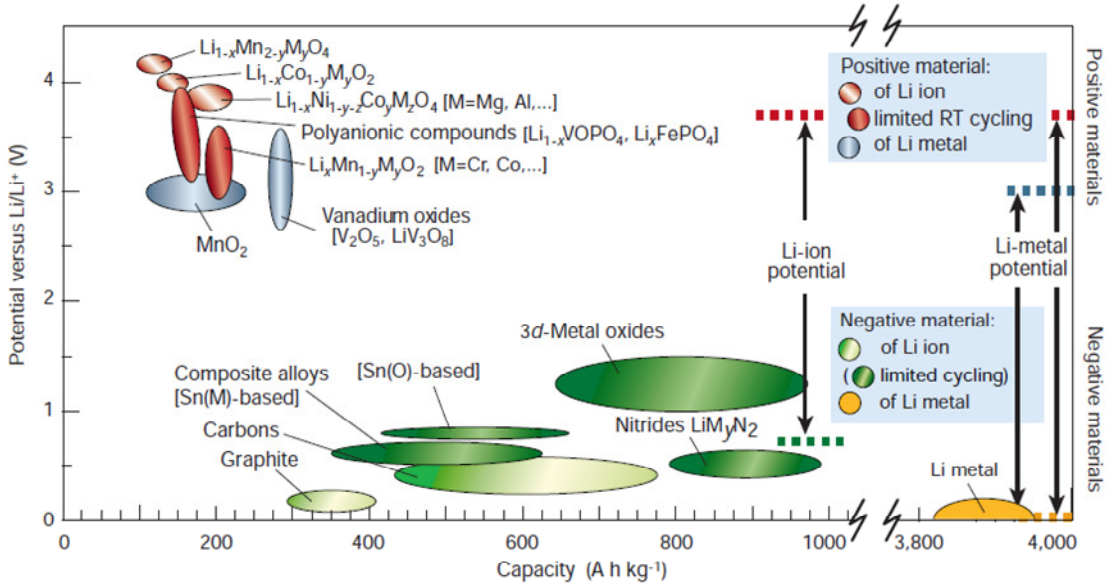

Figura 1.3. Esquema que muestra los principales tipos de materiales usados o potencialmente utilizables como materiales activos de electrodos en baterías de ión litio.[6]

1.1.2 *Baterías de ión sodio*

Las baterías que sustituyen los compuestos basados en litio por sodio son llamadas baterías de ión sodio. Dichas baterías se han concebido como una alternativa prometedora a las celdas de ión litio ya que el coste actual, la accesibilidad y el impacto ambiental de la extracción y

producción de litio son cuestiones bajo debate reciente. Sin embargo, los electrodos de sodio han mostrado propiedades de ciclabilidad deficientes lo cual podría limitar sus aplicaciones.

Dos décadas atrás, el concepto de las baterías de ión sodio como una alternativa a las baterías de ión litio fue discutido por Doeff et al.[3]. Al respecto $NaCoO_2$ (el análogo de $LiCoO_2$) fue estudiado a fondo como material para electrodo positivo en celdas de ión sodio utilizando carbono[9,10] y óxidos de conversión[11] como materiales para ánodos. Recientemente, Ellis et al.[4] han publicado un fosfato de hierro de sodio / litio, A_2FePO_4F (A = Na, Li) que podría servir como un cátodo en baterías tanto de ión litio como de ión sodio. El uso de líquidos iónicos por el grupo de Tarascon ha dado resultados interesantes en la preparación de fluorofosfatos de sodio por vía ionotermal cómo Na_2FePO_4F para su uso como cátodo.[12]

1.2 Materiales anódicos

El material anódico más ampliamente utilizado en las baterías de ión litio desde principio de la década de 1990 está constituido por algún derivado modificado de manera física o química del carbono como el coque, grafito o los carbones duros.[13] Dichos materiales tienen un coste relativamente bajo y las reacciones con el litio han sido considerablemente estudiadas. La reacción de intercalación del litio en el grafito se puede escribir de la siguiente forma

$$xLi^+ + xe^- + C_6 = Li_xC_6 \qquad 0 \leq x \leq 1,$$

Lográndose una capacidad teórica máxima para los electrodos de grafito de 372 $mAh.g^{-1}$ cuando x=1.

El proceso de intercalación de litio en el grafito se produce a un potencial menor a 1.0 V frente al par redox Li^+/Li^0. A este potencial tan bajo, se puede producir la reducción de electrólito, acompañada de la formación de una capa pasivante sobre la superficie del grafito. La formación de esta capa es esencial para el funcionamiento de los electrodos de grafito, así como también inhibe su exfoliación. Pero el hecho de que la mayoría del litio se intercale en el grafito a potenciales menores a 100 mV frente al Li^+/Li^0, hace que el litio altamente reactivo, pueda depositarse sobre la superficie del grafito, generando serios problemas de seguridad en la batería.[14]

La búsqueda de materiales anódicos alternativos con el objetivo de superar los problemas asociados a los materiales basados en el carbono ha conducido al uso de los elementos (Al, Si, Zn, Sn, Sb…) que forman aleaciones y/o compuestos intermetálicos con litio de forma reversible según la reacción general:

$$xM + yLi = Li_yM_x$$

En la mayor parte de estos materiales no se obtienen capacidades muy superiores a las del grafito. No obstante, el principal problema asociado al uso de ánodos de aleaciones de litio reside en las variaciones de volumen en el electrodo que se producen en los procesos de carga y descarga, generando tensiones en el material electródico que se convierten en fracturas y terminan con la vida útil de la batería.

Asimismo también han sido propuestos como materiales anódicos alternativos para las baterías de ión litio, óxidos y oxisales de metales de

transición que no reaccionan con el litio por los procesos clásicos de inserción-deinserción de litio o por aleación sino que reaccionan mediante un proceso de conversión.[6]

1.2.1 *Materiales anódicos de conversión*

Óxidos de metales de transición tales como CoO[15], FeO[16], CuO[17], han sido extensamente investigados. Dichos materiales pueden mostrar capacidades 2 ó 3 veces superiores a las del grafito con un 100% de la retención de la capacidad hasta 100 ciclos. Además, las reacciones de conversión también las presentan otros aniones como sulfuros,[18] nitruros [19] y oxisales del tipo $MnCO_3$,[20] y oxalatos como FeC_2O_4,[21] CoC_2O_4.[22]

La posibilidad de reducir completamente el metal de transición desde el estado iónico inicial hasta su estado metálico de manera reversible durante el proceso de carga-descarga de la batería es la principal ventaja de dichos compuestos. En el caso de la ferrita $NiFe_2O_4$, ocho electrones son intercambiados durante el proceso electroquímico de carga y descarga a través de la siguiente reacción.[23]

$$NiFe_2O_4 + 8Li^+ + 8e^- = Ni^0 + 2Fe^0 + 4Li_2O,$$

La reacción con el litio conlleva la completa degradación estructural del óxido de partida resultando en la formación de agregados de nanopartículas metálicas embebidas en una matriz de Li_2O. Tras la posterior carga, la cristalinidad del material original no se recupera aunque existen claras evidencias de la reoxidación de los metales de transición.[17]

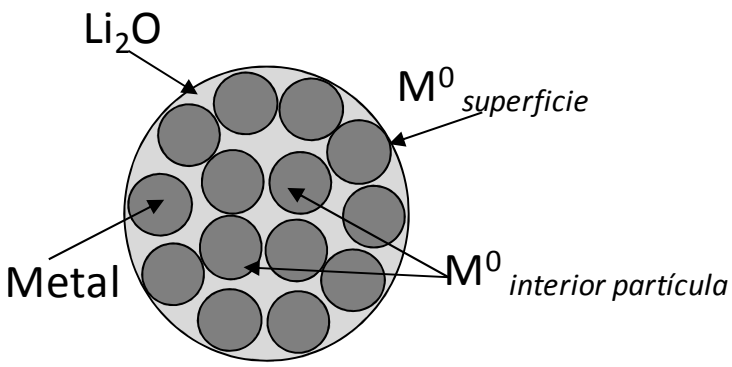

Figura 1.4. Producto de la reacción de conversión.

La reacción de conversión implica la desaparición completa de la estructura del óxido de partida. El metal de transición reducido aparece como nanopartículas de aproximadamente 5 nm embebidas en una matriz de Li_2O(Fig.1.4). La elevada superficie de la interfase M0/ Li_2O asegura la reversibilidad del proceso electroquímico. Diversos autores han observado diferentes entornos locales para átomos de hierro reducidos en este tipo de reacciones mediante el uso de la espectroscopía Mössbauer ^{57}Fe. Estos se han asignado a átomos localizados en el interior y en la superficie de las partículas, como se observa en la figura 1.4..[24]

Sin embargo dichos materiales presentan una reducción gradual de la capacidad debido a la histéresis que presenta el ciclo de carga-descarga. Para obtener un rendimiento óptimo de los materiales de conversión se están desarrollando amplios estudios para optimizar el tamaño de partícula y morfología de éstos compuestos.

1.3 Materiales catódicos

El material que se usa generalmente como electrodo positivo es un óxido de metal de transición con una estructura en capas, es decir, una

estructura laminar como puede ser $LiMO_2$ dónde M= Co, Ni, Mn. $LiCoO_2$ es el más ampliamente utilizado en las baterías de ión litio comerciales. El ión litio se intercala y desintercala en torno a 3,9 ~ 4,2 *V*. Aunque la deslitiación reversible de $LiCoO_2$ más allá de 0,5 Li^+ es factible,[25] la deslitiación para aplicaciones comerciales se ha limitado al valor de un máximo de 0.5 por razones de seguridad (máximo 4,2 *V*). Varias rutas han sido exploradas para tratar de evitar estos problemas de seguridad y capacidad. Una de ellas ha sido la síntesis mediante *chimie douce* de materiales análogos al $LiCoO_2$ como son $LiFeO_2$ y $LiMnO_2$.[5] A pesar de los numerosos métodos de síntesis y diversos intentos de obtener $LiFeO_2$ electroquímicamente atractivo, los resultados no han sido los esperados. En contraste, la investigación sobre $LiMnO_2$ ha sido más fructífera y la inestabilidad estructural de la fase $Li_xMn_2O_4$ espinela durante el ciclado ha sido recientemente disminuida a través de la sustitución catiónica de Mn por Cr ($Li_{1+x}Mn_{0.5}Cr_{0.5}O_2$).[26] La espinela $LiMn_2O_4$, a pesar de que posee alrededor de un ~10% menos de capacidad que $LiCoO_2$, tiene una ventaja en términos de coste y además se presenta como material "verde" ya que el Mn no es tóxico y se trata de un elemento muy abundante.[6]

En la búsqueda de materiales óptimos para su uso como electrodos positivos en baterías de ión litio, una opción prometedora la conforman los materiales NASICON, una familia de conductores iónicos de sodio o los materiales olivino cómo el silicato de magnesio y hierro. Ambos presentan estructuras polianiónicas construidas a partir de octaedros MO_6 donde M es Fe, Ti, V o Nb) y XO_4 aniones tetraédricos donde X es S, P, As, Mo o W.[6]

La extracción reversible de litio en $LiMPO_4$ donde M = Fe, Mn, Co, o Ni se estudió por JB Goodenough et al.[27] Ellos mostraron $LiFePO_4$ como un excelente candidato para su uso como cátodo en baterías recargables y con grandes ventajas al ser un material barato, no tóxico, y ambientalmente benigno. La extracción electroquímica se limita a 0,6 Li^+ por fórmula unidad, pero a pesar de dicha limitación la capacidad específica es de 100 a 110 $mAh.g^{1}$ aprovechando así un 90% de su capacidad teórica (169 $mAh.g^{-1}$). Estos compuestos polianiónicos presentan una extracción electroquímica reversible en una región interesante de potencial entre $3V$ y $3{,}5V$ vs Li^0/Li^+, así como altos de difusión de litio y por lo tanto son serios candidatos para la próxima generación de baterías de ión litio.[7]

Dentro de los materiales NASICON, aquellos compuestos capaces de intercalar hasta 2 Li^+ de manera reversible están bajo especial atención como las familias de $Fe_2(XO_4)_3$ donde X = Mo, W, S [28] o los tiatanatos y silicatos del tipo Li_2MSiO_4 donde M = Fe, Mn, Co que están presentando altos valores de capacidad.[29]

1.4 Objetivos y plan de trabajo

Hay dos objetivos principales generales en ésta tesis. Por un lado, la optimización de óxidos mixtos para su uso como ánodos en baterías de ión litio mediante el uso de nuevas rutas de síntesis como las metodologías sol-gel o micelas inversas con el fin de obtener tamaños de partícula y morfologías adecuadas para su propósito. Por otro lado, la síntesis y la optimización de materiales tales como fosfatos y fluorofosfatos que supongan una alternativa a los materiales catódicos

de intercalación existentes tanto para uso en baterías de ión litio como ión sodio.

Para conseguir estos dos grandes objetivos se ha establecido el siguiente plan de trabajo cuyos resultados positivos han sido plasmados en las publicaciones que se desarrollan en la presente memoria:

1. Síntesis mediante sol-gel y micelas inversas para la obtención de la familia de materiales MFe_2O_4 donde M=Ni, Co, Cu y Fe principalmente con diferentes tamaños de partícula y morfologías.

2. Caracterización estructural mediante técnicas de difracción de rayos X, Espectroscopía Infrarroja, Microscopía de alta resolución y Espectroscopía Mössbauer para el análisis estructural de las fases obtenidas, control de impurezas, estudio de los cambios de los estados de oxidación del Fe y la dilucidación de los mecanismos de las reacciones de conversión.

3. Análisis de superficie y textural mediante microscopía SEM de las diferentes morfologías obtenidas.

4. Caracterización electroquímica mediante ciclado galvanostático, medidas potenciostáticas (*Step potential electrochemical spectroscopy (SPES))* y espectroscopía de impedancia compleja en celdas de litio de dos y tres electrodos con el objetivo de comprender las propiedades electroquímicas de las muestras más prometedoras.

Los puntos 1, 2, 3 y 4 del plan de trabajo se desarrollan a lo largo del capítulo 2 de la presente memoria.

5. Síntesis de materiales relativamente novedosos en el campo de los cátodos de intercalación mediante estado sólido o sol-gel como

$Na_3Fe_{2-x}Cr_x(PO_4)_3$ y Na_2FePO_4F y mediante cambio iónico como $Li_3Fe_{2-x}Cr_x(PO_4)_3$.

6. Caracterización estructural mediante técnicas Difracción de Rayos X, Espectroscopía Infrarroja, Microscopía de alta resolución y Espectroscopía Mössbauer para el análisis estructural de las fases obtenidas, control de impurezas, estudio de los cambios de los estados de oxidación del Fe y la dilucidación de los mecanismos envueltos en las reacciones de intercalación.

7. Análisis termo-gravimétricos para cuantificar el porcentaje de carbón *in situ* en las muestras y análisis de superficie y textural mediante microscopía SEM de las diferentes morfologías obtenidas.

8. Análisis químico mediante espectroscopía dispersiva de rayos X con el fin de cuantificar la proporción de Na/P en las muestras de $Na_3Fe_{2-x}Cr_x(PO_4)_3$ y de $Li_3Fe_{2-x}Cr_x(PO_4)_3$.

9. Caracterización electroquímica mediante ciclado galvanostático, medidas potenciostáticas y espectroscopía de impedancia compleja en celdas de litio y de sodio de dos y tres electrodos para el estudio de los procesos electroquímicos durante el ciclado frente a litio o sodio de los diferentes materiales.

Los puntos 5, 6, 7, 8 y 9 son desarrollados en el capítulo 3 de la presente memoria.

Referencias

1. Lavela P., Tirado J.L. *Baterías avanzadas* **2003**
2. Doeff M.M., Ma Y., Visco S.J., de Jonghe L.C., *J. Electrochem. Soc.* **1993**, 140, L169.
3. Ellis B.L., Makahnouk W.R.M., Makimura Y., Toghill K., Nazar L.F., *Nat. Mater.* **2007**, 5, 749.
4. David Linden and Thomas B. Reddy. **2002**, *The hand Book of Batteries*: Third edition.
5. Tarascon J.-M., Armand M., *Nature* **2001**, 414, 359-367.
6. Winter M., Besenhard J.O., Spahr M.E., Novák P., *Advanced Materials*. **1998**, 10, 10.
7. Nagaura T., Tozawa K., *Prog. Batt. Solar Cells* **1990**, 9 , 209.
8. Tirado J.L., *Mat. Sci. Eng.* **2003**, R40, 103.
9. Alcántara R., Jiménez-Mateos J.M., Lavela P., Tirado J.L., *Electrochem. Commun.* **2001**, 3, 639.
10. Alcántara R., Jiménez-Mateos J. M., Tirado J. L., *J. Electrochem. Soc.* **2002**, 149, A201.
11. Alcántara R., Jaraba M., Lavela P., Tirado J. L., *Chem. Mater.* **2002**, 14, 2847.
12. Recham N., Chotard J-N., Dupont L., Djellab K., Armand M., Tarascon J.M., *J. Electrochem. Soc.* **2009**, 156, A993.
13. Winter M, Besenhard J.O., Spahr M.E., Novak P., *Adv. Mater.* **1998**, 10,725.
14. Bruce P.G., *Solid State Ionics*. **2008**, 179, 752–760.
15. Grugeon S., Laruelle S., Dupont L., Tarascon J.-M., *Solid State Sciences*. **2003**, 6, 895–904.

16. Poizot, P., Laruelle, S., Grugeon, S., Dupont, L. Tarascon J.M, *Nature*. **2000**, 407, 496.
17. Grugeon S., Larruelle S., Herrera-Urbina R., Dupont L., Poizot P., Tarascon J.-M., *J. Electrochem. Soc.* **2001**, 148, A285–A292.
18. Shao-Horn Y., Osmialowski S., Horn Q.C., *J. Electrochem. Soc.* **2002**, 149, p. A1547
19. Shodai T., Okada S., Tobishma S., Yamaki J., *J. Power Sources.* **1997**, 68 , p. 515.
20. Aragón M.J., León B., Vicente C.P., Tirado J.L., *Journal of Power Sources*. **2001**, 196, 5, 2863–2866 .
21. Aragón, M.J., León, B., Vicente, C.P., Tirado, *J.L. Inorganic Chemistry*. **2008**, 47, 22, 10366-10371.
22. Aragón, M.J., León B., Vicente, C.P., Tirado J.L., Chadwick A.V., Berko A., Beh S.-Y., *Chemistry of Materials*. **2009**, 21, 9, 1834-1840.
23. Vidal-Abarca C., Lavela P., Tirado J.L., *J. Phys. Chem. C* **2010**, 114, 12828-12832.
24. Lavela P., Tirado J. L., Womes M., Jumas J.C., *J. Phys. Chem. C* **2009**, 113, 20081–20087
25. Jan N. Reimers and J. R. Dahn, Electrochemical and in situ X-Ray Diffraction Studies of Lithium Intercalation in Li_XCoO_2.
26. Ammundsen B., Desilvestro J., Groutso T., Hassell D., Metson J. B., Regan E., Steiner R., Pickering P. J., *Journal of The Electrochemical Society*. **2000**, 147, 11, 4078-4082.
27. Padhi A. K., Nanjundaswamy K. S., Goodenough J. B., *Journal of Electrochemical Society*. **1997**, 144, 4.
28. Masquelier C., Pahdi A.K., Nanjundaswamy K.S., Goodenough J. B., *Journal of Solid State Chemistry*. **1998**, 135, 228-234.

29. Nytén A., Abouimrane A., Armend M, Gustafsson T., Thomas J.O., *Electrochemistry Communication* **2005**.

Capítulo 2

Óxidos mixtos para ánodos de conversión en baterías de ión litio

2.1. On the role of faradaic and capacitive contributions in the electrochemical performance of $CoFe_2O_4$ as conversion anode for Li-ion cells

C. Vidal-Abarca, P. Lavela*, J.L. Tirado

Laboratorio de Química Inorgánica, Universidad de Córdoba. Edificio Marie Curie Campus de Rabanales 14071 Córdoba, Spain

Abstract

$CoFe_2O_4$ samples were synthesized by the reverse micelles procedure. The electrochemical performance of the studied samples was explained in terms of capacitive and faradaic contributions to charge storage, by using SPES at several sweep rates. The faradaic storage mechanism was considered as the main contribution to global capacity, while the capacitive component has positive effect on the kinetic response. ^{57}Fe Mössbauer spectra of recorded samples revealed that core iron plays an important role to prolong the faradaic redox reaction for a large number of cycles at high capacity values. The best performance was recorded for the sample prepared in strong alkaline medium and annealed at 800ºC. Capacity values of ca. 600 $mAh.g^{-1}$ were recorded after 100 cycles.

Solid State Ionics 181 (2010) 616-622

**corresponding author*

2.1.1 *Introduction*

Electrochemical lithium driven reactions have opened a new field of research for the negative electrode of lithium ion batteries.[1-3] Transition metal compounds can be electrochemically reduced to obtain the transition element in a metallic state and lithium oxide. The resulting nanometric metal particles are embedded in a Li_2O matrix. Although the energy for the subsequent oxidation is large, the close proximity of reagents favors the reversibility of the electrochemical reaction.[4] In previous reports, cobalt containing compounds have demonstrated to deliver high capacity values for a long term cycling.[5-7]

The use of $CoFe_2O_4$ may provide some advantages as the introduction of a low-cost and environmentally friendly transition metal. The initial long range ordering of the oxide is lost during the first discharge because of the enhanced structural degradation. Fortunately, ^{57}Fe Mössbauer spectroscopy can be used to analyze the changes in the oxidation state and the local environment of iron atoms upon the electrochemical reaction. This technique has demonstrated to be useful to unfold the mechanisms involved in lithium driven conversion reactions.[8-10]

Cobalt ferrite has been prepared by several methods including sol-gel processes among others.[11] In fact, we reported high capacity values for a $CoFe_2O_4$ sample prepared at 1000ºC by a sol-gel method.[12] The use of high annealing temperatures increases the production costs. Here we report an alternative route of synthesis based on the use of organic anionic surfactants that stabilize reverse (water-in-oil) micelles. These tiny aqueous droplets behave as nanoreactors in which transition metal

water-soluble salts react to yield a solid precursor. A further annealing will provide the final oxide.

2.1.2 *Experimental*

A reverse micelles procedures with Span 80 as a surfactant was used in this study. The reaction took place by the coalescence of two different reverse micelles containing aqueous solutions of NaOH and metal chlorides, respectively. The effect of NaOH concentration was checked by using 6 and 8 M solutions. The organic phase selected for this procedure was hexane. The aqueous to organic volume ratio was set at 1:1. Precursors were rinsed with water, and heated in air at 800 and 1000 ºC for 15 hours. Samples will be referred to as CoFeXMT (X: 6 and 8; T: 800 and 1000).

X-ray diffraction (XRD) patterns were recorded in a Siemens D5000 diffractometer, with a CuKα radiation and a graphite monochromator. A step scan procedure was set with a pass of 0.02° (2θ) and a measuring time of 1.2 s. The Williamson-Hall method was used to calculate the crystallite size. SEM images were obtained with a JEOL-SM6300 microscope.

An EG&G constant acceleration spectrometer and a ^{57}Co (Rh matrix) (10 mCi) gamma radiation source were used for recording ^{57}Fe Mössbauer spectra in transmission mode at room temperature. The magnetic sextet recorded from a high purity iron foil was used to calibrate the velocity scale. Experimental data were fitted to Lorentzian lines by using a least

square based method.[13] The quality of the fit was controlled by the classical test of χ^2.

Battery tests were carried out by using two electrodes Swagelok type cells. Counter electrodes were 9 mm discs of lithium metal and the working electrode consisted of a mixture of 75 % of active material, 5% of PVDF binder, 10 % of graphite and 10 % of carbon black, and were deposited on a cooper foil of the same diameter. The use of graphite:carbon-black mixtures as conductive material allowed a notorious improvement in both mechanical strength and conductive properties as compared to exclusively containing carbon black in the same ratio. The electrodes were dried at 250ºC in Ar atmosphere for 16 hours to ensure the binder distribution and adhesion to the electrochemically active particles.

A 1 M $LiPF_6$ (EC:DEC = 1:1) electrolyte solution was supported in Whatman glass fiber discs. Galvanostatic tests were carried out on an Arbin galvanostat multichannel system. The imposed kinetic rate was fixed at 1C for both charging and discharging. Step potential electrochemical spectroscopy (SPES) was monitored on a MacPile System. Electrochemical impedance spectroscopy (EIS) was carried out in an Autolab PGSTAT12 system. A three-electrode lithium cell was successively cycled by passing current between the working electrode (evaluating material) and the counter electrode (Li). After a period of relaxation, at least 5 h, to achieve a quasi-equilibrium system, the impedance spectra were recorded versus a Li reference electrode. An ac voltage signal of 5 mV was applied from 100 to 2 mHz.

2.1.3 Results and discussion

Sample purity was checked by XRD (Fig.2.1.1). The patterns were characterized by narrow and intense reflections indexed in the Fd3m space group corresponding to $CoFe_2O_4$ (JCPDS 03-0864).

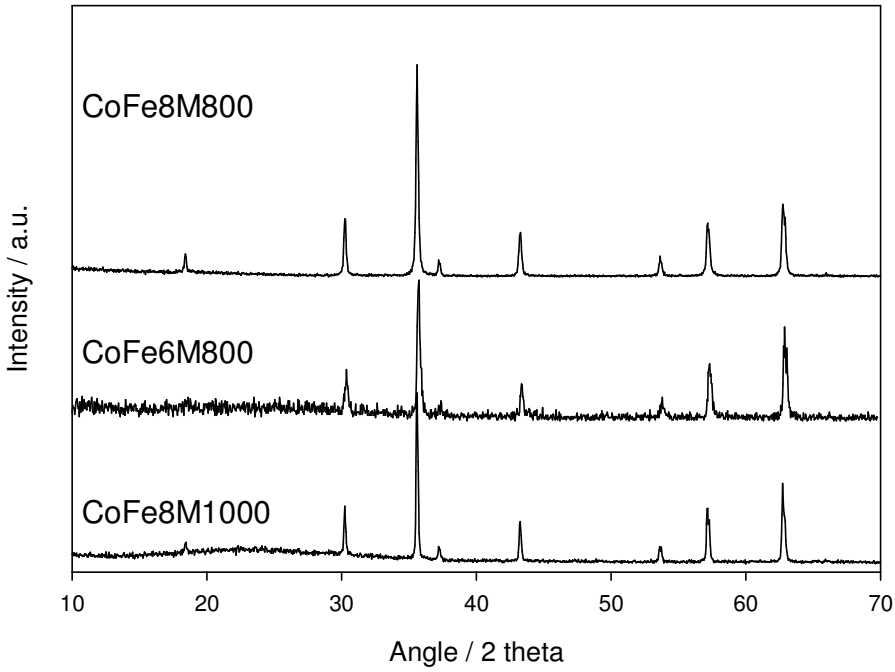

Figure 2.1.1. X-ray diffraction patterns of CoFe8M800, CoFe6M800 and CoFe8M1000.

The ^{57}Fe Mössbauer spectra of $CoFe_2O_4$ samples, prepared by using 8 M NaOH, were recorded to determine magnetic properties and cation distribution (Fig. 2.1.2 and Table 2.1.I).[14,15]

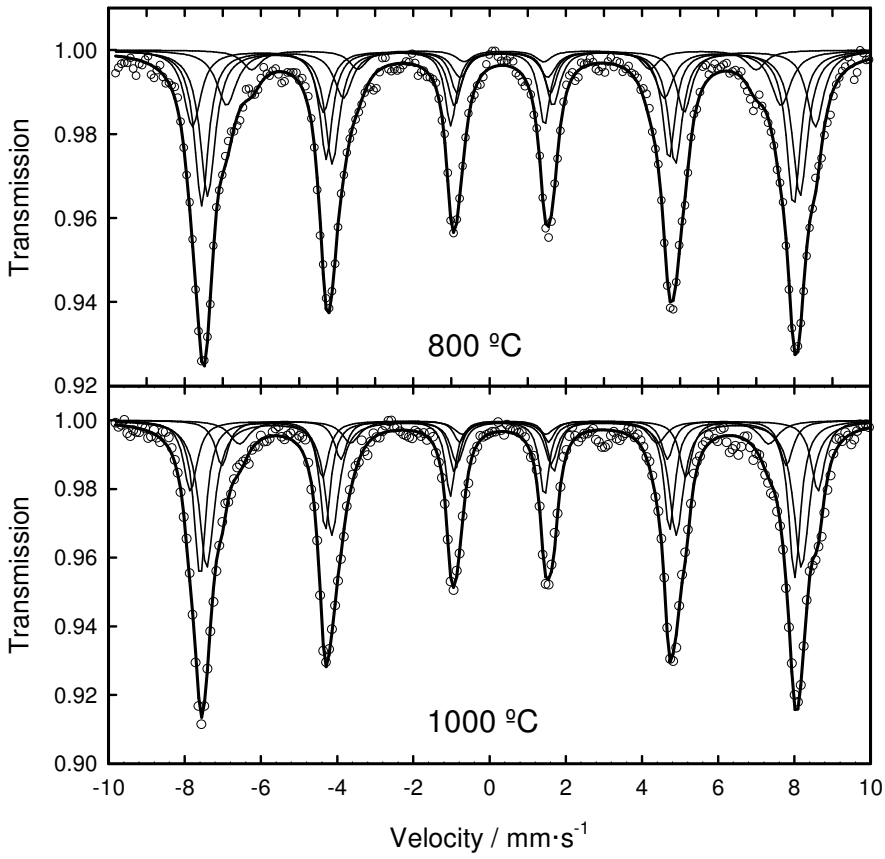

Figure 2.1.2. ^{57}Fe Mossbauer spectra of CoFe8M800 and CoFe8M1000.

Figure 2.1.2 shows the occurrence of sextets arising from the Zeeman splitting of the nuclear levels as a consequence of the presence of ferrimagnetic domains in well crystallized particles. Their asymmetric profiles reveal the occurrence of non-resolved components ascribable to different local environments of iron atoms. It is well known that Co^{2+} ions are preferentially located at octahedral sites, whereas the Fe^{3+} ions distribute between octahedral and tetrahedral coordination sites in the spinel lattice. However, a more complex deconvolution of the $CoFe_2O_4$ spectra has been reported in which the presence of five overlapped sextets has been revealed.[16] According to these authors, iron in tetrahedral sites is evidenced by a single sextet component while four additional sextets are deconvoluted for iron atoms located in octahedral

sites surrounded by different numbers of nearest Fe^{3+} neighbor ions. Our spectra were fitted according to this model (Table 2.1.I).

Table 2.1.I. Hyperfine parameters of CoFe8M800 and CoFe8M1000.

Sample	[a]δ (mm/s)	[b]Δ (mm/s)	[c]2Γ (mm/s)	[d]B_{hf}(T)	[e]C (%)	[f]χ^2
CoFe8M800	0.37(2)	0.015 (8)	0.53(4)	50.9(1)	19.2	0.466
	0.37(1)	0.006 (4)	0.48(2)	48.3 (1)	30.0	
	0.37(3)	-0.01 (1)	0.62(8)	45.2(2)	15.0	
	0.37(5)	-0.07 (3)	0.61(9)	41.1(3)	6.5	
	0.21(5)	-0.010 (4)	0.44(2)	48.2(1)	29.3	
CoFe8M1000	0.38(1)	0.026(7)	0.42(3)	51.1 (1)	17.2	0.494
	0.38(1)	0.005 (4)	0.49(3)	48.5(1)	35.6	
	0.38(3)	-0.03 (1)	0.42(9)	46.0(2)	9.5	
	0.38(5)	0.02 (2)	0.62(9)	43.2(3)	8.8	
	0.20(1)	-0.005 (4)	0.38(2)	48.5(1)	28.9	

[a] δ: isomer shift; [b] Δ: quadrupole splitting; [c] 2Γ: full line width at half maximum; [d] B_{hf}: Hyperfine magnetic field; [e] C: contribution to total absorption; [f] χ^2: goodness of the fitting.

Four signals at ca. 0.37 $mm.s^{-1}$ are attributed to iron at the octahedral sites (Fe(Oh)), whereas a signal at ca. 0.21 $mm.s^{-1}$ is assigned to iron in tetrahedral sites (Fe(Td)). The Fe(Td)/Fe(Oh) occupancy ratio can be calculated from the relative contribution of the subspectra. It took values of 0.41 for both samples which agrees with the occurrence of an inverse spinel.

Figure 2.1.3 shows SEM images of selected $CoFe_2O_4$ samples. Submicronic particles are densely packed in large agglomerates. It has been reported that both morphology and particle size have an influence on the performance. NuLi et al. showed that nanospherical α-Fe_2O_3 displayed the best electrochemical performance among other

nanoparticle shapes. It was attributed to the high surface area and small and uniform grain size.[17]

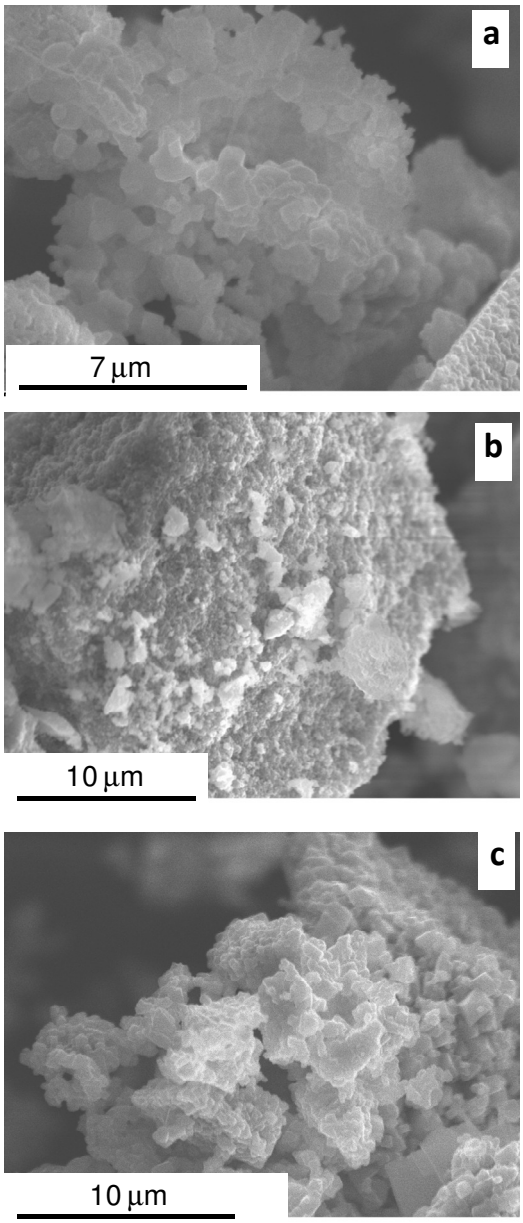

Figure 2.1.3. SEM images of a) CoFe8M800, b) CoFe6M800 and c) CoFe6M1000.

In contrast, other authors reported better capacity retention for Cu_2O and CuO samples with micrometric size.[18] Capacity fading on extended cycling of well dispersed nanometric Co_3O_4 particles has been assigned to oxide dissolution in the cell electrolyte.[19] Otherwise, good

electrochemical results have been recorded on submicronic $CoFe_2O_4$. The occurrence of a macroporous system favoring the electrolyte/electrode contact was considered the determinant effect rather than particle size.[11] In this way, Dahn et al. pointed out that the mechanical strength provided by an appropriate selection of binder is even more determining than a nanometer size in the raw material.[20]

Galvanostatic curves of lithium test cells, assembled with the ferrite samples as the positive electrode, revealed the common features in lithium driven conversion reactions (Fig. 2.1.4). An extended plateau ascribable to the homogenous reduction of the transition metal ions is monitored during the first discharge of the raw crystalline material.

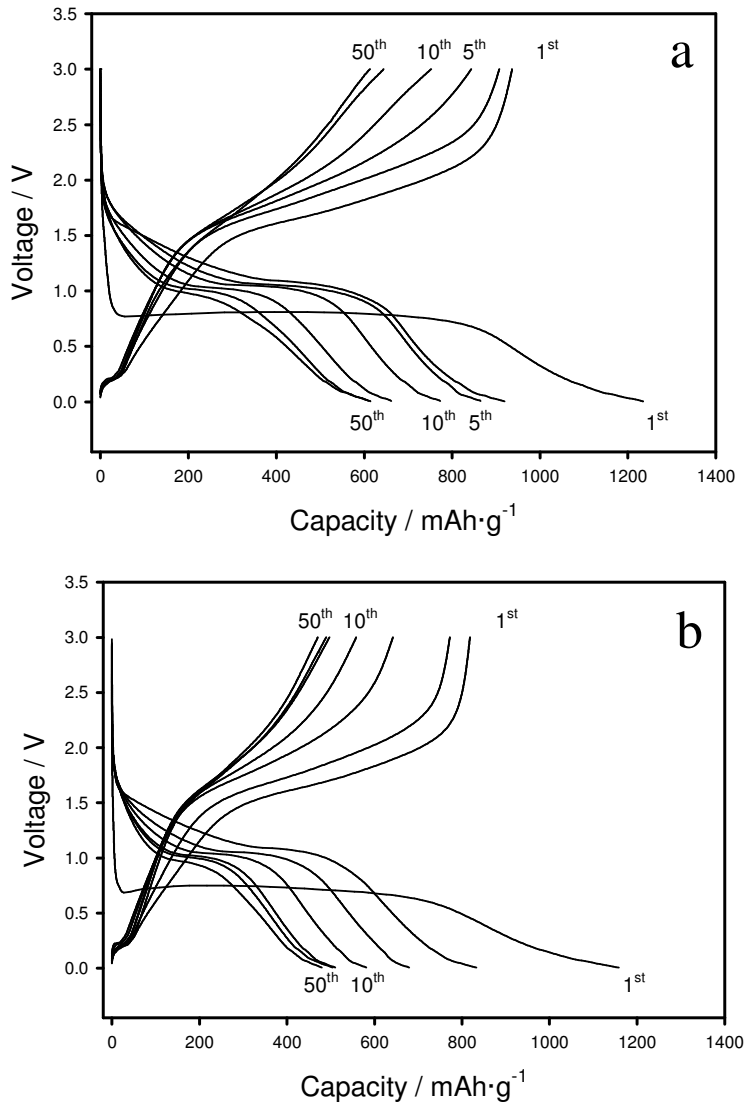

Figure 2.1.4. Galvanostatic discharge and charge profiles of CoFe8M800 and CoFe6M800 samples.

The eventual voltage drop to zero proceeded steadily through a pseudo-capacitive process, which can be ascribed to a polymeric layer formation [21] and/or capacitive charge accumulation at the interphase.[22] The different profile of the subsequent discharge branches evidences the partial reversibility of the structural and morphological transformation occurring during the first discharge. On extended cycling, the most relevant difference is the progressive shortening of the plateau ascribed to the transition metal redox reaction. From the comparison of galvanostatic curves of two selected samples, marked differences in the

profiles were not observed. However, an enhanced fading is evident from the extent of the plateau for the CoFe6M1000 sample.

The SPES curves recorded at different scan rates were helpful to obtain more detailed information on the mechanism of charge storage. Capacitive and faradaic behaviors can be separated analyzing the relationship between the measured current and the sweep rate.[23] From this method of calculation, b values ($0 < b < 1$) could be obtained as an adjustable parameter. Values close to 0.5 are related to a faradaic behavior whereas those values near $b = 1$ should correspond to a capacitive behavior.

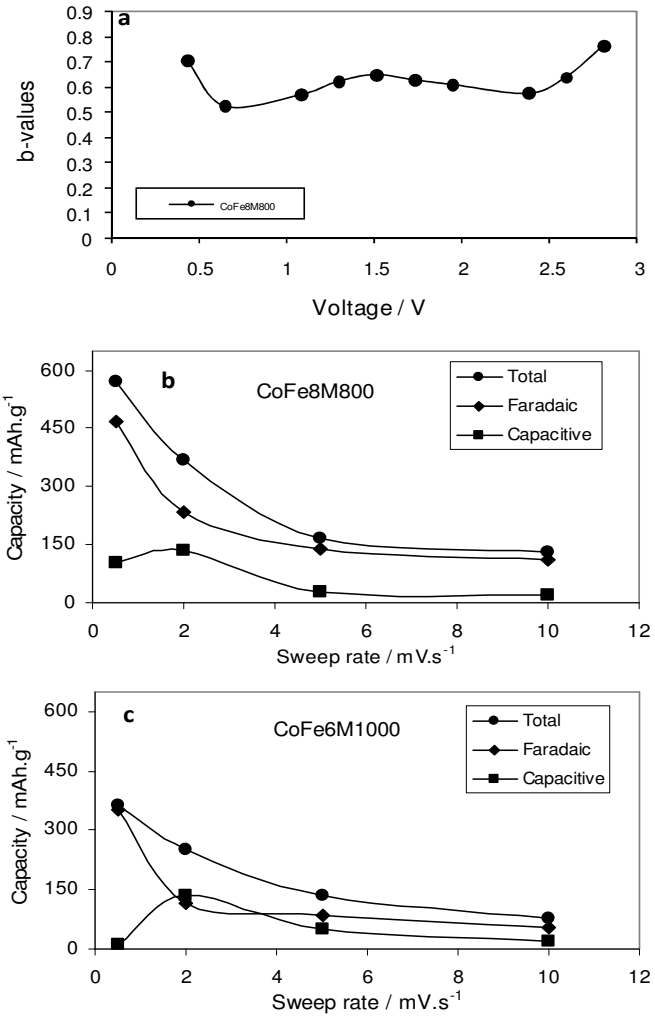

Figure 2.1.5. a) Calculated b-values for CoFe8M800 versus cell potential; Charge storage dependence of b) CoFe8M800 and c) CoFe6M1000.

Figure 2.1.5a shows *b* values for CoFe8M800 along the 7th discharge. Values close to the faradaic reaction were mainly detected in the 2-1 V range which is fairly coincident with the transition metal reduction as shown in figure 2.1.4. A capacitive behavior was observed at the beginning of discharge. However, a slight increase of the *b* value at end of discharge could be related to an enhanced capacitive behavior. These features were common for the samples here studied, namely CoFe8M800 and CoFe6M1000. From the area under the voltammetric curve and the separation of capacitive and faradaic components previously calculated, the overall capacity could be decomposed in faradaic and capacitive components, and evaluated as function of the sweep rate. Figure 2.1.5b and c show these results for CoFe8M800 and CoFe6M1000 samples. The capacity values were higher for CoFe6M1000, which agrees well with the capacities inferred from the curves in Fig. 2.1.4. However, a marked capacity decrease was observed in this sample when the discharge rate was increased. The large capacitive contribution in CoFe6M1000 at 2 $mV{\cdot}s^{-1}$ is responsible for this behavior. Thus, the particularly high total capacities recorded for CoFe8M800 should be ascribed to the large faradaic contribution, whereas the enhanced kinetic response of CoFe6M1000 can be related to the significant contribution of the capacitive component at intermediate rates.

The electrochemical performance of the electrode materials in a long term cycling was highly dependent on the NaOH concentration used in the preparation (Fig. 2.1.6). Thus, CoFe8M800 provided samples with the ability of maintaining capacity values ca. 600 $mAh.g^{-1}$ after 100 cycles for the oxide annealed at 800ºC. Also, the increase of the

annealing temperature to 1000ºC induced a significant decrease in capacity, irrespective of the alkali concentration.

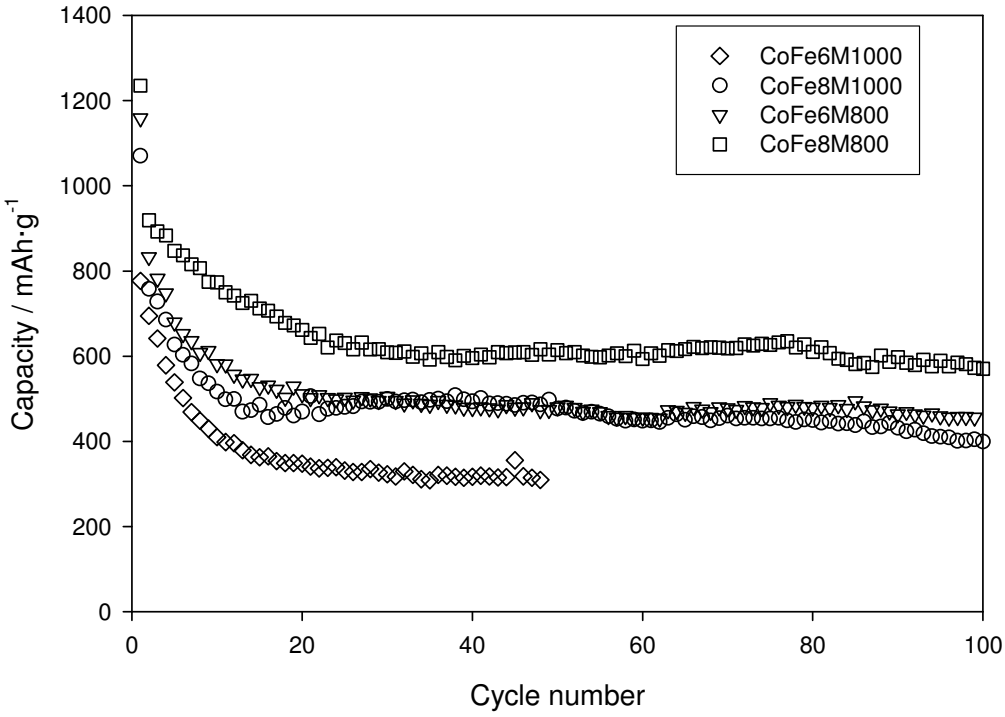

Figure 2.1.6. Extended galvanostatic cycling of $CoFe_2O_4$ samples obtained in different conditions.

^{57}Fe Mössbauer spectra allowed evaluating the changes in oxidation state and local environment of iron atoms during the first cycles. After cell discharge to 2 F.mol^{-1}, the sextets have disappeared by the rapid loss of the ferrimagnetic order, induced by the structural degradation that is typical of conversion reactions (Fig. 2.1.7). The spectrum can be decomposed in two signals with isomer shift values of 0.35(1) and 1.05(1) mm/s attributed to Fe^{3+} and Fe^{2+}, respectively. These results reveal the occurrence of ferrous ions as an intermediate species in the first overall reduction process. The spectrum recorded for the fully discharged electrode is composed of a doublet and a singlet signals with an isomer shift value of ca. 0.04 $mm.s^{-1}$, revealing an effective iron reduction. In previous works, on the preparation of cobalt and copper ferrites

prepared by a sol-gel method, we ascribed the doublet to surface Fe. However, higher isomer shifts (0.11 mm/s for $CoFe_2O_4$ [11] and 0.12 mm/s for $CuFe_2O_4$ [24] were recorded. It was ascribed to side reactions with the electrolyte, which leads to an undesirable partial oxidation.

Table 2.1.II. Hyperfine parameters of electrochemically reacted electrodes of CoFe8M800, CoFe8M1000 and CoFe6M800.

Sample	Electrode	[a]δ (mm/s)	[b]Δ(mm/s)	[c]2Γ (mm/s)	[d]C (%)	[e]χ^2
CoFe8M800	2 F/mol	0.34(1)	0.30(1)	0.53(2)	62.4	0.509
		1.05(1)	0.68(2)	0.53(4)	37.6	
	Recharged at 3 V	0.28(2)	0.99 (3)	0.49(6)	56.7	0.593
		0.25(1)	0.49 (3)	0.49(3)	43.3	
	1st Discharge	0.04(1)	--	0.61(7)	17.5	0.470
		0.04(1)	0.65(3)	0.61(2)	82.5	
	6th Discharge	0.02(1)	--	0.70(3)	37.9	0.526
		0.06(1)	0.77(2)	0.70(2)	62.1	
CoFe8M1000	1st Discharge	0.04(2)	0.27(3)	0.52(2)	59.8	0.444
		0.05(1)	0.76(2)	0.52(5)	40.2	
	6th Discharge	0.03(1)	0.56(1)	0.81(2)	100	0.562
CoFe6M800	1st Discharge	0.02(2)	0.35(5)	0.52(2)	41.7	0.350
		0.04(2)	0.72(4)	0.52(8)	58.3	
	6th Discharge	0.00(1)	--	0.70(2)	35.7	0.535
		0.03(1)	0.85(2)	0.70(2)	64.3	

[a] δ: isomer shift; [b] Δ: quadrupole splitting; [c] 2Γ: full line width at half maximum; [d] C: contribution to total absorption; [e] χ^2: goodness of the fitting.

The results obtained on $CoFe_2O_4$ prepared by the reverse micelle method are indicative of a more effective reduction of surface iron atoms. The spectrum of the subsequent charge at 3 *V* is characterized by two

quadrupolar doublets at 0.28 and 0.25 $mm.s^{-1}$. The isomer shifts of both subspectra reveal the oxidation of iron atoms, though a clear assignation to a particular local environment is difficult due to the high structural disordering of fully re-oxidized samples. It has been reported that ball-milled $CuFe_2O_4$ samples also lead to two super-paramagnetic doublets. However, the authors could not clearly infer the assignation to either octahedral and tetrahedral spinel locations or core and surface sites.[25] Otherwise, Aragón et al. have reported the absence of Fe^{2+} on the electrochemically recharged of ferrous oxalate evidencing that the oxidation reaction in lithium conversion reaction does not match to the raw electrode material. From this background and the exposed results only the equation describing the reduction process can be stated:

$$CoFe_2O_4 + 8\ Li^+ \longrightarrow Co^0 + 2\ Fe^0 + 4Li_2O \qquad (1)$$

In order to unfold the origin of the different electrochemical performance, the ^{57}Fe Mössbauer spectra of selected $CoFe_2O_4$ samples were recorded at the end of the first and sixth discharges (Fig. 2.1.7 and 2.1.8).

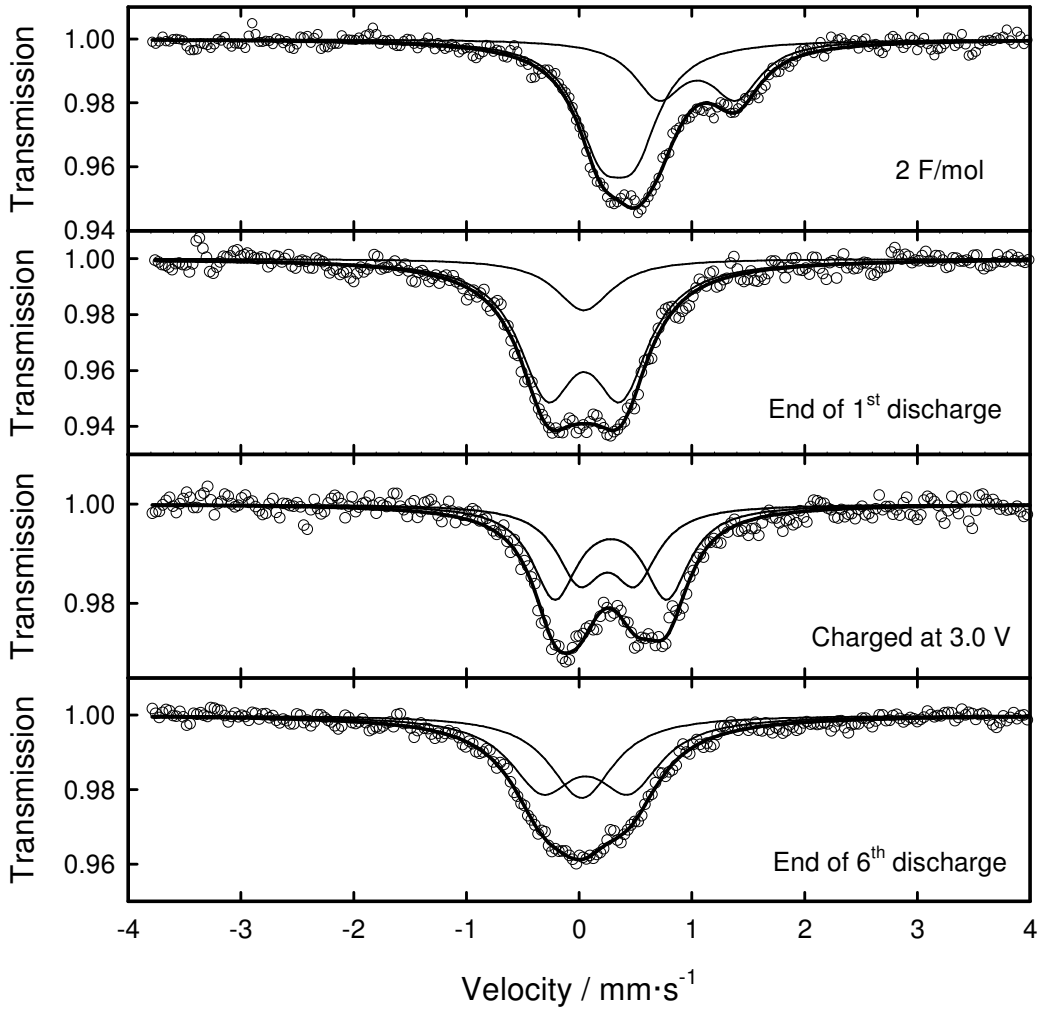

Figure 2.1.7. ^{57}Fe Mossbauer spectra of CoFe8M800 electrodes after the discharge at 2 *F.mol^{-1}*, fully discharge, recharge at 3 V and six discharges.

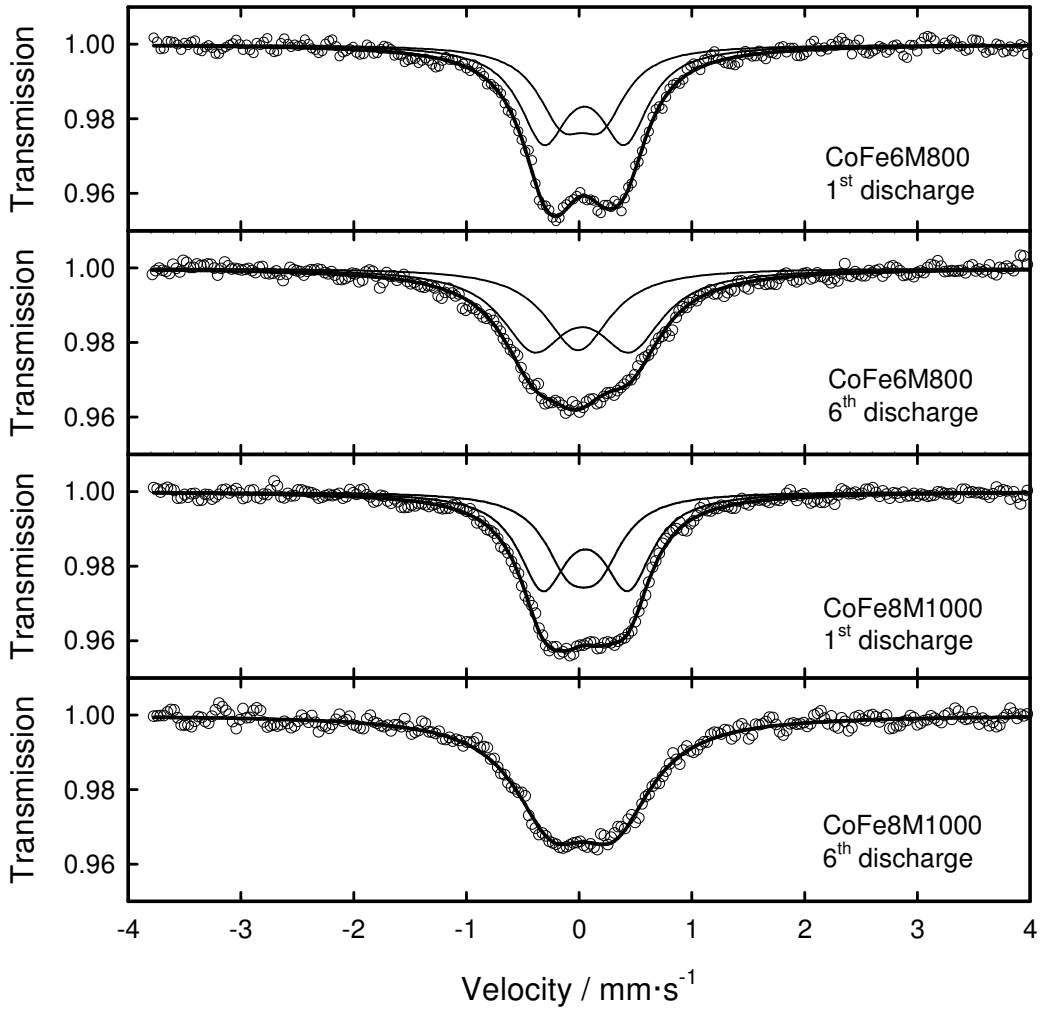

Figure 2.1.8. ^{57}Fe Mossbauer spectra of CoFe6M800 and CoFe8M1000 electrodes after the first and sixth discharges.

The broadening of the deconvoluted signals upon cycling was a common result for the studied samples. It can be ascribed to the enhanced structural deterioration during the charge and discharge cycles. Most likely, our model must be considered as a single approach to a more complex site distribution existing in the amorphous cycled electrodes. Recently, a degradation effect contributing to capacity fading has been correlated to the decrease in the relative contribution of the low-splitting signal, attributed to core iron.[26] For CoFe8M800, the contribution of core iron atoms increased during the first six cycles,

ensuring the contribution of faradaic capacity through the redox reaction to the overall capacity. In contrast, a significant reduction of this component was observed in CoFe6M800 and CoFe8M1000, which agrees with the lower capacity values measured by continuous galvanostatic cycling. Moreover, a complete disappearance of the low-splitting signal was observed for the sample annealed at 1000ºC.

The changes in the local structure of cycled electrodes have also a direct effect on the kinetic response of these materials. Figure 2.1.9 displays selected Nyquist plots obtained for CoFe8M800 and CoFe6M800 samples.

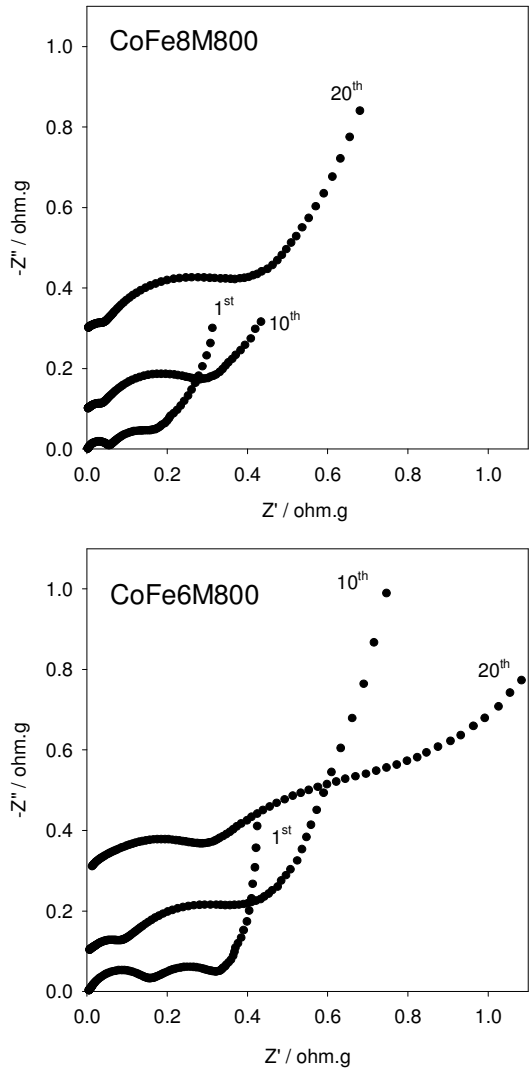

Figure 2.1.9. Impedance spectra of electrodes discharged after the first, tenth and twentieth discharge for CoFe8M800 and CoFe6M800 samples.

The spectra were recorded at the end of selected discharges. Two depressed semicircles are clearly observed at high and intermediate frequencies, which are commonly attributed to lithium migration through the electrolyte/inorganic surface film and charge transfer through the particle surface.[27] The fitting of the spectra allowed us to calculate the resistance values for the lithium migration through the surface film (R_{sf}) and charging transfer process (R_{ct}) (Table 2.1.III). On cycling, a more steady increase of both resistances is observed for CoFe8M800, justifying the best electrochemical performance.

Table 2.1.III: Fitted parameters of the electrochemical impedance spectra recorded for CoFe6M800 and CoFe6M800. Electrodes were measured at full discharge.

CoFe8M800						
n^{th} discharge	R_{sf}(Ohm·g)	CPE_{sf}		R_{ct}(Ohm·g)	CPE_{ct}	
		Y_0 $(Ohm·g)^{-1/n}·s^n$	n		$Y_0(Ohm·g)^{-1/n}·s^n$	N
1st	0.055	$5.94·10^{-09}$	0.73	0.113	$3.24·10^{-06}$	0.72
10th	0.046	$3.60·10^{-09}$	0.54	0.233	$1.10·10^{-06}$	0.74
20th	0.047	$1.60·10^{-09}$	0.52	0.355	$6.12·10^{-07}$	0.70
CoFe6M800						
1st	0.167	$5.24·10^{-09}$	0.68	0.154	$3.71·10^{-06}$	0.78
10th	0.106	$3.16·10^{-09}$	0.57	0.304	$1.66·10^{-06}$	0.71
20th	0.315	$1.71·10^{-10}$	0.54	0.615	$1.65·10^{-07}$	0.59

The depression in the shape of the semicircles reveals a frequency dispersion that cannot be described by simple elements. This effect is

generally attributed to a "capacitance dispersion" expressed in terms of a constant-phase element (CPE).[28] The expression for the impedance response of CPE is:

$$Q = (Y_0 j\omega)^{-n} \quad (2)$$

The CPE has been considered to represent a circuit parameter with limiting behavior as a capacitor for $n = 1$, a resistor for $n = 0$. Nevertheless, electrode double layers with a CPE character show illogical capacitance values.[29]

From table 2.1.III, we observe that n values are far from the behavior expected from an ideal capacitor. For this reason, our discussion was mainly focused on the resistance values.

2.1.4 *Conclusions*

$CoFe_2O_4$ samples were prepared by a reverse micelles procedure. The XRD patterns evidenced the validity of this method for obtaining well crystallized and pure spinel samples. ^{57}Fe Mössbauer spectroscopy revealed the ferromagnetic character of the raw material. The asymmetric profiles are characteristic of the complex local environment of iron atoms surrounded by a different number of cobalt and iron neighbors. SEM images revealed the presence of submicronic particles densely packed in large agglomerates as a common morphology of the studied samples.

SPES recorded at several sweep rates allowed to differentiate the faradaic and capacitive components of charge storage in the studied material. As compared with CoFe8M800, a significant capacitive

contribution allows CoFe6M1000 to display better capacity retention at intermediate rates. Nevertheless, the large faradaic contribution for the sample prepared at 800ºC counteracted this effect and provided the highest capacity values (ca. 600 $mAh.g^{-1}$) for a large number of cycles. The Mossbauer spectra recorded for cycled electrodes evidenced a significant diminution of the population of core iron atoms for those samples with a poorer electrochemical performance. In fact, core irons are responsible for the reversible redox reaction during cycling and hence contribute to the faradaic component of the stored charge. Also, the changes in the local environment of iron were related to the increase of impedance for samples displaying a poorer performance.

Acknowledgments

We appreciate the financial support from the MEC (Contract MAT2008-0558) and Government of Andalusia (Project FQM1447, group FQM288). We also want to thank the Central Support Service for Research at the University of Cordoba.

References

1. Arico A. S., Bruce P., Scrosati B., Tarascon J.M., van Schalkwijk W., *Nature Materials* **2005**, 4, 366-377.
2. Bruce P. G., Scrosati B., Tarascon J.M., *Angew. Chem. Int. Ed.* **2008**, 47, 2930.
3. Tirado J.L., *Mat Sci Eng.* **2003**, R 40, 103.
4. Poizot P., Laruelle S., Grugeon S., Tarascon J. M., *J. Electrochem. Soc.* **2002**, 149, A1212.
5. Poizot P., Laruelle S., Grugeon S., Dupont L., Tarascon J.M., *Nature* **2000**, 407, 496.
6. Vidal-Abarca C., Lavela P., Tirado J. L., *Electrochem. Solid-State Lett.*, **2008**, 11, A198.
7. Lavela P., Tirado J.L., Vidal-Abarca C., *Electrochim. Acta* **2007**, 52, 7986.
8. Obrovac M. N., Dunlap R. A., Sanderson R. J., Dahn J. R. *J. Electrochem. Soc.* **2001**, 148, A576.
9. Larcher D., Bonnin D., Cortes R., Rivals I., Personnaz L., Tarascon, J. M. *J. Electrochem. Soc.* **2003**, 150, A1643.
10. Lavela P., Tirado J. L., Womes M., Jumas J. C., *J. Phys. Chem. C* (doi: 10.1021/jp9056362).
11. Akl J., Ghaddar T., Ghanem A., El-Rassy H., *J. Mol. Catal. A: Chem.* **2009**, 312, 18.
12. Lavela P., Tirado J.L., *J. Power Sources* **2007**, 172, 379.
13. Kündig W., *Nuclear Instr. Methods,* **1969**, 75, 336.
14. Rajendran M., Pullar R. C., Bhattacharya A.K., Das D., Chintalapudi S.N., Majumdar C.K., Magn J. *Magn. Mater.* **2001**, 232, 71.

15. Grigorova M., Blythe H. J., Blaskov V., Rusanov V., Petkov V., Masheva V., Nihtianova D., Martinez Ll. M., Muñoz J.S., Mikhov M., Magn J., *Magn. Mater.,* **1998**, 183, 163.
16. Ferreira T.A.S., Waerenborgh J.C., Mendonça M.H.R.M., Nunes M.R., Costa F.M., *Solid State Sci.* **2003**, 5, 383.
17. NuLi Y., Zeng R., Zhang P., Guo Z., Liu H., *J. Power Sources.* **2008**, 184, 456.
18. Grugeon S., Laruelle S., Herrera-Urbina R., Dupont L., Poizot P., Tarascon J.M., *J. Electrochem. Soc.* **2001**, 148, A285.
19. Binotto G., Larcher D., Prakash A. S., Herrera-Urbina R., Hegde M. S., Tarascon J.M., *Chem. Mater.* **2007**, 19, 3032.
20. Li J., Dahn H.M., Krause L.J., Le D.B., Dahn J.R., *J. Electrochem. Soc.* **2008**, 155, A812.
21. Laruelle S., Grugeon S., Poizot, P. Dollé M., Dupont L., Tarascon J. M., *J. Electrochem. Soc.* **2002**, 149, A627.
22. Balaya P., Bhattacharyya A.J., Jamnik J., Zhukovskii Y.F., Kotomin E.A., Maier J., *J. Power Sources*, **2006**, 159, 171.
23. Brezesinski T., Wang J., Polleux J., Dunn B., Tolbert S. H., *J. Am. Chem. Soc.* **2009**, 131, 1802.
24. Bomio M., Lavela P., Tirado J. L., *ChemPhysChem.* 2007, 8, 1999.
25. Jiang J.Z., Goya G.F., Rechenberg H.R., *J. Phys.: Condens. Matter.* 1999, 11, 4063.
26. Lavela P., Tirado J. L., Womes M., Jumas J. C., *J. Electrochem. Soc.* 2009, 156, A589.
27. Dolle M., Poizot Ph., Dupont L., Tarascon J.M., *Electrochem. Solid-State Lett.* 2002, 5, A18.
28. Jorcin J.-B., Orazem M. E., Pebere N., Tribollet B., *Electrochim Acta* **2006**, 51, 1473.

29.Zoltowski P., *J. Electroanal. Chem.* 1998, 443, 149.

2.2. The origin of capacity fading in $NiFe_2O_4$ conversion electrodes for lithium-ion batteries unfolded by ^{57}Fe Mössbauer spectroscopy

C. Vidal-Abarca, P. Lavela*, J.L. Tirado

Laboratorio de Química Inorgánica. Universidad de Córdoba. Edif. Marie Curie, Campus de Rabanales, 14071 Córdoba. Spain.

Abstract

Li driven electrochemical conversion reaction is regarded as a promising mechanism for lithium storage in anode materials. Two $NiFe_2O_4$ samples have been prepared by a sol gel method at different annealing temperatures. The distinct textural properties were correlated to the electrochemical performance in lithium test cells. ^{57}Fe Mössbauer spectroscopy was used to evaluate the local environment of metallic iron atoms in the discharged electrodes. The different contributions of core and surface atoms have been correlated to the effect of the annealing temperature and the capacity fading observed during the first cycles. The decrease of the blocking temperature of ferromagnetic-superparamagnetic transition in the discharged electrodes is ascribed to a parallel decrease in the metallic particle size.

Journal of Physical Chemistry C 2010, 114, 12828-12832.

**corresponding author*

2.2.1 *Introduction*

Current research on electroactive solids for the anode of lithium ion batteries is no longer restricted to the reversible lithium intercalation the layered structure of graphitic materials or the formation of lithium-rich intermetallic compound of tin or silicon. Li driven conversion reactions on transition metal compounds have attracted much attention in recent years.[1-3] The possibility of fully reducing the transition metal atoms from their ionic to the metallic state benefits from high charge transfer per formula unit. Thus, eight electrons should be transferred for the following reaction:

$$NiFe_2O_4 + 8\ Li^+ \longrightarrow Ni^0 + 2\ Fe^0 + 4\ Li_2O \qquad (1)$$

Several methods have been proposed for the synthesis of $NiFe_2O_4$ as electrode in lithium batteries including the decomposition of layered double hydroxide precursors,[4] the deposition of thin film,[5] hydrothermal synthesis,[6] etc. Among them, the sol-gel method based on the precipitation of a citrate precursor has revealed as a straightforward and low cost process to produce transition metal ferrites. The oxide products are characterized by submicronic particles mutually interconnected and defining a macroporous system that ensures good contact with the electrolyte and mechanical strength to sustain high capacity values for a large number of cycles.[7-8]

Although the conversion reaction (1) is thermodynamically favorable, the feasibility of the reverted reaction is limited unless the initial crystallinity is not recovered.[9, 10] This fact impedes the use of diffraction techniques in the study of the reaction mechanisms. However, studies by different spectroscopic techniques revealed that transition metal

atoms are, at least partially, oxidized during charge vs. Li.[11-13] Among the techniques suitable for these studies, ^{57}Fe Mössbauer spectroscopy is particularly powerful to determine the local environment and oxidation state of iron atoms in both pristine ferrites and used electrodes of lithium test cells. Recently, we have reported the reliability of room temperature Mössbauer spectroscopy to unfold the origin of capacity fading in cobalt ferrite electrodes during the first few cycles.[14] However, the overlapping of several superparamagnetic doublets makes difficult spectra deconvolution and signal assignment.

The aim of this work is to take advantage of the selectivity and reliability of low temperature ^{57}Fe Mössbauer spectroscopy to deepen in the characterization of discharged electrodes, in order to evaluate the factors affecting their cyclability.

2.2.2 *Experimental Methods*

$NiFe_2O_4$ spinel oxides were prepared by a sol-gel method using a citrate ligand to complex the metal ions, as described elsewhere.[7] The precursors were annealed at 600 and 1000º*C* for 24 hours in air. X-ray diffraction (XRD) patterns were recorded with a Siemens D-5000 apparatus provided with CuKα radiation and graphite monochromator. The 2θ scan rate was 0.04° per 1.2 seconds. Crystallite size was calculated by the Scherrer equation. Scanning electron microscopy (SEM) was performed in a JEOL-SM6300 microscope. Transmission electron microscopy (TEM) was carried out in a PHILIPS CM-10. High resolution transmission electron microscopy (HR-TEM) was carried out in a JEOL JEM 2010.

Electrochemical tests were carried out in two-electrode Swagelok™ type lithium test cells. The lithium test cells were assembled by stacking a lithium metal disc as auxiliary electrode, Whatman glass fiber discs supporting a 1 M $LiPF_6$ (EC:DEC=1:1) electrolyte solution, and the working electrode. The latter was prepared by pasting the electrode material onto a copper foil. For this purpose, a mixture of 75% of active material and 10% of graphite, 10% of carbon black and 5% of PVDF binder was slurred in N-Methyl Pyrrolidone to form the paste. An Arbin potentiostat/galvanostat multichannel system was used to cycle the lithium cells at 1C for the extended cycling and at C/2 for the preparation of Mössbauer samples. The cell voltage limits were set at 3 and 0.02 *V*.

^{57}Fe Mössbauer spectra were recorded in transmission mode (TMS) at room temperature, using an EG&G constant acceleration spectrometer and a ^{57}Co (Rh matrix) (10 *mCi*) gamma radiation source. The velocity scale was calibrated from the magnetic sextet of a high purity iron foil absorber. Experimental data were fitted to Lorentzian lines by using a least square based method. The quality of the fit was controlled by the classical χ^2 test. All isomer shifts are given relative to the center of the α–Fe spectrum at room temperature. The measurements at low temperatures were carried out in Universidad de Córdoba, using a CRYOGENICS cryostat coupled to a CRYO.CON temperature controller.

2.2.3 *Results and discussion*

The XRD patterns of the annealed samples revealed a set of reflections which could be indexed to the well-known spinel structure of this ferrite (Fig. 2.2.1).

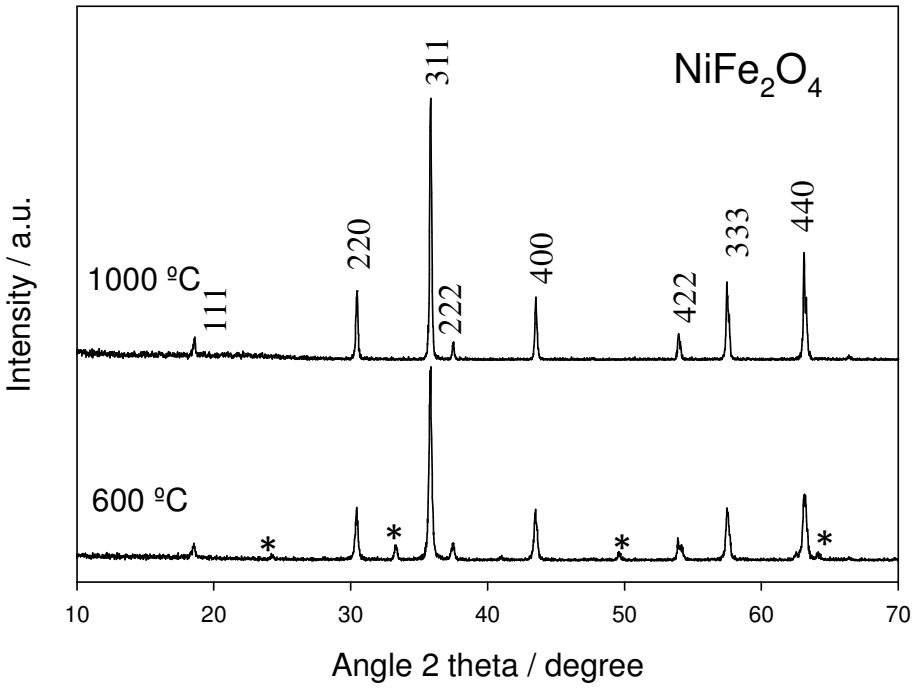

Figure 2.2.1. X-ray diffraction patterns of $NiFe_2O_4$ annealed at 600 and 1000º*C*.

Minor impurities ascribable to hematite were observed for the sample prepared at 600º*C* (marked with an asterisk). Their presence was not much concerning because of the amorphization process occurring during the first discharge in conversion reactions. Also, the presence of Fe^{3+} in both ferrite and hematite structure evenly contributes to the delivered capacity. Recently, we have reported results on the related compound $CuFe_2O_4$ in which the content of impurities of the original samples was less relevant for the electrochemical performance.[15] On increasing the annealing temperature for a narrowing of the reflection can be closely

related with an increase of the crystallite size and a decrease of lattice strains when structural defects are removed.

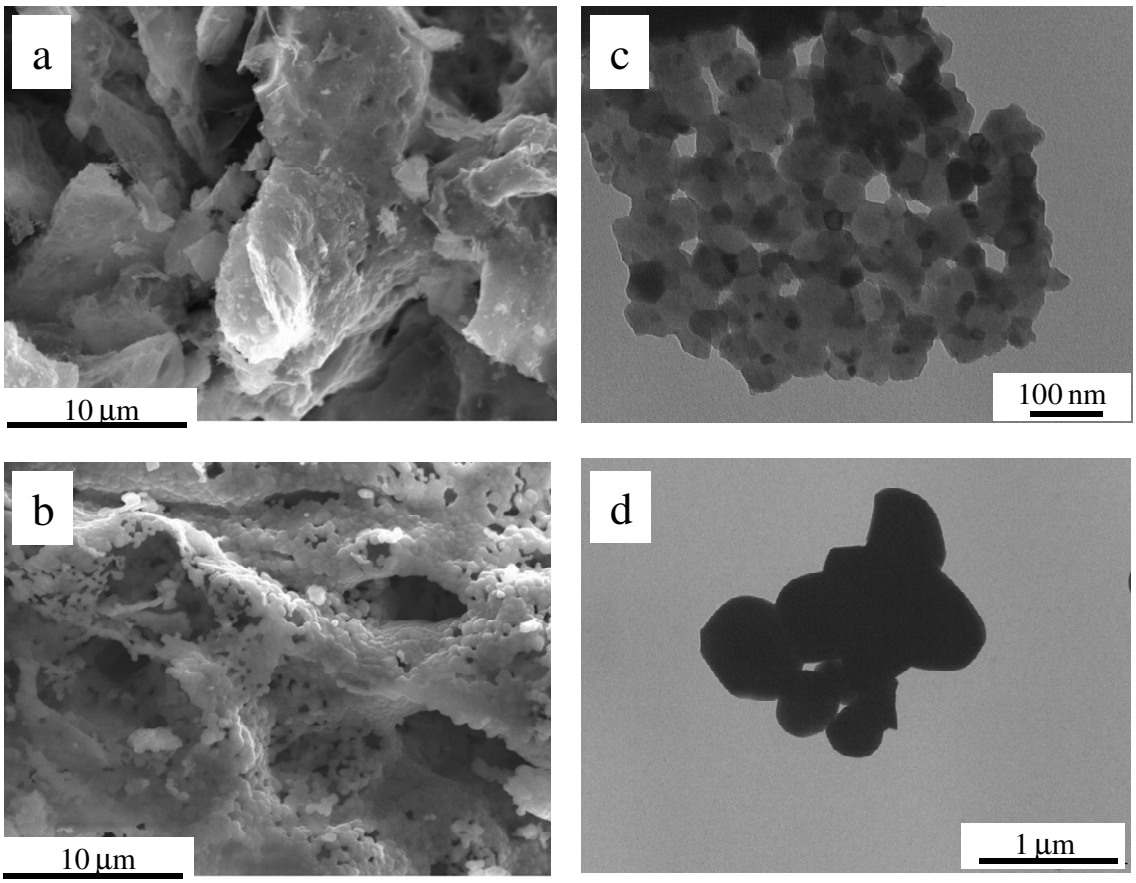

Figure 2.2.2. Electron microscope images of $NiFe_2O_4$ samples. SEM micrographs of samples annealed at a) 600°*C* and b) 1000°*C*. TEM micrographs of samples annealed at c) 600°*C* and d) 1000°*C*.

On increasing the annealing temperature, the reflections become narrower as a consequence of the increase in crystallite size exerted by crystallization. SEM images of the pristine materials revealed a layered morphology irrespective of the annealing temperature (Fig. 2.2.2a, b). In fact, the flakes are secondary particles resulting from the aggregation of submicrometer particles as observed from TEM images. Their size increases with temperature as expected from crystallization phenomena (Fig. 2.2.2c, d). Their average sizes agreed much better with the crystallite size values calculated from XRD data. These values were 74

and 405 *nm* for the samples annealed at 600 and 1000º*C*, respectively. This particular morphology, in which primary particles are mutually interconnected, has been considered beneficial for the electrochemical performance. It assures a suitable electrical conductivity and mechanical strength on a long extended electrode cycling.[7-8] Increasing the annealing temperature preserved the flake-like texture but enlarged the size of the primary particle, as expected from the crystallization phenomenon.

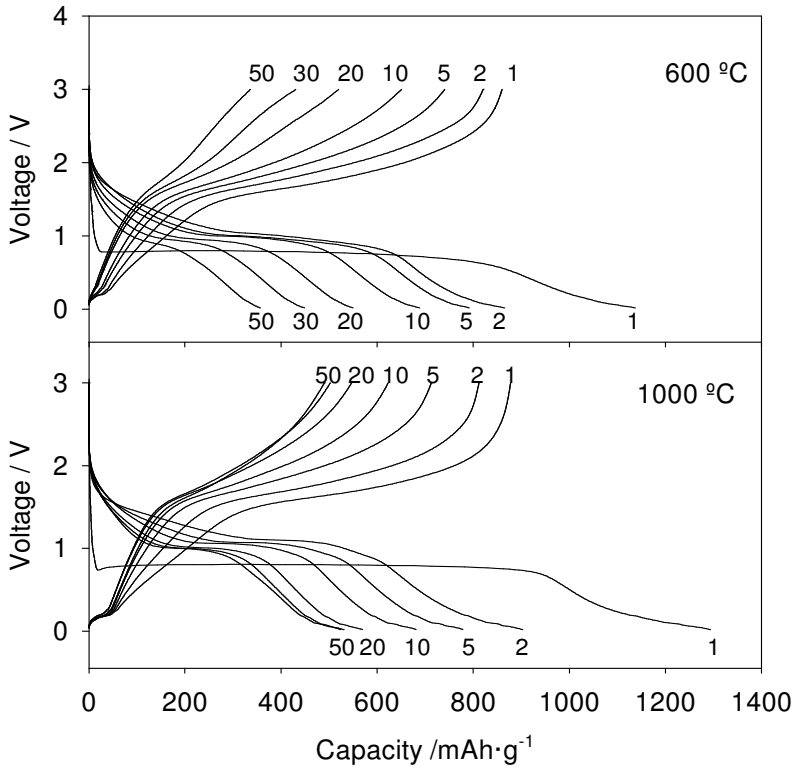

Figure 2.2.3. Voltage versus capacity plots of $NiFe_2O_4$ annealed at a) 600º*C*; b) 1000º*C*. Lithium cells were galvanostatically cycled at 1C.

The Mössbauer spectra of raw materials are characterized by two sextets (Fig. 2.2.4a), related to the ferrimagnetic character of well crystallized samples. The isomer shift values agree with the presence of Fe^{3+} and each sextet corresponds to iron atoms at octahedral and tetrahedral locations of the spinel framework. The equivalent contribution of both

iron sites revealed the fully inverse spinel structure commonly found in the literature.[16, 17]

Figure 2.2.3 shows the charge and discharge curves for some selected galvanostatic cycles. The main features of these curves are related to the occurrence of a quasi-plateau around 1 V, ascribed to transition metals reduction, and an eventual sloping voltage with a pseudo-capacitive behavior. The extent of the first discharge quasi-plateau was of 819 and 903.5 $mAh.g^{-1}$ for the samples annealed at 600 and 1000ºC, respectively. These values are close to the theoretical value 914 $mAh.g^{-1}$, though kinetic hindering, mainly for the 600ºC sample, would involve an incomplete reduction. The profile of the first discharge significantly changes in further cycles due to the severe evolution of the site energy upon the structural degradation above mentioned.[9] The most remarkable differences between these samples annealed at different temperatures are the higher first discharge capacity value and better capacity retention for the sample prepared at 1000ºC. Because the conversion reaction affects to the local environment and oxidation states of the transition metals, these differences in the electrochemical performance should be reflected in the Mössbauer spectra of the cycled electrodes.

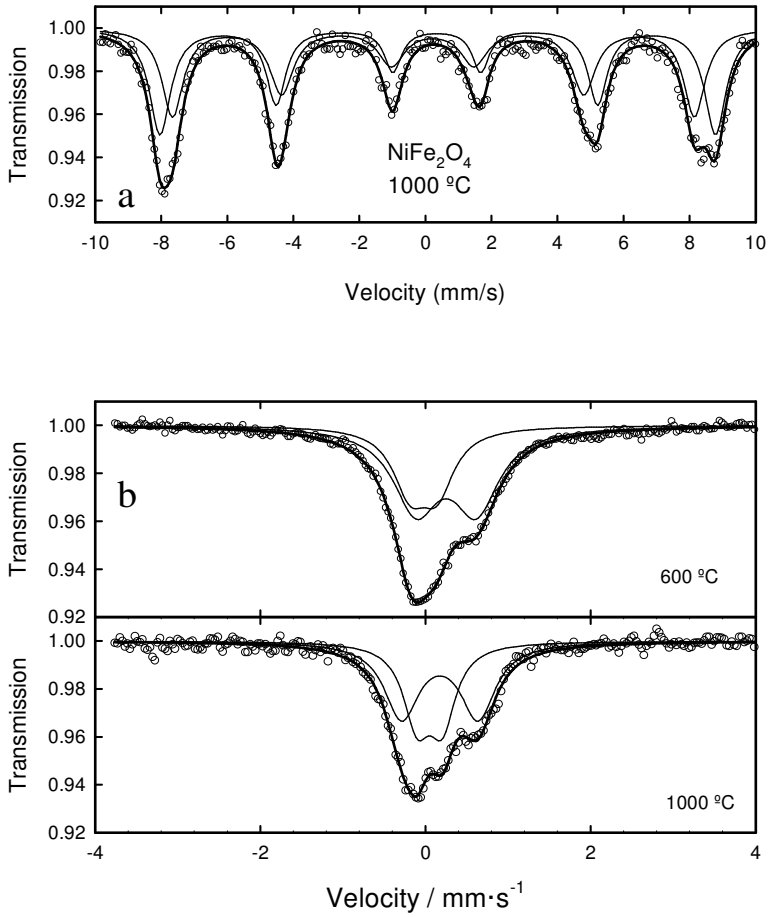

Figure 2.2.4. ^{57}Fe Mössbauer spectra of a) raw $NiFe_2O_4$ annealed at 1000°C. and b) $NiFe_2O_4$ annealed at 600 and 1000°C discharged electrodes.

^{57}Fe Mössbauer spectra of electrodes discharged at 0.02 V recorded at room temperature showed an asymmetric profile resolved which could be fitted as two doublets (Fig. 2.2.4b). These signals are commonly interpreted in terms of a superparamagnetic material in which iron atoms are located in the core (lower quadrupolar splitting) and the surface (higher quadrupolar splitting) of metallic nanometric particles.[18,19] During cell discharge, the enhanced structural degradation leading to nanometric iron particles separated by paramagnetic Li_2O gradually increases the interparticle distance and hence the interparticle magnetic dipole interaction decreases. In consequence, the magnetic moments in the nanometric iron particles are decoupled decreasing the

energy barrier to overcome by the magnetization vector of a superparamagnetic particle. Thus, the fluctuation of the magnetization vector in individual particles will be favored by the interparticle magnetic decoupling, and particles are in the superparamagnetic state. The isomer shift values of the signal ascribable to core iron is near 0 $mm.s^{-1}$ involving an efficient electrochemical metal reduction. Nevertheless, surface iron atoms are characterized by isomer shift values slightly higher than 0 $mm.s^{-1}$. This fact can be assigned to either parallel metal oxidation of surface atoms in contact with electrolyte traces or a low efficient electrochemical reduction. The latter factor could be inferred from the experimental capacity values lower than the theoretical one.

Table 2.2.I. Hyperfine parameters of raw and cycled $NiFe_2O_4$ samples recorded at 298 and 12 K.

Sample	Cycle	Recording Temp. (°K)	[a]δ (mm/s)	[b]Δ (mm/s)	[c]Γ (mm/s)	[d]B_{hf} (T)	[e]C (%)	[f]χ^2
1000 °C	Raw	298	0.36(2) 0.24(3)	0.01(1) 0.01(1)	0.74(5) 0.83(6)	52.3(1) 49.2(1)	45.7 54.3	0.613
600 °C	1st discharge	298	-0.02(2) 0.25(1)	0.33(2) 0.73(2)	0.50(3) 0.67(2)	-- --	35.5 64.5	0.458
1000 °C	1st discharge	298	0.05(1) 0.17(1)	0.31(1) 0.92(2)	0.39(3) 0.51(3)	-- --	43.9 56.1	0.540
600 °C	1st discharge	12	0.21(4) 0.25(4)	0.01(2) 0.00(2)	0.80(9) 1.06(1)	35.7(2) 31.0(2)	39.7 60.3	0.475
600 °C	10th discharge	12	0.19(2) 0.3(1)	0.01(1) 0.09(5)	0.80(5) 0.8(1)	34.1(1) 27.9(5)	79.9 20.1	0.520
1000 °C	1st discharge	12	0.18(3) 0.16(5)	-0.01(1) 0.04(1)	1.1(1) 1.2(1)	34.8(2) 30.3(3)	48.3 51.7	0.582
1000 °C	10th discharge	12	0.19(3) 0.12(6)	0.01(1) 0.02(2)	1.1(1) 0.6(1)	34.8(2) 30.7(3)	79.3 20.7	0.520
Fe_3O_4	1st discharge	12	-0.01(2) 0.23(2)	-0.14(1) 0.05(1)	0.87(6) 1.02(5)	33.9(1) 34.1(1)	42.1 57.9	0.615

[a] δ: isomer shift; [b] Δ: quadrupolar splitting; [c] 2Γ: full line width at half maximum; [d] B_{hf}: Hyperfine magnetic field; [e] C: contribution to total absorption; [f] χ^2: goodness of the fitting.

For the sample annealed at 1000 °*C*, the spectra revealed that surface atoms appear more reduced, as evidenced by their lower isomer shift (Table 2.2.I). This behavior could be correlated to a more effective electrochemical reaction with lithium and correspondingly a better performance, as was previously reported.[7] The contribution values of surface atoms was lower for this sample as expected from the larger particle size.

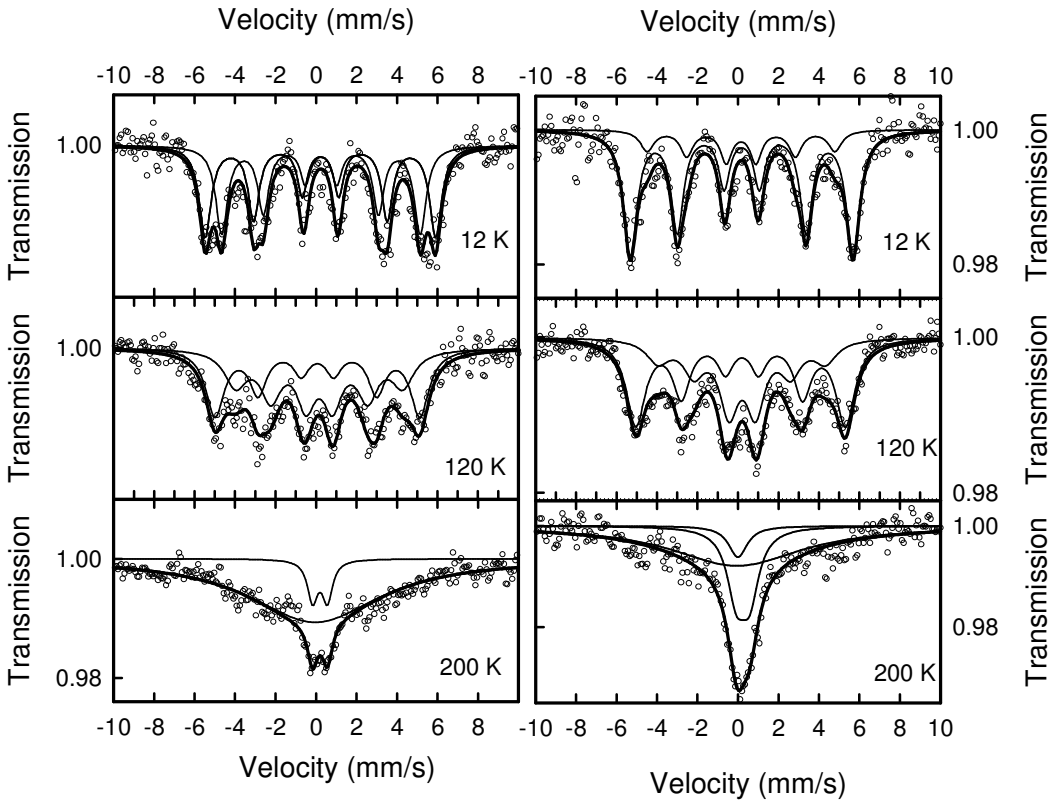

Figure 2.2.5. ^{57}Fe Mössbauer spectra of cycled $NiFe_2O_4$ (600 °*C*) electrodes after a) 1 discharge and b) 10 discharges. The spectra were recorded at 12, 120 and 200 *K*.

On decreasing the recording temperature, the thermal energy is insufficient to allow the magnetization vectors to overcome the energy barrier. Consequently, the magnetization coupling between particles appears and sextets are again observed. The spectra were recorded for $NiFe_2O_4$ samples annealed at 600 and 1000°*C* after one and ten discharges. The recording temperatures were selected at 12, 120 and 200 *K* in order to observe the superparamagnetic-ferrimagnetic transition. In all cases, the doublets become two sextets when the recording temperature was decreased (Fig. 2.2.5 and 2.2.6). These signals are better resolved that the doublets recorded at room temperature. Anyway, the contributions of these sextets (Table 2.2.II) fairly match with those of the superparamagnetic doublets indicating that the decomposition of the asymmetric profile according to the reported

signals was correct. We can assume that the thickness of the atomic surface layer on a spherical particle is approximately equivalent to four iron atoms (5.04 *Å*). According to the contribution values on tables 2.2.I and 2.2.II, they correspond to approximately 50% of the overall area of the Mössbauer spectrum. An easy geometrical calculation leads to an eventual particle diameter of ca. 5 *nm*. This value agrees with previous data reported by Klabunde et al.[20] It also agrees with the particle diameter reported for the metallic particles observed in discharged electrodes of $CoFe_2O_4$.[21] An evidence of the formation of a bimetallic Ni-Fe alloy could not be inferred from the hyperfine field data. It is assumed that the hyperfine field increases by 0.94 *T* when one Ni atom substitutes iron atom in the first coordination sphere and by 0.7 *T*, in the second sphere for *bcc* Fe–Ni alloys.[22] Such an increment in the hyperfine field was not observed when the spectra of a electrochemically reduced magnetite, in which Ni atoms are absent, was compared with any of the $NiFe_2O_4$ discharged electrodes.

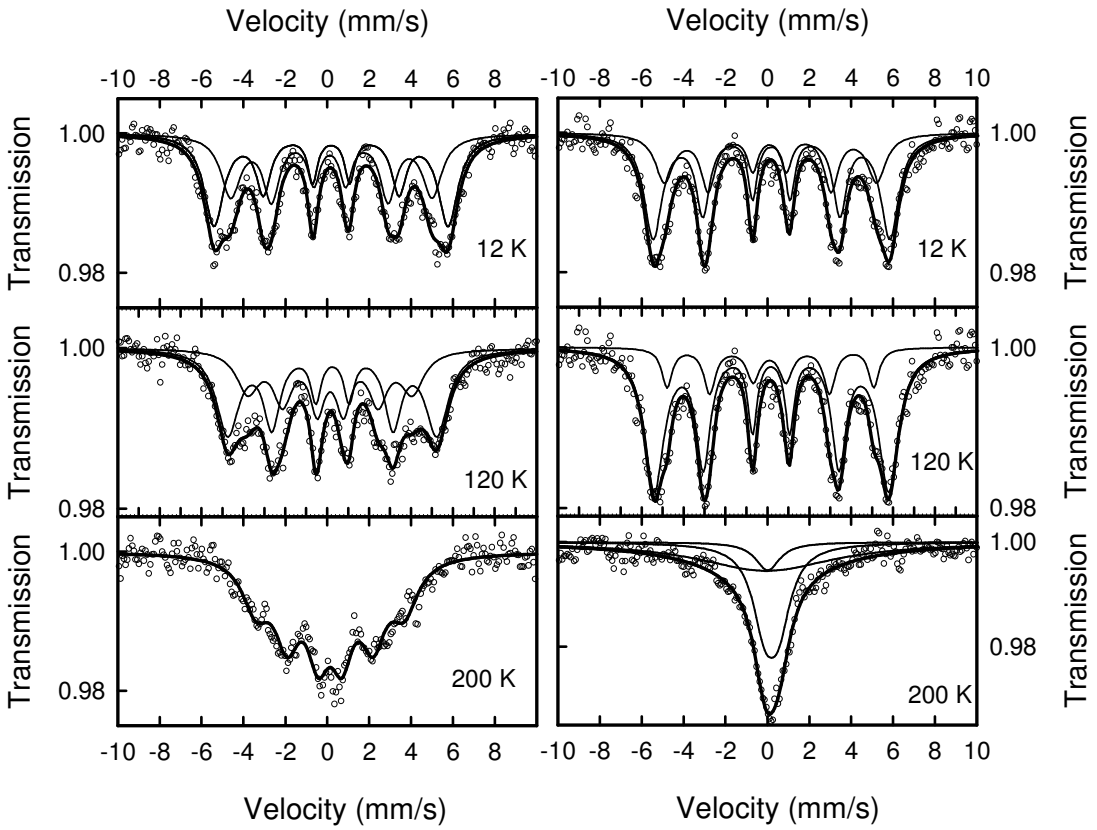

Figure 2.2.6. ^{57}Fe Mössbauer spectra of cycled $NiFe_2O_4$ (1000 °*C*) electrodes after a) 1 discharge and b) 10 discharges. The spectra were recorded at 12, 120 and 200 *K*.

Figures 2.2.5a and 2.2.6a show the Mössbauer spectra recorded at several temperatures for $NiFe_2O_4$ samples after the first discharge. The progressive disappearance of the sextets was observed for both annealing temperatures when the recording temperature was increased. However, this effect is more enhanced for the $NiFe_2O_4$ sample annealed at 600°*C*, in which the ferrimagnetic contribution could only be fitted to a highly broadened band. Consequently, a higher blocking temperature for the sample prepared at 1000 °*C* can be inferred. A direct relationship between the particle size and magnetic properties is well established.[23] The electron spin cooperation in a large particle will counterbalance the thermal motion of the particle favoring the ferromagnetic character, while superparamagnetic relaxation will prevail in small particles. Bearing in mind this assumption, smaller metallic particles can be

expected for the sample prepared at 600º*C*. The sextet characterized by the lowest hyperfine field is more affected by temperature. From 12 to 120 *K*, the change of its relative intensities seems to indicate that is prone to be converted in the superparamagnetic doublet at low temperatures. For this reason, the sextet could be ascribed to either surface iron atoms or the smallest particles which are more prone to undergo superparamagnetic relaxation even at extremely low temperatures. This statement was confirmed by recording high resolution images of the discharged electrodes. The images are characterized by agglomerations of dark particles in a mosaic-like texture which has been extensively reported as belonging to electrochemical reduced metal nanoparticles embedded in a Li_2O matrix.[19, 24] A visual inspection of the images in figure 2.2.7 evidences a coarse grain for the sample prepared at 1000ºC. This fact would agree with the Mössbauer results above mentioned.

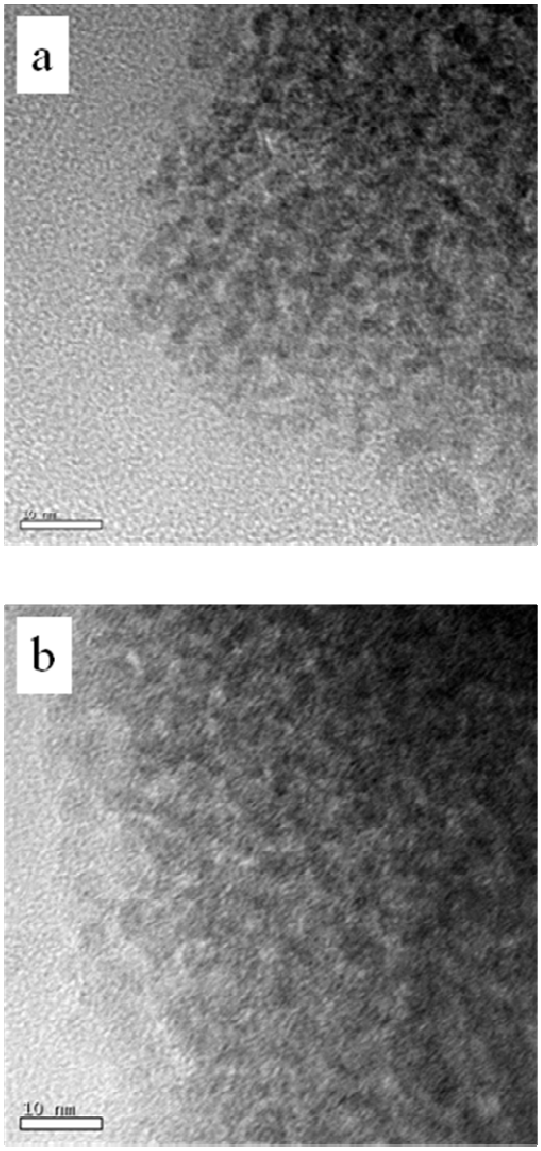

Figure 2.2.7. High resolution images from transmissions electron microscopy of $NiFe_2O_4$ electrodes after one discharge. Raw samples were annealed at a) 600º*C*; (b) 1000º*C*.

The most relevant effect of cycling on the ^{57}Fe Mossbauer spectra recorded at 200 *K* is a significant contribution of the superparamagnetic doublets after 10 cycles as compared to the profiles recorded after only one discharge (Fig. 2.2.5b and 2.2.6b). Thus, the electrode cycling seems to provoke an electrochemical grinding that continuously disaggregates the Li_2O/Ni-Fe agglomerations. This phenomenon could be responsible for the capacity fading observed at least during the first ten cycles.

2.2.4 *Conclusions*

$NiFe_2O_4$ samples have been prepared by a sol-gel method for their use as anode materials in lithium ion batteries. The effect of the annealing temperature is reflected in both morphological and electrochemical properties. Thus, the macroporous system formed by the interconnection of submicrometer particles is preserved in the sample annealed at 1000 ^oC while the size of the primary particle was enlarged, which leads to a better capacity retention in lithium test cells.

The ^{57}Fe Mossbauer spectra of cycled electrodes in lithium test cells evidenced an enhanced diminution of particle size evidenced by superparamagnetic relaxation while a ferrimagnetic character was observed in the raw $NiFe_2O_4$ materials. The electrochemical reduction of iron atoms is also revealed. The spectra recorded at 12 K retrieved the ferrimagnetic character whose contribution agrees well with those of the superparamagnetic doublets recorded at room temperature. According to the contribution values, a ca. 5 *nm* particle diameter was calculated in good agreement with electron images on this and related compounds. A higher blocking temperature for the sample prepared at 1000 ^oC was observed, what is correlated with larger metallic iron particles for this reduced sample.

The significant decrease of the blocking temperature observed in the cycled electrodes can be ascribed to a parallel decrease in particle size. Most likely, an electrochemical grinding effect produced during cycling would disaggregate the Li_2O/Ni-Fe agglomerations and provoke capacity fading observed at least during the first ten cycles.

Acknowledgements

We acknowledge the financial support from MEC MAT2008-05880. M. Mohedano for her technical support.The Service of Support to Research at the University of Córdoba provided the electron microscopy equipment.

References

1. Poizot, P. ; Laruelle, S. ; Grugeon, S. ; Dupont, L. ; Tarascon, J. M. *Nature* **2000**, *407*, 496-499.
2. Tirado, J. L. *Mat. Sci. Eng. R* **2003**, *40*, 103-123.
3. Bruce, P. G.; Scrosati, B.; Tarascon, J. M. *Angew. Chem. Int. Ed.* **2008**, *47*, 2930–2946.
4. Li, X.D.; Yang , W.S.; Li, F.; Evans, D.G.; Duan X. *J. Phys. Chem .Solids* **2006**, *67*, 1286–1290.
5. NuLi, Y.N.; Qin, Q.Z. *Journal of Power Sources* **2005**, *142*, 292–297.
6. Zhao, H.; Zheng, Z.; Wong, K.W.; Wang, S.; Huang, B.; Li D. *Electrochem. Commun.* **2007**, *9*, 2606–2610.
7. Lavela, P.; Tirado, J.L. *J. Power Sources* **2007**, *172*, 379-387.
8. Bomio, M.; Lavela, P.; Tirado, J.L. *ChemPhysChem* **2007**, *8*, 1999-2007.
9. Alcántara, R.; Jaraba, M.; Lavela, P.; Tirado, J.L.; Jumas, J.C.; Olivier-Fourcade, J. *Electrochem. Commun.* **2003**, *5*, 16-21.
10. Poizot, P. ; Laruelle, S.; Grugeon, S. ; Tarascon, J. M. *J. Electrochem. Soc.* **2002**, *149*, A1212-A1217.
11. Choi, H.C.; Lee, S.Y.; Kim, S.B.; Kim, M.G.; Lee, M.K.; Shin, H.J.; Lee, J.S. *J. Phys. Chem. B* **2002**, *106*, 9252-9260.
12. Thissen, A.; Ensling, D.; Fernández Madrigal, F. J.; Jaegermann, W.; Alcántara, R.; Lavela, P.; Tirado, J. L. *Chem. Mater.* **2005,** *17*, 5202-5208.
13. Chadwick, A. V.; Savin, S. L. P.; Fiddy, S.; Alcántara, R.; Fernández Lisbona, D.; Lavela, P.; Ortiz, G. F.; Tirado, J. L. *J. Phys. Chem. C* **2007**, *111*, 4636-4642.

14. Lavela, P.; Tirado, J. L.; Womes, M.; Jumas, J. C. *J. Electrochem. Soc.* **2009**, *156*, A589-A594.
15. Bomio, M.; Lavela, P.; Tirado, J.L. *J. Solid State Electrochem.* **2008**, *12*, 729–737.
16. Sui, Y.; Su, W.H.; Zheng, F.L.; Xu, D.P. *Mater. Sci. Eng., A* **2000**, *A286* , 115–118
17. Halasa, N.A.; DePasqual, G.; Drickamer, H.G.; *Phys. Rev. B* **1974**, *10*, 154.
18. Obrovac, M. N.; Dunlap, R. A.; Sanderson, R. J.; Dahn, J. R. *J. Electrochem Soc.* **2001**, *148*, A576-A588.
19. Larcher, D. ; Bonnin, D. ; Cortes, R. ; Rivals, I. ; Personnaz, L. ; Tarascon, J. M. *J. Electrochem. Soc.* **2003**, *150*, A1643-A1650.
20. Glavee, G. N.; Eason, K.; Klabunde, K. J.; Sorensen, C.M.; Hadjipanayis, G. C. *Chem. Mater* **1992**, *4*, 1360-1363.
21. Lavela, P.; Tirado, J. L.; Womes, M.; Jumas, J. C.; *J. Phys. Chem. C* **2009**, *113*, 20081–20087.
22. E. Jartych, *J. Magn. Magn. Mater.* **2003**, *265*, 176–188.
23. Ma, Y.G.; Jin, M.Z.; Liu, M.L.; Chen, G.; Sui, Y.; Tian, Y.; Zhang, G.J.; Jia, Y.Q. *Mat. Chem. Phys.* **2000**, *65*, 79–84.
24. Débart, A. ; Dupont, L. ; Poizot, P. ; Leriche, J.B. ; Tarascon J.M. *J. Electrochem. Soc.* **2001**, *148*, A1266-A1274.

2.3. A ^{57}Fe Mössbauer spectroscopy study of cobalt ferrite conversion electrodes for Li-ion batteries

Candela Vidal-Abarca, Pedro Lavela, José L. Tirado*

Laboratorio de Química Inorgánica, Universidad de Córdoba,Edificio Maire Curie, planta 1, Campus de Rabanales, 14071 Córdoba, Spain

Abstract

The reverse micelles method has been employed to obtain cobalt ferrite samples. The effect of the type of surfactant and volumetric proportion of the aqueous and organic phases on the electrochemical behavior has been evaluated. The sample prepared using Span 80 as a surfactant and equivalent volumes of the aqueous and organic phases showed the highest capacity values and rate capabilities. It has been correlated to the better stability of the faradaic conversion process upon cycling for this sample. Based on the ^{57}Fe Mössbauer spectra of discharged electrodes, this result has been associated to the preservation of reduced iron atoms into the core of the particles. The metallic atoms are ready to be oxidized, thus sustaining the reversible electrochemical reaction in further cycles.

Journal of Power Sources 196 (2011) 6978–6981

**corresponding author*

2.3.1 *Introduction*

Transition metal oxides and oxysalts display interesting conversion reactions in lithium cells.[1] The effective reversible reduction of metal atoms from the initial oxidation state to the metallic state involves the transfer of several electrons. This is the main advantage of these electrode materials. Reversible capacities close to twice the theoretical capacity of graphite are commonly observed, which gives these materials a potential applicability in lithium-ion batteries.[2] The electrochemical reversibility of these reactions has been ascribed to the nanometric size of the particles of the products (M and Li_2O).[3] It ensures an extremely large interface which facilitates the slow oxide ion migration between the metal atoms. Nevertheless, the significant polarization between charge and discharge branches and high irreversible capacities in the first cycle jeopardizes their practical use.

Recently, it has been shown the interest of ternary oxides as $Co_{3-x}Fe_xO_4$ (x = 0, 1, 2) or the$Mn_xCo_{3-x}O_4$ series (x: 1, 1.5, 2, 3) to tune the anode working voltage.[4,5] The presence of two different transition metals leads to a unique reduction plateau whose potential depends on the stoichiometry and the metal present in the composition. Also, the morphology of both primary particles and their agglomerates has a notorious influence on the electrochemical performance.[6,7] Therefore, the analysis of new method of synthesis affecting to the size and shape of the particles may lead to new materials with optimized electrochemical properties.[8,9] In this way, the reverse micelles method is an alternative preparation route based on the use of organic anionic surfactants that stabilize reverse (water-in-oil) micelles.[10,11] The transition metal solution reacts within the small aqueous droplets to yield a solid precursor.

In order to develop new methods to limit the main drawbacks, a first step is always a good understanding of the reaction mechanisms. For this purpose, ^{57}Fe Mössbauer spectroscopy (MS) has proven to be a relevant tool in the study of iron containing oxides.[12,13] In this communication we discuss the mechanism of reduction-reoxidation of $CoFe_2O_4$ in lithium test cells, by using MS.

2.3.2 *Experimental*

The precursor formation undergoes by the coalescence of two different reverse micelles containing aqueous solutions of metal chlorides as a metal source and 8M NaOH solution as precipitating reagent. The reverse micelles were stabilized by stirring the aqueous solution in an organic phase in the presence of a surfactant. The organic phase selected for this procedure was hexane. The aqueous to organic volume ratio was allowed to vary from 1:1 to 1:2. Span 80 and Tween 85 surfactants were used. The precursors were eventually annealed in air at 800 ºC for 15 hours. Samples will be named as CoFeXA:B (X: S or T for the surfactant; A:B for the Aqueous:Organic phase ratio). Thus, samples will be named as CoFeS1:1, CoFeS1:2 and CoFeT1:1.

X-ray diffraction (XRD) patterns were recorded in a Siemens D5000 diffractometer, with a Cu Kα radiation and a graphite monochromator. SEM images were obtained with a JEOL-SM6300 microscope. An EG&G constant acceleration spectrometer and a ^{57}Co (Rh matrix) gamma radiation source were used for recording ^{57}Fe Mössbauer spectra in transmission mode at room temperature. The magnetic sextet recorded from a high purity iron foil was used to calibrate the velocity

scale. Experimental data were fitted to Lorentzian lines by using a least square based method.[14]

Battery tests were carried out by using two-electrodes Swagelok type cells. Counter electrodes were 9 *mm* discs of lithium metal and the working electrode consisted of a mixture of 75 % of active material and 10 % of graphite, 10 % of carbon black and 5% of PVDF binder were coated on a cooper foil of the same diameter. A 1M $LiPF_6$ (EC:DEC = 1:1) electrolyte solution was supported in Whatman glass fiber discs. Galvanostatic tests were carried out on an Arbin galvanostat multichannel system. The imposed kinetic rate was set at 1C for battery testing and C/2 for the discharged electrodes used in the Mössbauer spectroscopy. Step potential electrochemical spectroscopy (SPES) was monitored on a MacPile System.

2.3.3 *Results and discussion*

The XRD patterns of the annealed products were characterized by narrow and intense reflections that can be indexed in the Fd3m space group corresponding to $CoFe_2O_4$ (JCPDS 03-0864) (Fig. 2.3.1). The presence of impurities was discarded. The reflections of the CoFeS1:1 sample are less broadened what is related to the higher crystallinity of this sample.

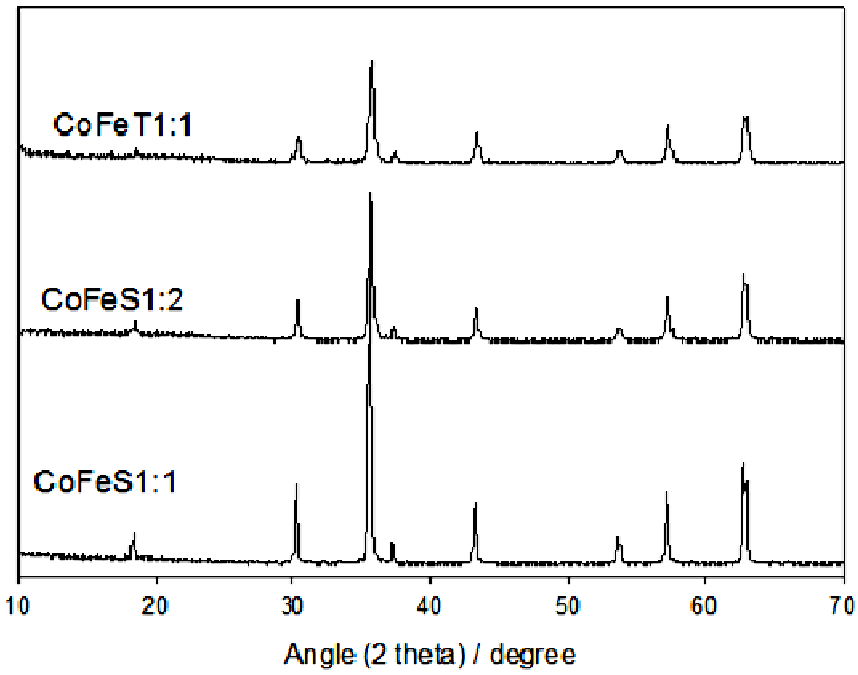

Figure 2.3.1. XRD patterns of the annealed samples.

The analysis of the SEM images showed the occurrence of large agglomerates of primary particles (Fig. 2.3.2). It evidenced a close similarity between the oxides prepared using Span 80 as a surfactant irrespective of the volume ratio of aqueous and organic phases. They were constituted by submicron particles. Contrarily, the use of Tween 85 as a surfactant involved the presence of large primary particles with a micrometric size. This different morphology would influence undoubtedly on the electrochemical behavior, since lithium reacts with the electrode material migrating from the surface to the core particle.

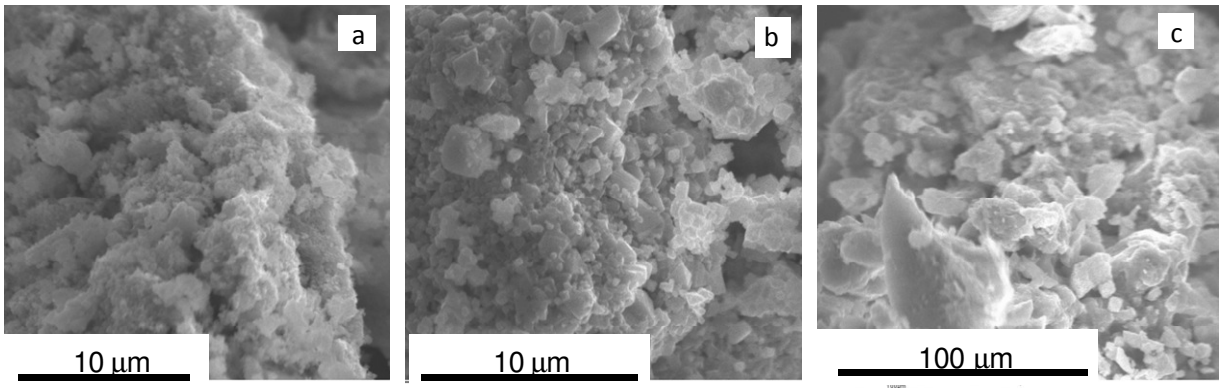

Figure 2.3.2. SEM images of $CoFe_2O_4$ samples with a) CoFeS1:1; b) CoFeS1:2 and c) CoFeT1:1

The electrochemical lithium driven conversion reaction can be decomposed in two different processes. First, a faradaic process involves the complete reduction of the metal atoms. This effect is identified by an extended plateau which voltage is located slightly higher than 1 V for the cobalt ferrite. Then a pseudo-capacitive process appears as a sloping voltage feature until the end of discharge. The relative contribution of both processes depends on several factors as the sweep rate. Figure 2.3.3 shows the SPES results obtained at different rates, v, for sample CoFeS1:1, which were used to calculate the relative contributions by using the method developed by Dunn and coworkers.[15,16]

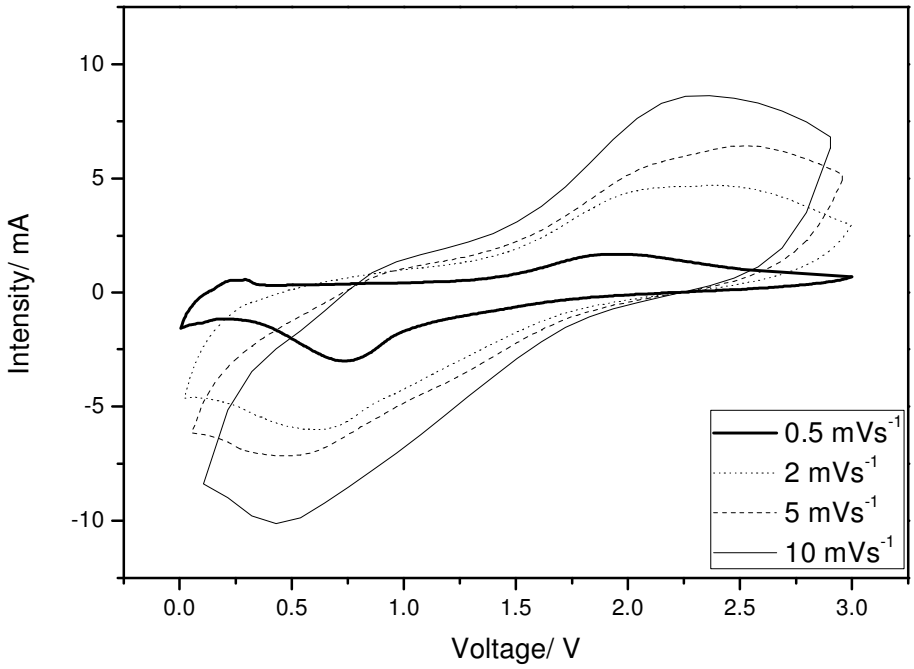

Figure 2.3.3. SPES results at different rates for sample CoFeS1:1

A linear relationship was found between the intensity measured at different voltages by using equation (1).

$$i(V)/v^{1/2} \longrightarrow k_1 v^{1/2} + k_2 \qquad (1)$$

where constants k_1 and k_2 are related to current contributions from surface capacitive and diffusion-controlled Faradaic effects, respectively. As can be seen in Table 2.3.I, the contribution of the faradaic reaction increases with the sweep rate from 2 $mV.s^{-1}$ what evidences the importance of this process to favor high rate capabilities.

However, for slow rates of 0.5 $mV.s^{-1}$ this tendency is reverted probably due to the higher contribution of other electrochemical processes, such as reactions with the electrolyte which are kinetically hindered at higher rates.

Table 2.3.I. Relative contributions of faradaic and capacitive processes to the total discharge capacity at different sweep rates for CoFeS1:1.

Sweep rate(mVs-1)	Capacitive(%)	Faradaic(%)
0.5	17.85	82.15
2	36.46	63.54
5	16.95	83.05
10	14.24	85.76

For electrochemical characterizations, voltage profiles with discharge/charge capacities and first cycle efficiency were obtained. The profiles have been included in new figure 2.3.4. The efficiencies were 75.8, 74.4 and 73.4 % for CoFeS1:1, CoFeS1:2 and CoFeT1:1, respectively.

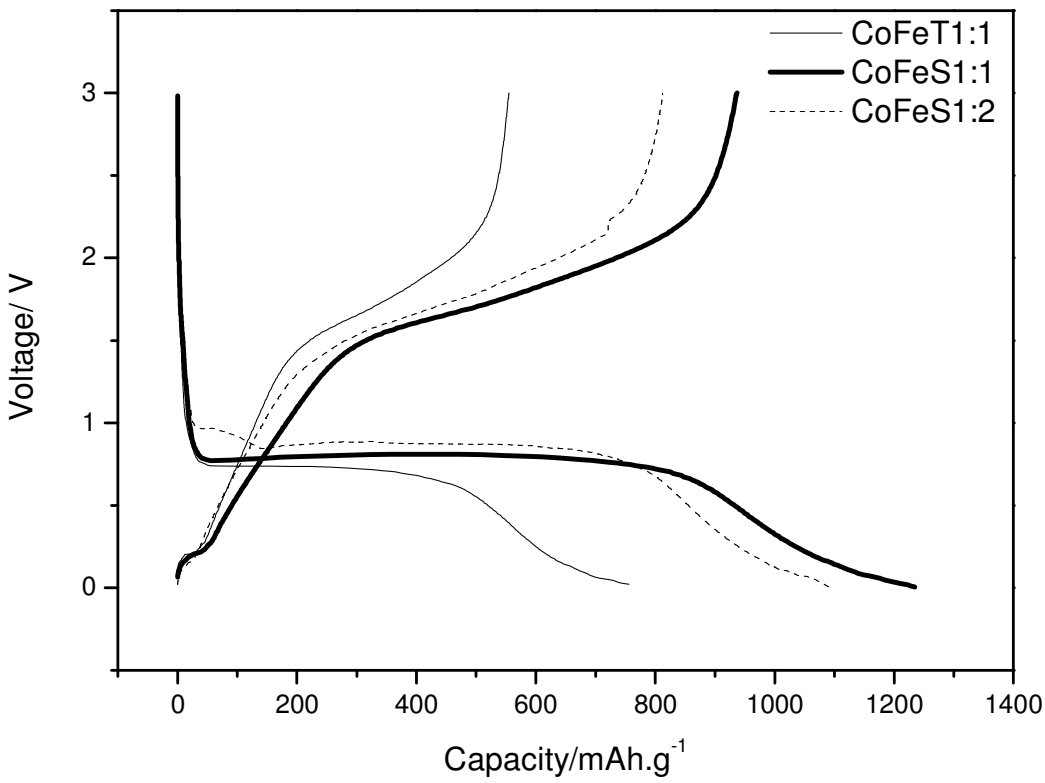

Figure 2.3.4. Voltage profiles with discharge/charge capacities for the studied samples.

The extended galvanostatic cycling reveals quite different behavior for the obtained samples despite of the equivalent composition (Fig. 2.3.5). It highlights the importance of morphological and crystallinity differences on the performance of these electrode materials subjected to conversion reactions. Thus, CoFeS1:1 showed the highest capacity retention reaching capacity values as high as 614 $mAh.g^{-1}$ after 50 cycles.

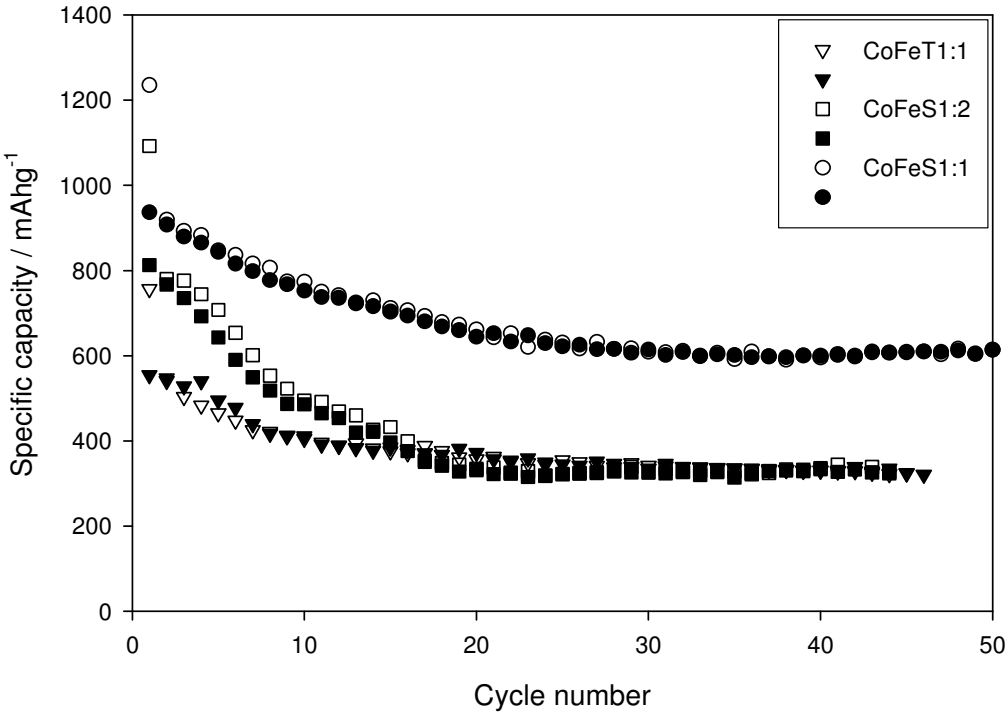

Figure 2.3.5. Galvanostatic cycling of the studied samples (open circles: charge, full symbol: discharge.

In order to understand their different performance the differential capacity plots were displayed in figure 6. The 2nd, 10th, 20th and 40th cycles were plotted to evidence the general behavior upon cycling. The bands are correlated to the galvanostatic quasi-plateaus defining the faradaic process. The positive values correspond to the charging curves. The strongly broadened bands are ascribed to the transition metal oxidation reactions. Unfortunately, their enhanced broadening avoids

description of the different behavior among samples. Contrarily, the anodic process is characterized by narrow signals which evolution upon cycling allows discerning some differences among the studied samples. As a general feature, we observe a progressive shifting of the signals to lower voltages. This effect could be related to an increase of electrode polarization. This effect could be attributed to a decrease of the electronic conductivity due to particle isolation. The capacity fading of CoFeS1:2 and CoFeT1:1 samples can be correlated to the decrease of intensity and enhanced broadening observed in these faradaic signals upon cycling. It undoubtedly reflects the lack of stability of the electrochemical reaction after a large number of cycles.

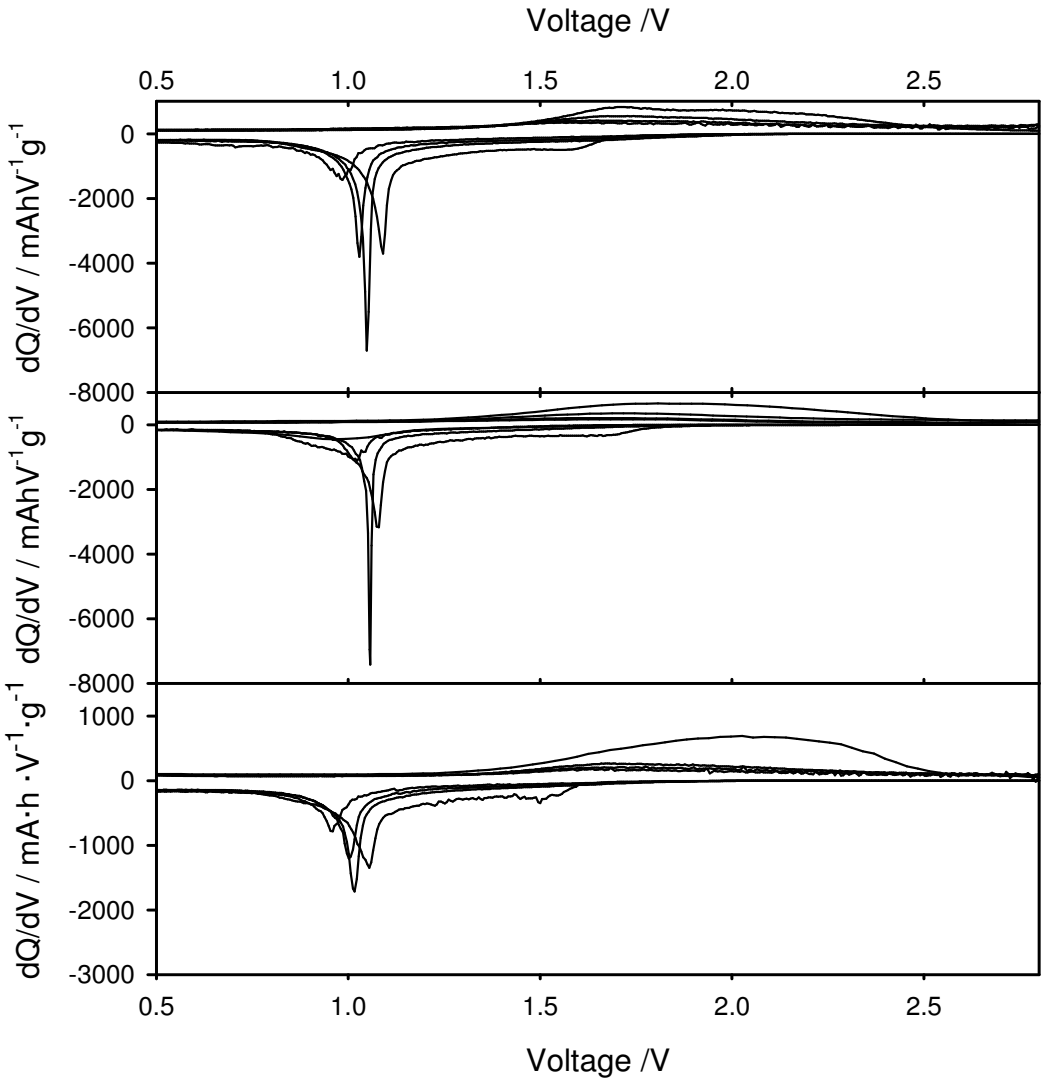

Figure 2.3.6. Differential capacity plots of a) CoFeS1:1; CoFeS1:2; c) CoFeT1:1.

The better stability of the faradaic process can be also evidenced observing the rate capability. Thus, the sample CoFeS1:1 is able to sustain high capacity values when subjected to high C rates (Fig. 2.3.7). Nevertheless, an enhanced decrease in capacity was recorded for this sample when discharged at 5C.

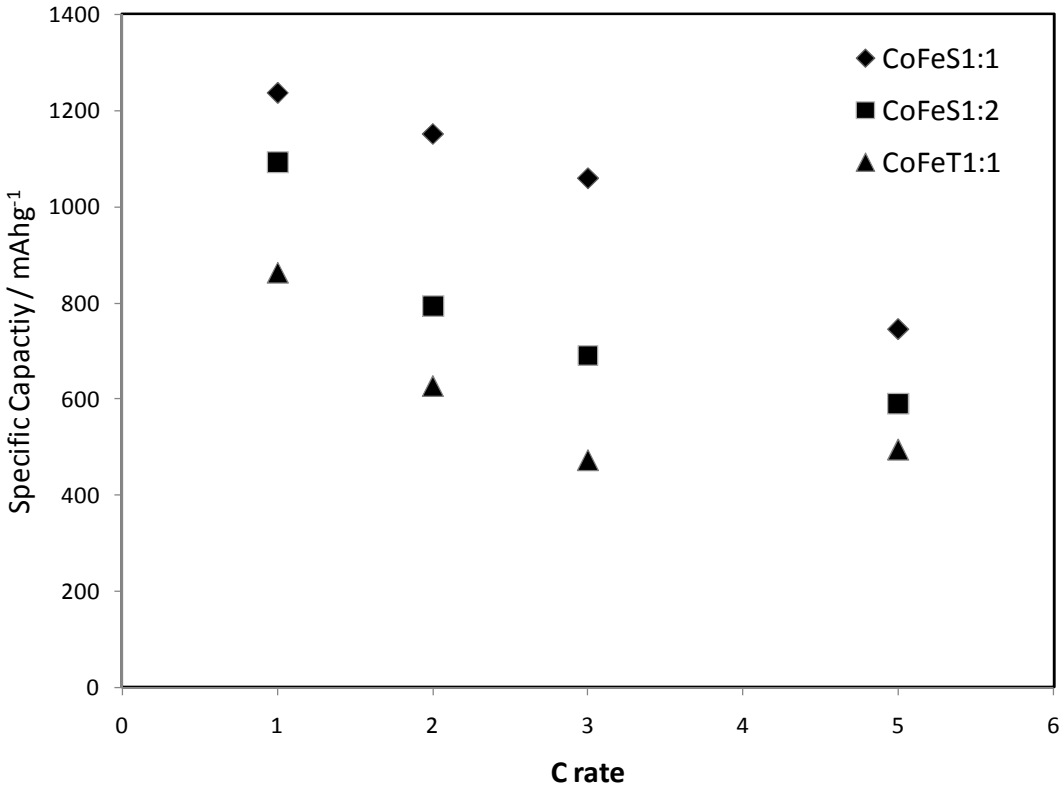

Figure 2.3.7. Plot of specific capacity values recorded for the first discharge at several kinetic rates.

The ^{57}Fe Mössbauer spectra of CoFeS1:1 discharged electrodes can be decomposed into a doublet and a singlet revealing the superparamagnetic character of the metallic Fe obtained upon the electrochemical reduction (Fig. 2.3.8).

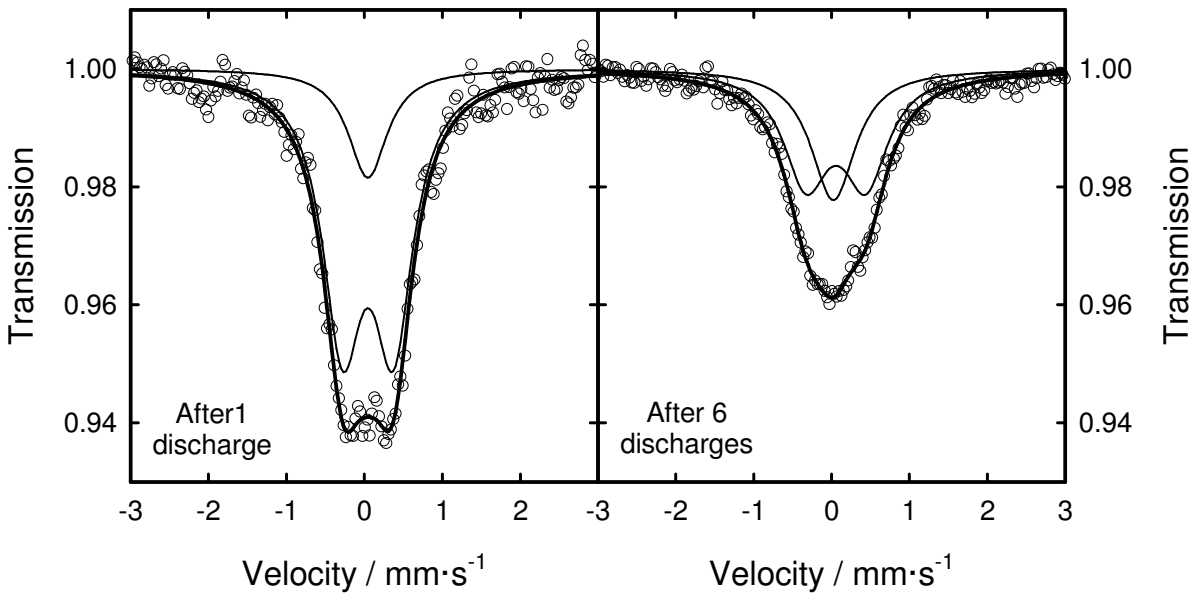

Figure 2.3.8. ^{57}Fe Mössbauer spectra of CoFeS1:1 electrodes recorded after a) one and b) six discharges.

The isomer shift values ranging between 0.0-0.07 $mm.s^{-1}$ confirm the effective reduction of the transition metal. The singlet is commonly assigned to Fe atoms located at the core of the particles, while the doublet is attributed to those placed on the surface. Moreover, the isomer shift value of the latter doublet is usually higher than that of core iron atoms. It has been attributed to the contact of surface iron atoms with the electrolyte favoring undesirable oxidation side reactions with the electrolyte which increase their average oxidation state and also enhances the irreversibility of the electrochemical reaction. Otherwise, core iron atoms are preserved from these side reactions and contribute positively to the reversibility of the redox reaction. In fact, a decrease in the relative contribution of the singlet upon cycling has been correlated to the capacity fading in related electrode materials.[7] Therefore, the high contribution of core iron atoms to the overall

spectrum after six cycles in CoFeS1:1 may explain its high capacity retention after a large number of cycles.

2.3.4 *Conclusions*

The reverse micelles method is a suitable route to prepare anode materials undergoing electrochemical conversion reactions. The appropriated selection of the synthesis conditions, namely type of surfactant and aqueous/organic phase volume ratio, leads to electrode materials with optimized electrochemical performance. $CoFe_2O_4$ sample prepared by using Span 80 as a surfactant and a ratio of 1:1 showed the highest capacity values (614 $mAh.g^{-1}$) after a large number of cycles. The contribution of the faradaic process to the electrochemical performance during the galvanostatic cycling has demonstrated to be essential. This effect has been correlated to the preservation of metallic iron atoms into the core of the particles in the discharged electrodes. These atoms are preserved from irreversible reactions with the electrolyte and hence they promote the high reversibility and rate capability of CoFeS1:1 sample.

Acknowledgments

We appreciate the financial support from the MICINN (Contract MAT2008-0558) and Government of Andalusia (Project FQM1447, group FQM288). CV is grateful to MICINN for a FPI grant. We also want to thank the Central Support Service for Research at the University of Cordoba.

References

1. Aragón M. J., Lavela P., León B., Pérez-Vicente C., Tirado J.L., Vidal-Abarca C., *J Solid State Electrochem*. **2010**, 14, 1749.

2. Lavela P., Tirado J.L., *J. Power Sources*. **2007**, 172, 379.

3. Poizot P., Laruelle P. S., Grugeon S., Dupont L., Tarascon J. M., *Nature* **2000**, 407, 496.

4. Lavela P., Ortiz G. F., Tirado J. L., Zhecheva E., Stoyanova R., Ivanova Sv., *J. Phys. Chem. C* **2007**, 11, 38, 14238.

5. Lavela P., Tirado J.L., Vidal-Abarca C., *Electrochim. Acta*. **2007**, 52, 7986.

6. Fan Q., Whittingham M. S., *Electrochem. Solid-State Lett*. **2007**, 10, A48.

7. Gillot F., Boyanov S., Dupont L., Doublet M. L., Morcrette M., Monconduit L., Tarascon J. M., *Chem. Mater*. **2005**, 17, 6327.

8. Akl J., Ghaddar T., Ghanem A., El-Rassy H., *J. Mol. Catal. A: Chem*. **2009**, 312.

9. Grugeon S., Laruelle S., Herrera-Urbina R., Dupont L., Poizot P., Tarascon J.M., *J. Electrochem Soc*. **2001**, 148, A285.

10. Wang G.X., Chen Y., Yang L., Yao J., Needham S., Liu H.K., Ahn J.H., *J. Power Sources* **2005**, 146, 487.

11. Vidal-Abarca C., Lavela P., Tirado J. L., *Electrochem. Solid-State Lett.*, **2008**, 11, A198.

12. Lavela P., Tirado J.L., Womes M., Jumas J.C., *J. Electrochem. Soc.* **2009**, 156, A589.

13. Lavela P., Tirado J.L., Womes M., Jumas J.C., *J. Phys. Chem. C.* **2009**, 113, 20081.

14. Kündig W., *Nuclear Instr. Methods*, **1969**, 75, 336.

15. Wang J., Polleux J., Lim J., Dunn B., *J. Phys. Chem. C.* **2007**, 111, 14925.

16. Brezesinski T., Wang J., Polleux J., Dunn B., Tolbert S.H., *J. Am. Chem. Soc.* **2009**, 131, 1802.

Capítulo 3

Fosfatos para cátodos de inserción

3.1. Improving the cyclability of sodium-ion cathodes by selection of electrolyte solvent

C. Vidal-Abarca, P. Lavela, J.L. Tirado*

Laboratorio de Química Inorgánica, Universidad de Córdoba, Edificio Maire Curie, Planta 1, Campus de Rabanales, 14071 Córdoba, Spain

A.V. Chadwick, M. Alfredsson

Functional Materials Group, School of Physical Sciences, University of Kent, Canterbury, Kent CT2 7NR, U.K.

E. Kelder

NanoStructured Materials, Department of Chemical Engineering, TUDelft, 2628BL Delft, The Netherlands

Abstract

A composite material containing orthorhombic $Na_{1.8}FePO_4F$ and carbon is prepared by mechanical activation and ceramic procedures. The material is studied in sodium test cells as a potential candidate for sodium-ion battery cathodes. The effect of the solvents in the electrolyte on the electrochemical performance is analysed by X-ray absorption spectroscopy. The structural changes on cycling are small, while the changes in the oxidation state of iron agree with the sodium insertion-extraction processes. The oxidation state is especially affected by the upper limit of the voltage window, and the discharge capacity is strongly affected when using propylene carbonate solvent. Capacity and capacity retention are higher for sodium cells using mixtures of ethylene carbonate and diethyl carbonate as the solvent of $NaPF_6$ electrolytes.

Journal of Power Sources 197 (2012) 314– 318

**corresponding author*

3.1.1 *Introduction*

Sodium-ion batteries have been envisaged as a promising alternative to lithium-ion cells as the current cost and accessibility of lithium may prevent the extensive use of lithium-based batteries. However, sodium electrodes have shown poor cycling properties and this would limit their applications. Almost two decades ago the concept of sodium-ion batteries as an alternative to lithium-ion batteries was discussed by Doeff et al.[1]. In this respect $NaCoO_2$ - the analogue of $LiCoO_2$ - was thoroughly studied as the positive electrode in sodium-ion cells using carbon [2,3] and conversion oxide materials [4] as anodes. Recently, Ellis et al.[5] reported on a sodium/lithium iron phosphate, A_2FePO_4F (A = Na, Li), that could serve as a cathode in either lithium-ion or -sodium-ion cells. The use of ionic liquids by Tarascon group has given interesting results on the ionothermal preparation of the sodium fluorophosphates, Na_2FePO_4F, cathode.[6]

The optimization of Na_2FePO_4F material for use in sodium test cells is the aim of this work. The study is focused in the changes affecting the cathode material with a common anode on changing the electrolyte. It is well known that safety problems led to discard the use of $LiClO_4$ in lithium-ion batteries. In this study, $NaPF_6$ was chosen instead of $NaClO_4$ in order to avoid safety problems associated to the use of perchlorates. The different organic solvents used in the study are common in lithium and sodium batteries. Firstly, we present a new preparation route based on mechanical activation and ceramic procedures. Then the effect of the electrolyte was analysed by X-ray absorption spectroscopy (XAS). The XAS study of the electrodes was done with different organic solvents. Finally, the choice of electrolyte

and potential window were assessed by the analysis of electrochemical results.

3.1.2 *Experimental*

The synthesis of Na_2FePO_4F was carried out in two steps. Firstly, a nano-$FePO_4$ precursor was synthesized by spontaneous precipitation from aqueous solutions as described by Huang et al.[7]. In a second step, the resultant $FePO_4$ was mixed with sodium carboxymethylcellulose (NaCMC, average Mw ~250,000) and NaF (99 % purity) in equimolar concentrations and with 10 ml of hot ethanol near the boiling point. The mixture was ground in a planetary ball-mill for 30 min at 500 rpm in air to get a solid-liquid rheological body, a kind of slurry. Finally, Fe^{3+} in the precursor compound ($FePO_4$) was reduced by calcination at 600ºC for 8h under argon atmosphere.

X-ray diffraction (XRD) patterns were recorded with a Siemens D-5000 apparatus provided with Cu K_α radiation and graphite monochromator. The 2θ scan rate was 0.04° per 1.2 s. Scanning electron microscopy (SEM) was performed in a JEOL-SM6300 microscope.

The electrochemical activity of Na_2FePO_4F/C powder toward Na was measured using Swagelok-type half cells. The test cells were assembled by stacking a sodium metal disk as the negative electrode, Whatman glass fibber disks supporting a 1 M $NaPF_6$ (EC:DEC) (1:1, w/w) or 1 M $NaPF_6$ (PC) electrolytes solution, and the Na_2FePO_4F/C as the positive electrode. The latter was prepared by pasting the electrode material onto an aluminium foil. For this purpose, a mixture of 75% of active material, 15% of carbon black, and 10% of PVDF binder was ball milled

for 30 min at 500 rpm in N-methylpyrrolidone (NMP) to form the paste. A VMP-3 multichannel system was used to cycle the cells at C/20 for the cycling between 4.2 and 1.5 V vs Na^+/Na.

^{57}Fe Mössbauer spectra were recorded in transmission mode (TMS) at room temperature, using an EG&G constant acceleration spectrometer and a ^{57}Co (Rh matrix) (10 mCi) γ radiation. The velocity scale was calibrated from the magnetic sextet of a high-purity iron foil absorber. Experimental data were fitted to Lorentzian lines by using a least-squares-based method. The quality of the fit was controlled by the classical χ2 test. All isomer shifts are given relative to the centre of the α-Fe spectrum at room temperature.

The X-ray absorption studies were performed on BM26 of the DUBBLE - Dutch-Belgian Beam Line - at the ESRF in Grenoble (France). The main characteristics of the beam line are: Incident energy range from 4.9 to 32 *keV*, flux of 1 × 1011 $photons.s^{-1}$, energy resolution dE/E of 2 10^{-4}, horizontal acceptance 2 *mrad*, beam size at sample place (H × V) max: 30 × 3 mm^2, min: 0 × 0.2 mm^2, and step-by-step data collection with the acquisition time of 1s for optimised sample. A 9-element monolithic Ge detector with a max. count rate per element ~150 kHz and an energy resolution < 250 *eV* at 5.9 *keV* for fluorescence measurements at low concentrations was used. An Fe foil was used to calibrate the energy at the edge (7112 *eV*). The analysis of the absorption data was performed using Sixpack software.[8]

3.1.3 *Results and discussion*

The X-ray diffraction (XRD) pattern of the resulting Na_2FePO_4F/C composite and the corresponding Rietveld refinement (Fig. 3.1.1) confirmed that the phosphate material can be indexed in the orthorhombic *Pbcn* space group in good agreement with previously reported data on Na_2FePO_4F.[5] However, by allowing the refinement of the Na site occupancy, a final stoichiometry of $Na_{1.8}FePO_4F$ with a = 5.2287_3 Å, b = 13.864_1 Å, and c =11.7615_8 Å. (R_{wp} = 14.9 %, R_{exp} = 14.9 %, R_{Bragg} = 8.6 %) was obtained. The origin of the lower sodium content as referred to stoichiometric Na_2FePO_4F will be further discussed below in the light of the spectroscopic results.

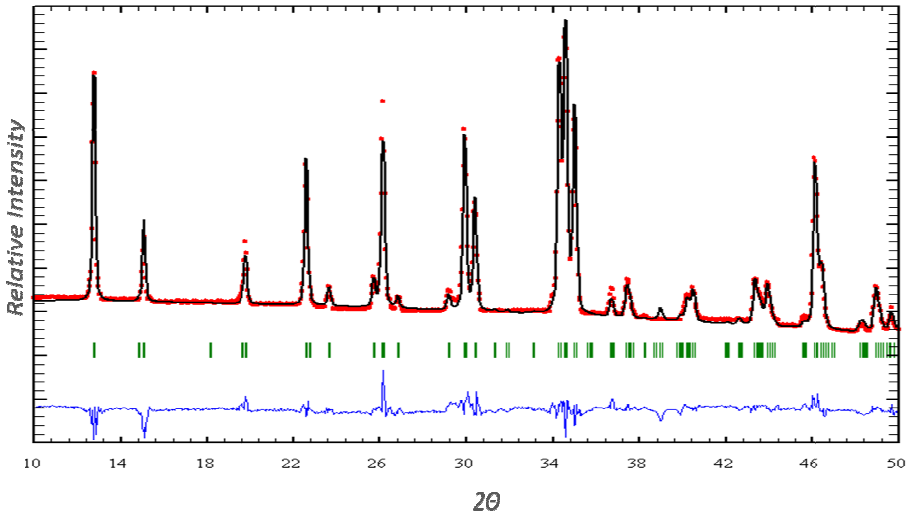

Figure. 3.1.1. XRD full-pattern fitting of the as-prepared Na_2FePO_4F/C composite

Thermogravimetric analysis was carried out in order to estimate the *in situ* carbon content. The TG curves (not shown) indicated one sharp mass-loss peak between 350 and 450ºC which corresponds to that of carbon removal (*m/m= 25.00 wt.%)*. This weigh loss process is related to an exothermic peak in the DTA curve at *ca.* 420ºC due to the release of carbon as volatile oxides. The SEM images showed agglomerates of

submicron primary particles (Fig. 3.1.2). The presence of Fe^{2+} was confirmed by ^{57}Fe Mössbauer spectroscopy.

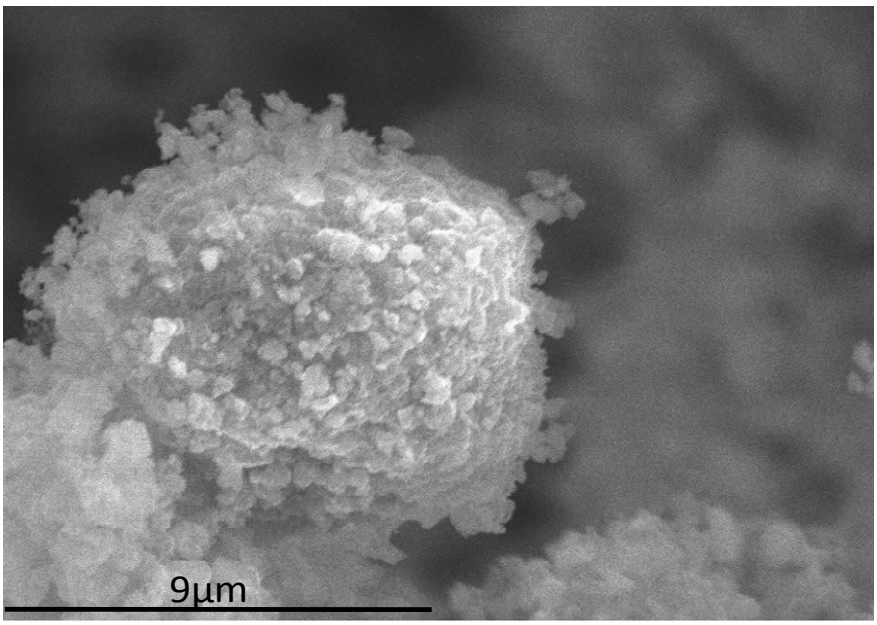

Figure. 3.1.2. SEM image of Na_2FePO_4F/C synthesized by solid-state reaction with hot ethanol.

Samples were galvanostatically cycled in Na/1M $NaPF_6$(PC)/Na_2FePO_4F/C and Na/1M$NaPF_6$(EC:DEC=1:1)/Na_2FePO_4F/C cells at C/20. As we can see in figure 3.1.3, Na/Na_2FePO_4F/C cells reversibly donate *ca.* one sodium at an average voltage of 3 *V* when cycling at C/20. Good electrochemical results were recorded, featuring capacity values between 100 and 120 $mAh.g^{-1}$. However, depending on the solvents electrolyte decomposition can be observed at end voltages. Using PC, the instability was observed at lower-end voltages while for EC:DEC at the higher-end values of the potential. The charge and discharge profiles and capacity fading were strongly dependent on the used electrolyte.

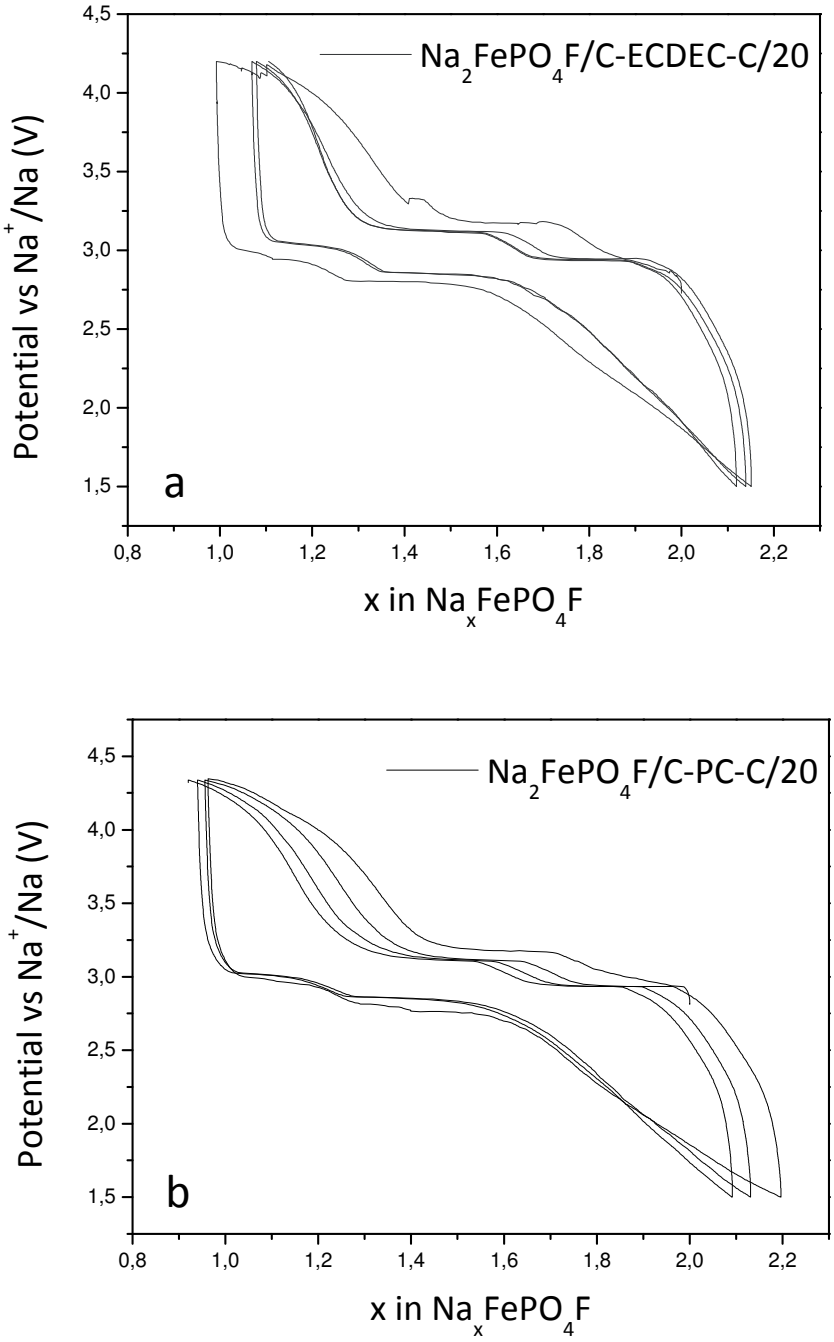

Figure 3.1.3. Charge/discharge galvanostatic curves at C/20 (1Na$^+$ in 20h) for Na/ Na_2FePO_4F/C cells using a) EC:DEC electrolyte cycled between 1.5 and 4.2*V* and b) PC electrolyte cycled between 1.5 and 4.3*V* vs Na$^+$/Na.

The electrochemical behaviour is presented in figure 3.1.4. As PC electrolyte showed instability at lower-end voltages, the upper limit was fixed at 4.2 *V*, while for lower potentials three different values were used (2.5*V*, 2.0*V* and 1.5*V*). In contrast, the EC:DEC electrolyte showed

instability at higher voltages so the lower potential was fixed at 1.5 V and three upper potentials were used (3.25 V, 3.75 V and 4.2 V), as shown in figure 3.1.4, upper. For both electrolytes a decrease in capacity can be observed when decreasing the voltage window. However, the cell stability depends on the electrolyte, and capacity decreases due to electrolyte decomposition at the end voltages. This is more pronounced for PC. The results revealed better capacity retention and higher values of capacity for the sodium cells using EC:DEC as the solvent of the electrolyte. Comparing the cycling performances at the same cell voltage window (4.2V-1.5V), it is evident that sodium cells using EC:DEC as an organic solvent, shows distinctly better electrochemical performance (Fig. 3.1.4, lower).

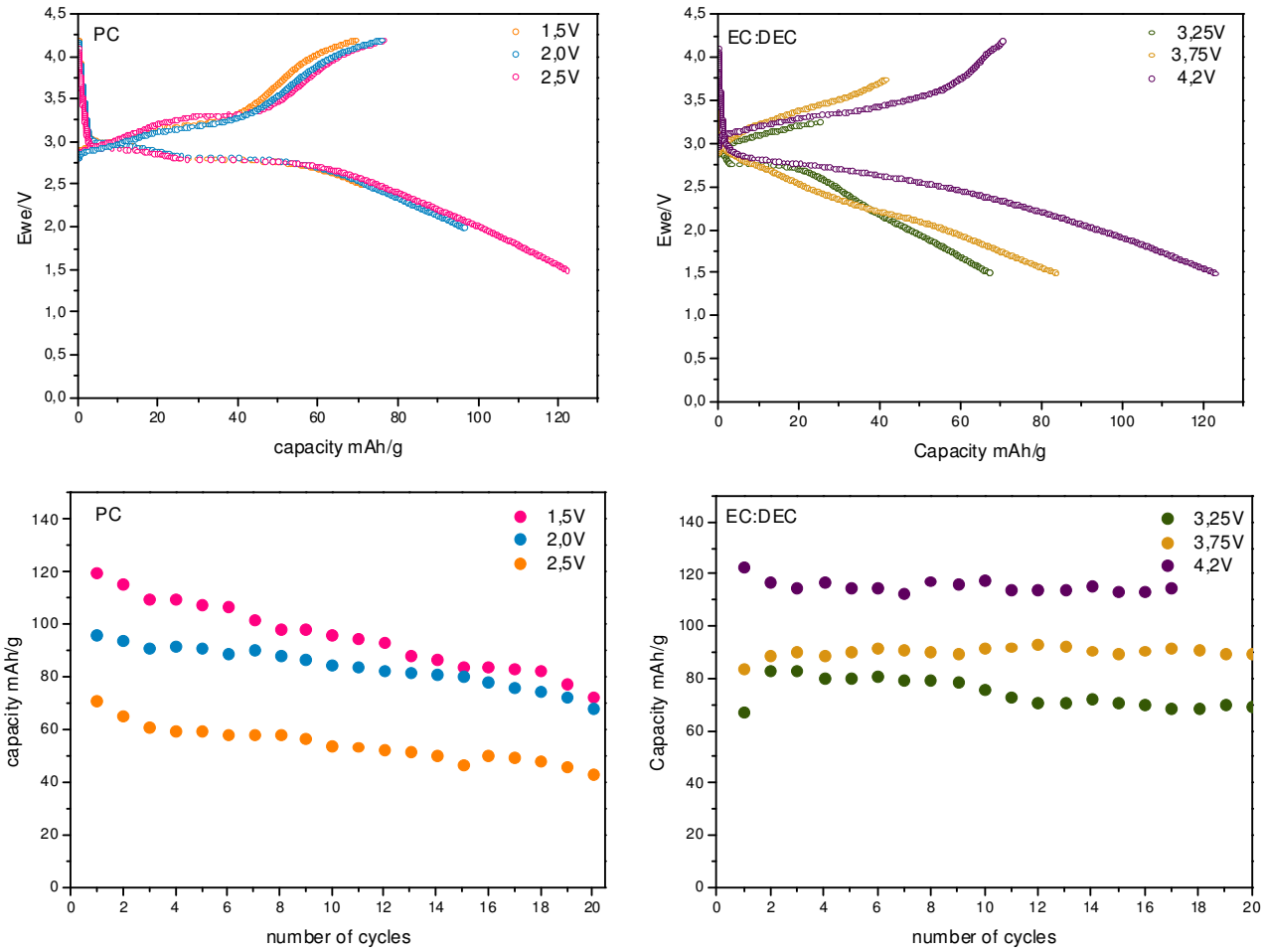

Figure 3.1.4. Upper: Charge/discharge galvanostatic profiles using PC electrolyte (left) and EC:DEC electrolyte (right) at different cut-off voltages. Lower: Capacity retention data for cycling at C/20 using PC electrolyte (left) and EC:DEC electrolyte (right) at different cut-off voltages.

The charge-discharge curves show an additional Na uptake. This can be understood from the Fe valency changes. Thus, the ^{57}Fe Mössbauer spectra shown in figure 3.1.5 and the corresponding fitting results (Table 3.1.I) indicates the presence of traces of Fe^{3+} in the original sample.

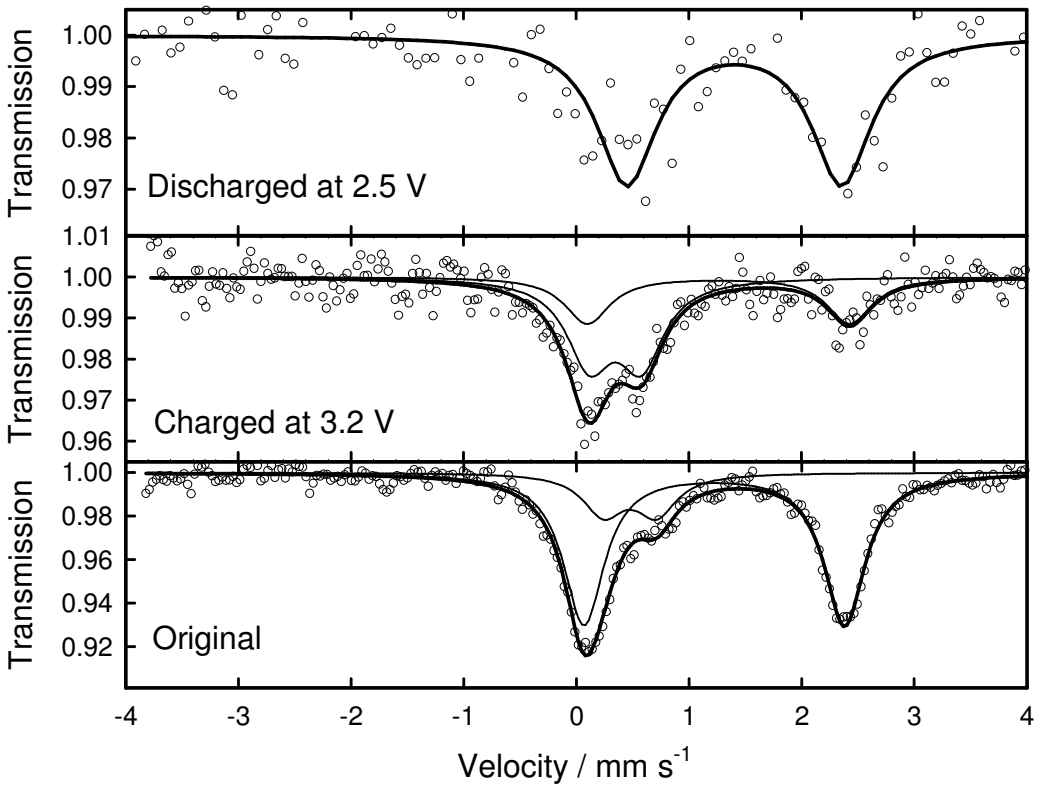

Figure 3.1.5. ^{57}Fe Mössbauer spectra of original and used electrodes at different voltages.

The presence of Fe^{3+} limits the charge capacity, while allowing a deeper reduction of iron after the first discharge. It is stressed that the intensity of the component peaks of the quadrupolar "doublet" of Fe^{2+} signals are typically the same. Therefore, fitting the curve of the sample discharged at 2.5 *V*, only Fe^{2+} was found, due to the intensity of the peak at ~2.4 $mm.s^{-1}$. The composition derived by Rietveld analysis is clearly correlated with the relative contributions of Fe^{2+} and Fe^{3+} in the Mössbauer spectra. The composition of the initial sample can be more strictly written as $Na_{1.8}Fe^{3+}{}_{0.2}Fe^{2+}{}_{0.8}PO_4$. The oxidation of Fe^{2+} is not complete on charge to 3.2 *V*, while the reduction to Fe^{2+} is virtually complete during the first discharge, as revealed by the single quadrupole split signal, reaching compositions closer to Na_2FePO_4. However, the deterioration of the quality of the spectra on cycling impeded the use of

this technique for further analysis. XAS was used as a successful alternative.

Table 3.1.I: Hyperfine parameters of fitted Mössbauer spectra of Na_2FePO_4F/C composite cycled electrodes.

	s/d	iron species	δ (mm/s)	Δ (mm/s)	Γ (mm/s)	C (%)	χ^2
Original	D	Fe(III)	0.48(2)	0.47(2)	0.44(5)	20.9	0.517
	D	Fe(II)	1.22(1)	2.31(1)	0.44(1)	79.1	
Charged at 3.2 V	D	Fe(III)	0.35(3)	0.46(6)	0.49(4)	63.6	0.524
	D	Fe(II)	1.26(6)	2.3 (1)	0.4(1)	36.4	
Discharged at 1.5 V	D	Fe(II)	1.40(4)	1.91 (6)	0.64(8)	100	0.512

s/d: singlet (*s*) or doublet (*d*); δ: isomeric shift; Δ: quadrupole splitting; Γ: line-width at half maximum; *C*: relative contribution; χ^2: goodness of the fitting.

A XANES study on electrodes at various state of charge was carried out here for the first time. The shift of the spectra to higher energies on charge agrees well with the oxidation of iron atoms from 2^+ to 3^+ (Fig. 3.1.6).

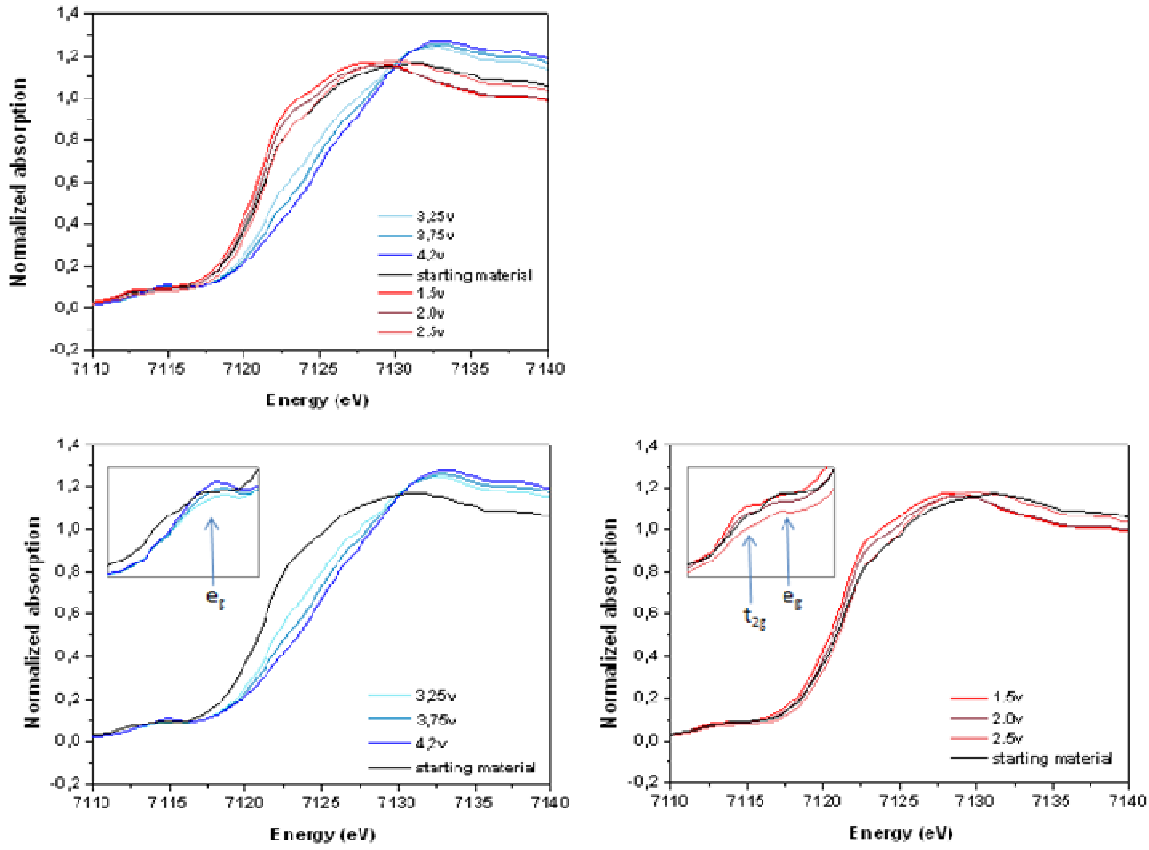

Figure 3.1.6. FeK XANES of Upper: pristine and used electrodes at different voltages. Lower right: details of original sample and charged electrodes. Lower left: Details of discharged electrodes

The reversibility of the process is clear as the capacity is almost completely recovered compared to the initial compound on discharge. The slight but significant shift toward lower energies, as referred to the original compound, after cell discharge agrees well with the extra capacity revealed by the above Mössbauer and electrochemical studies. Thus further sodium can be inserted with the simultaneous reduction of iron below the oxidation state in the original compound. In order to further understand the influence of the electrolyte on the efficiency of the electrochemical reaction with sodium, the spectra at different cut-off voltages were recorded in cells using both electrolytes. The larger differences of line shift with voltage during charging evidence the

important role of the electrolyte solvent stability at higher voltages. This behaviour makes it particularly important to use EC:DEC within a moderately high voltage window, as came out from the electrochemical results.

On the other hand, the intensity of the pre-edge in the spectra of figure 3.1.6 is indicative of the distortion of the coordination polyhedra, which allows p-d mixing.[9] In fact the cis-FeO_4F_2 units have symmetry lower than Oh. In addition, the t_{2g} and e_g contributions are visible, especially for the original sample, which is indicative of the high-spin configuration of Fe^{2+}. A similar behaviour was reported for the $FePO_4$/$LiFePO_4$ system, in which the Fe K-edge XANES studies revealed that iron in $LiFePO_4$ and $FePO_4$ are both in the expected high-spin state and exhibit a crystal field splitting of about 2 *eV*.[9-11] For Na_2FePO_4F, the crystal field splitting is slightly larger than 2 *eV*.

Furthermore, the intensity of the white line increases slightly on oxidation. This behaviour resembles $LiFePO_4$, in which the small changes in intensity were correlated with negligible changes in iron coordination.[10-11] If we assume a change in coordination for Fe that results in a more pronounced *p-d* mixing, which in turn could decrease the intensity of the white line, this should be accompanied by a sharp increase in the pre-edge intensity, as found in CoC_2O_4.[13] Moreover, the changes in unit cell parameters from orthorhombic Na_2FePO_4F to $NaFePO_4F$ reported by Ellis et al.[14] and the fact that the structural framework is maintained during cycling according to Trad et al.[15] could imply little distortions. Thus we can conclude that the decreased intensity of the white line is not indicative of abrupt changes in coordination.

3.1.4 *Conclusions*

A new preparation route is found to obtain Na_2FePO_4F/C composites. The resulting material contains the fluorophosphate in the known orthorhombic form, being ca. 10 % substoichimetric in sodium due to a partial reduction of iron. The composite electrode provides good cycling performance *vs.* sodium in test cells. The local structures of pristine Na_2FePO_4F, and charged and discharged electrodes have been examined by XANES. The results show that Fe^{2+} and Fe^{3+} are found in high spin configurations in discharged and charged electrodes, respectively. The crystal field splitting of Fe^{2+} obtained from the XANES pre-peak is ca. 2.3 *eV*. The structural changes from $Na_{1.8}FePO_4F$ to $NaFePO_4F$, and then to Na_2FePO_4F are small and initiating only slight changes in the intensity of the XANES white line. It is nevertheless stressed, that the choice of the electrolyte is crucial to improve the cycling performance. While the oxidation state is especially affected by the upper limit of the voltage, the discharge capacity is strongly affected when using PC as solvent. The capacity and capacity retention are higher for sodium cells using EC:DEC as solvent using $NaPF_6$ as salt.

Acknowledgement

This work was carried out in the MICINN MAT2008-05880 and Junta de Andalucía FQM-6017 contracts and ALISTORE-ERI.

References

1. Doeff M.M., Ma Y., Visco S. J., de Jonghe L. C., *J. Electrochem. Soc.* **1993**, 140, L169.

2. Alcántara R., Jiménez-Mateos J.M., Lavela P., Tirado J.L., *Electrochem. Commun.* **2001**, 3, 639.

3. Alcántara R., Jiménez-Mateos J. M., Tirado J. L., J. *Electrochem. Soc.* **2002**, 149, A201.

4. Alcántara R., Jaraba M., Lavela P., Tirado J. L., *Chem. Mater.* **2008**, 14, 2847.

5. Ellis B. L., Makahnouk W. R. M., Makimura Y., Toghill K., Nazar L. F., *Nature Mater.* **2007**, 5, 749.

6. Recham N., Chotard J-N., Dupont L., Djellab K., Armand M., Tarascon J.M., *J. Electrochem. Soc.* **2009**, 156, A993.

7. Huang Y., Ren H., Peng Z., Zhou Y., *Electrochim. Acta* **2009**, 55, 311.

8. Webb S. M., *Phys. Scr.* **2005**, 115, 1011.

9. Choi H. C., Lee S. Y., Kim S. B., Kim M. G., Lee M. K., Shin H. J., Lee J. S., *J. Phys. Chem. B* **2002**, 106, 9252.

10. Deb A., Bergmann U., Cairns E. J., Cramer S. P., *J. Synchrotron Rad.* **2004**, 11, 497.

11. Deb A., Bergmann U., Cairns E. J., Cramer S. P., *J. Phys. Chem. B*, **2004**, 108, 7046.

12. Deb A., Bergmann U., Cramer S. P., Cairns E. J., *Electrochim. Acta*, **2005**, 50, 5200.

13. Aragón M.J., León B., Pérez Vicente C., Tirado J.L., Chadwick A. V., Berko A., Beh S.Y., *Chem. Mater.* **2009**, 21, 1834.

14. Ellis B.L., Michael Makahnouk W.R., Rowan-Weetaluktuk W.N., Ryan D.H., Nazar L.F., *Chem. Mater.* **2010**, 22, 1059.

15. Trad K., Carlier D., Croguennec L., Wattiaux A., Lajmi B., Amara M.B., Delmas C., *Chem. Mater.* **2010**, 22, 5554.

3.2. Chromium substitution in ion exchanged $Li_3Fe_2(PO_4)_3$ and the effects on the electrochemical behaviour as cathodes for lithium batteries

Nareerat Plylahan, C. Vidal-Abarca, P. Lavela*, J.L. Tirado

Laboratorio de Química Inorgánica, Universidad de Córdoba. Edificio Marie Curie Campus de Rabanales 14071 Córdoba, Spain

Abstract

A new family of cathode materials for lithium cells with nominal stoichiometry $Li_3Fe_{2-x}Cr_x(PO_4)_3$ ($0 \leq x \leq 1$), was successfully prepared by ion exchange reactions of $Na_3Fe_{2-x}Cr_x(PO_4)_3$. The chemical exchange process leads to the structural transition from the monoclinic to a rhombohedral phase with an open framework which facilitates lithium diffusion. Chromium substitution was evidenced by a decrease in cell parameters in both sodium and lithium phases. ^{57}Fe Mössbauer spectra revealed a decrease in the isomer shift on increasing Cr content. The partial substitution by low Cr contents improved the electrochemical performance of $Li_3Fe_{2-x}Cr_x(PO_4)_3$. Thus, $Li_3Fe_{1.8}Cr_{0.2}(PO_4)$ reversibly inserted 1.7 Li ions per formula unit, delivering a specific capacity of 105 $mAh.g^{-1}$ after the first discharge. The low electrode impedance of Cr substituted compounds can be responsible for the improvement of the electrochemical behaviour.

Electrochimica Acta 62 (2012) 124–131

**corresponding author*

3.2.1 *Introduction*

Recently, NASICON-related compounds, $A_3M_2(XO_4)_3$ (A = Li, Na; M; Fe, Cr, Ti, V; X= P, As, S) have gained much attention as active cathode materials due to their superior properties: favorable redox properties, good ionic conductivity and low cost.[1-3] The NASICON structure consists of a three-dimensional framework built up by a framework of FeO_6 octahedra and XO_4 tetrahedra sharing all vertices.[4,5] Each FeO_6 octahedron is surrounded by six XO_4 tetrahedra and each tetrahedron is linked to four FeO_6 polyhedra, forming the $[Fe_2(XO_4)_3]^{3-}$ open framework.[6] Monoclinic $Na_3Fe_2(PO_4)_3$ and rhombohedral $Li_3Fe_2(PO_4)_3$ have two similar $[Fe_2(PO_4)_3]$ frameworks in the *ac*-plane. The different distribution of alkaline cations within the structure is responsible for the different crystal symmetries.[7]

Masquelier et al.[8] found that optimized electrodes based on the monoclinic $Li_3Fe_2(PO_4)_3$ phase cycle remarkably well in the 3.5–2.0 *V* potential range. The electrochemical performance of NASICON compounds can be enhanced by partial substitution of iron by other transition metals. For example, $Li_3Fe_{1.8}Ti_{0.1}Mn_{0.1}(PO_4)_3$ shows a specific capacity of 123.3 $mAh.g^{-1}$ for the first discharge at C/20 and 90.8 $mAh.g^{-1}$ for the 20th cycle at C/2, and shows better conductivity as compared with $Li_3Fe_2(PO_4)_3$.[9] Also, $Li_{1.6}Na_{0.4}TiFe(PO_4)_3$ shows lower specific capacity in the first discharge (110 $mAh.g^{-1}$) but excellent capacity retention □ 100 $mAh.g^{-1}$ over 50 cycles .[10]

Several cathode materials containing chromium have been proposed in the literature, such as chromium oxide (CrO_x),[11] Cr_8O_{21},[12] and $LiMn_xCr_{1-x}O_2$.[13] Nevertheless, the toxicity of chromium imposes the use of this

transition metal in low concentrations, *e.g* by using only partially substituted materials,[13] thin coating films [14] or doping.[15] Chromium substitution in positive electrodes such as $LiMn_2O_4$ has been previously reported.[16] Beneficial effects, including extra-capacity at high voltage [17] or suppression of the cooperative Jahn–Teller distortion [18] have been evidenced.

In this work, two new $Na_3Fe_{2-x}Cr_x(PO_4)_3$ and $Li_3Fe_{2-x}Cr_x(PO_4)_3$ ($0 \leq x \leq 1$) series have been synthesized by a low-cost, wet method for their use as cathode materials in lithium-ion batteries. The aim of the study is to evaluate the validity of a precipitation method to synthesize the $Na_3Fe_{2-x}Cr_x(PO_4)_3$ series and ion exchange to prepare the $Li_3Fe_{2-x}Cr_x(PO_4)_3$ series. The effects of chromium substitution on the local structure and electrochemical behavior in lithium test cell are examined.

3.2.2 *Experimental*

Known volumes of 0.4 M $Fe(NO_3)_3{\cdot}9H_2O$ and $Cr(NO_3)_3{\cdot}9H_2O$ solutions were mixed in a beaker according to the metal ratio in the solid product. Then, the stoichiometric amount of a 0.6 M $NaH_2PO_4{\cdot}H_2O$ solution was added dropwise into the beaker containing the transition metals. The mixture was vigorously stirred to obtain a clear dissolution and neutralized by adding concentrated ammonia. The resulting slurry was vigorously stirred to ensure a homogeneous pH in the whole volume. The solvent was evaporated on a hot plate under continuous stirring and finally dried into an oven at 80°C overnight. The precursors were ground and annealed at 600 °C under air atmosphere for 10 hours with a heating rate of $2°C.min^{-1}$.

$Li_3Fe_{2-x}Cr_x(PO_4)_3$ samples were prepared by ion exchange processes. For this purpose, $Na_3Fe_{2-x}Cr_x(PO_4)_3$ powders were added into a concentrated solution of $LiNO_3$ with $Li_{solution}/Na_{solid} > 10$ molar ratio. The slurry was continuously stirred at room temperature for 24 hours. The solid residua were centrifuged and washed with deionized water several times to remove $NaNO_3$ and excess of $LiNO_3$. The whole process was repeated three times to ensure a high efficiency.

The XRD patterns were recorded using a Siemens D5000 diffractometer in the 10-70°2θ range, with $\Delta(2\theta) = 0.040°$ step size, and 20 seconds step time. The Rietveld analyses were performed using the *Fullprof* software. ^{57}Fe Mossbauer spectroscopy studies were carried out at room temperature with an EG&G constant accelerator spectrometer in transmission mode. The source was ^{57}Co in a Rh matrix. The velocity scale was calibrated from the magnetic sextet of a high purity iron foil absorber. Experimental data were fitted to Lorentzian lines by using a least squares based method.[19] The quality of the fit was controlled by the usual χ^2 test. All the isomer shifts are given relative to the center of the α–Fe spectrum at room temperature. Transmission electron microscopy (TEM) images were recorded in a PHILIPS CM-10 microscope.

The electrode material was prepared by mixing the active materials, carbon black and PVDF (polyvinylidene fluoride) in a 75:15:10 ratio, respectively. A slurry was formed by adding N-methyl-2-pyrrolidone which was subsequently ball milled at 500 rpm for 30 minutes. The working electrode material was supported on a 9 mm aluminum plate and dried at 120°*C* under vacuum. Then, the electrodes were kept overnight in an argon atmosphere at 250°*C* in order to improve the

polymer characteristics. The cells were assembled inside an *MBraun* glove box under argon atmosphere. Swagelok type cells were used with lithium foil (diameter of 9 *mm*) as an auxiliary electrode. A solution of $LiPF_6$ in (EC:DEC) supported on glass fibber separator (GF/A-Whatman) was used as electrolyte. The lithium cells were galvanostatically cycled between 2 and 4.2 *V*. The charge and discharge rate was expressed as C/n, n being the number of hours needed for the reaction with 1 $F.mol^{-1}$ in n h at the applied current intensity. Values of C/10 and C/40 were used. Electrochemical impedance spectroscopy (EIS) was carried out in an Autolab PGSTAT12 system. For this purpose, the electrode was assembled in a three-electrode Swagelok type cell and was discharged to the lower cut off voltage by passing a constant current (C/10) between the working electrode and the counter electrode (Li). A quasi-equilibrium system was achieved by relaxing the cell for at least 12 h corresponding to a cell potential of 10 $mV.h^{-1}$. Eventually, the impedance spectra were recorded versus a Li reference electrode. An AC voltage signal of 5 *mV* was applied from 100 *KHz* to 2 *mHz*.

3.2.3 *Results and discussion*

The XRD patterns of $Na_3Fe_{2-x}Cr_x(PO_4)_3$ ($0 \leq x \leq 1$) are shown in figure 4.1.1. The patterns are characterized by narrow reflections corresponding to well-crystallized phases. Most of the reflections could be indexed to monoclinic $Na_3Fe_2(PO_4)_3$ with space group *C2c*. Several authors have identified, in both single-crystal [20] and powder samples,[21] a superstructure with a superlattice unit cell a = 15.128(1) Å, b = 8.721(1) Å, c = 21.564(1) Å, and β = 90.14(1)° in the space group *C2/c*. Several

peaks (e.g., in the 13º and 37º regions) reveal that superstructure is present in Cr-containing samples. Nevertheless, impurities are clearly evident by some weak peaks at ca. 17º and 32º in samples with x = 0.8 and 1.0 (marked with an asterisk in figure 3.2.1), which are ascribable to some of the most intense reflections of $Na_3Cr_3(PO_4)_4$ (JCDS-ICDD 35-0043).

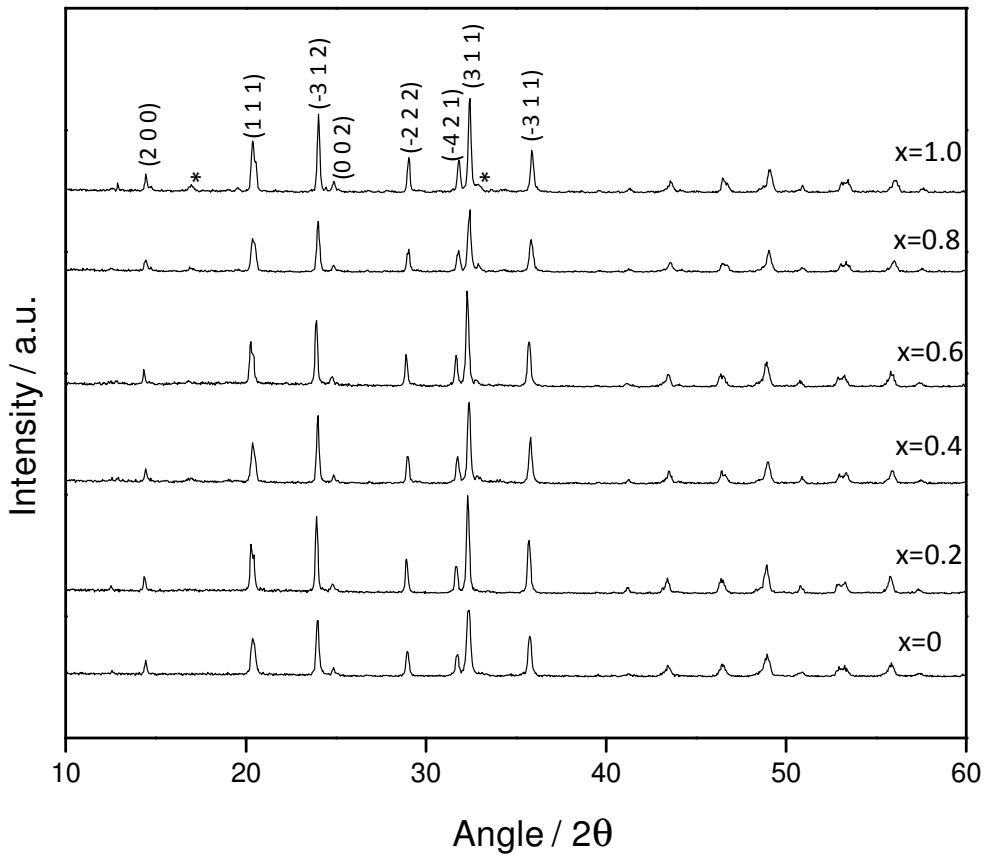

Figure 3.2.1. XRD patterns of $Na_3Fe_{2-x}Cr_x(PO_4)_3$; x = 0, 0.2, 0.4, 0.6, 0.8 and 1.0.

The precise quantification of impurities is difficult, due to the coexistence of the supperlattice, and the absence of data on the atomic coordinates in this superstructure, which prevent an accurate Rietveld analysis. A simplified analysis of the position of the peaks of the sublattice evidenced the effect of Cr substitution. Figure 3.2.2 shows a

decrease of the unit cell parameters on increasing chromium content that may be ascribed to the small difference in ionic radius between Fe^{3+} (0.645Å) and Cr^{3+} (0.615 Å).[21] The unambiguous presence of impurities at x = 1.0 can be responsible for the constancy of the c parameter after x=0.8, evidencing the solubility limit of chromium in the structure.

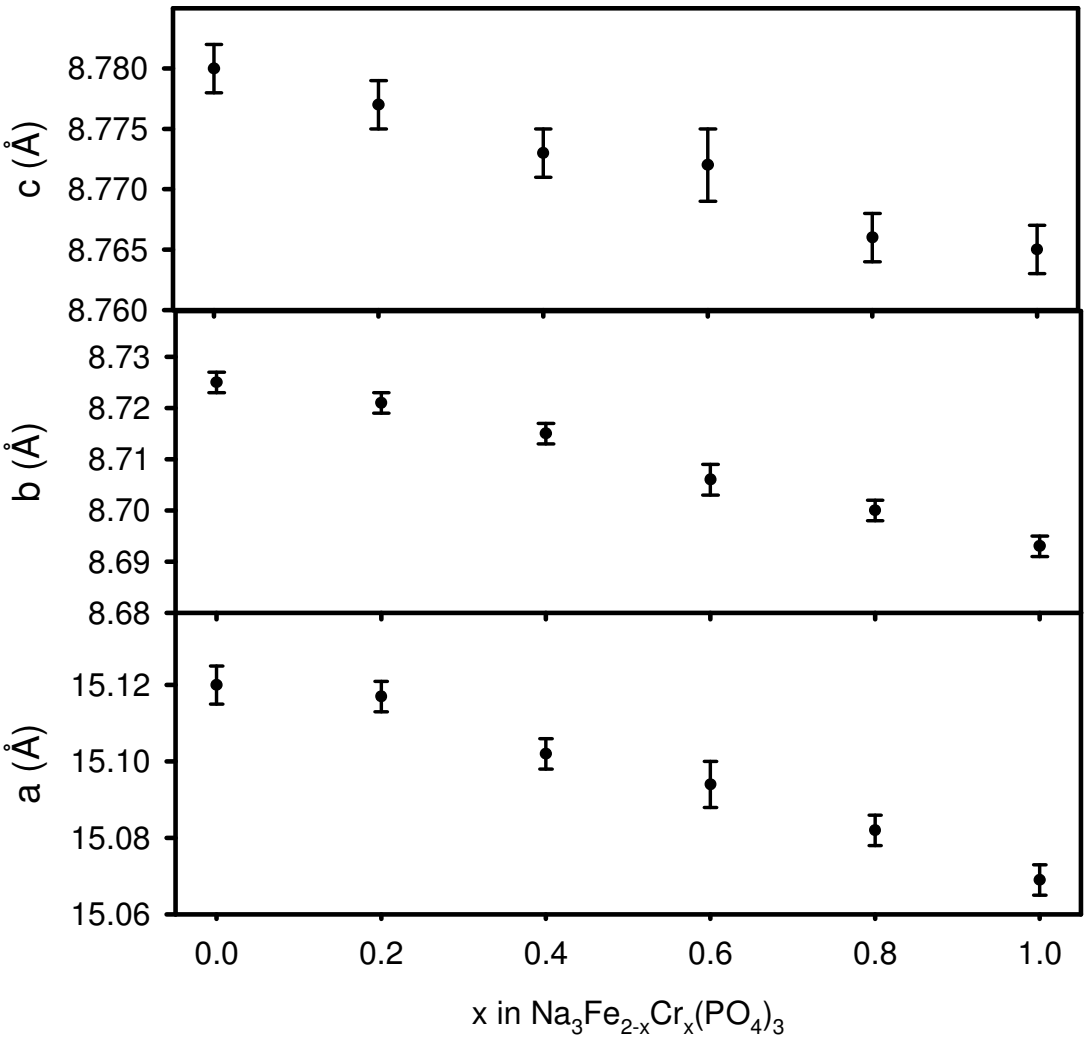

Figure 3.2.2. Cell parameters of $Na_3Fe_{2-x}Cr_x(PO_4)_3$ as a function of the chromium content.

Mössbauer *spectra* of $Na_3Fe_{2-x}Cr_x(PO_4)_3$ samples were recorded in order to obtain accurate information about the oxidation state and local environment of iron as probe atoms. The spectra are characterized by

one doublet signal with isomer shift value corresponding to the presence of Fe^{3+} ions, suggesting a unique site for iron atoms in the structure. The splitting of the signal is indicative of an anisotropic distribution of charges surrounding the probe atom. The introduction of Cr atoms does not involve significant changes in the spectrum profile (Fig. 3.2.3a). The hyperfine parameters of these spectra were calculated from their decomposition in lorentzian profiles. The results evidence a slight decrease of the isomer shift values as Cr content is increased (Fig. 3.2.3b).

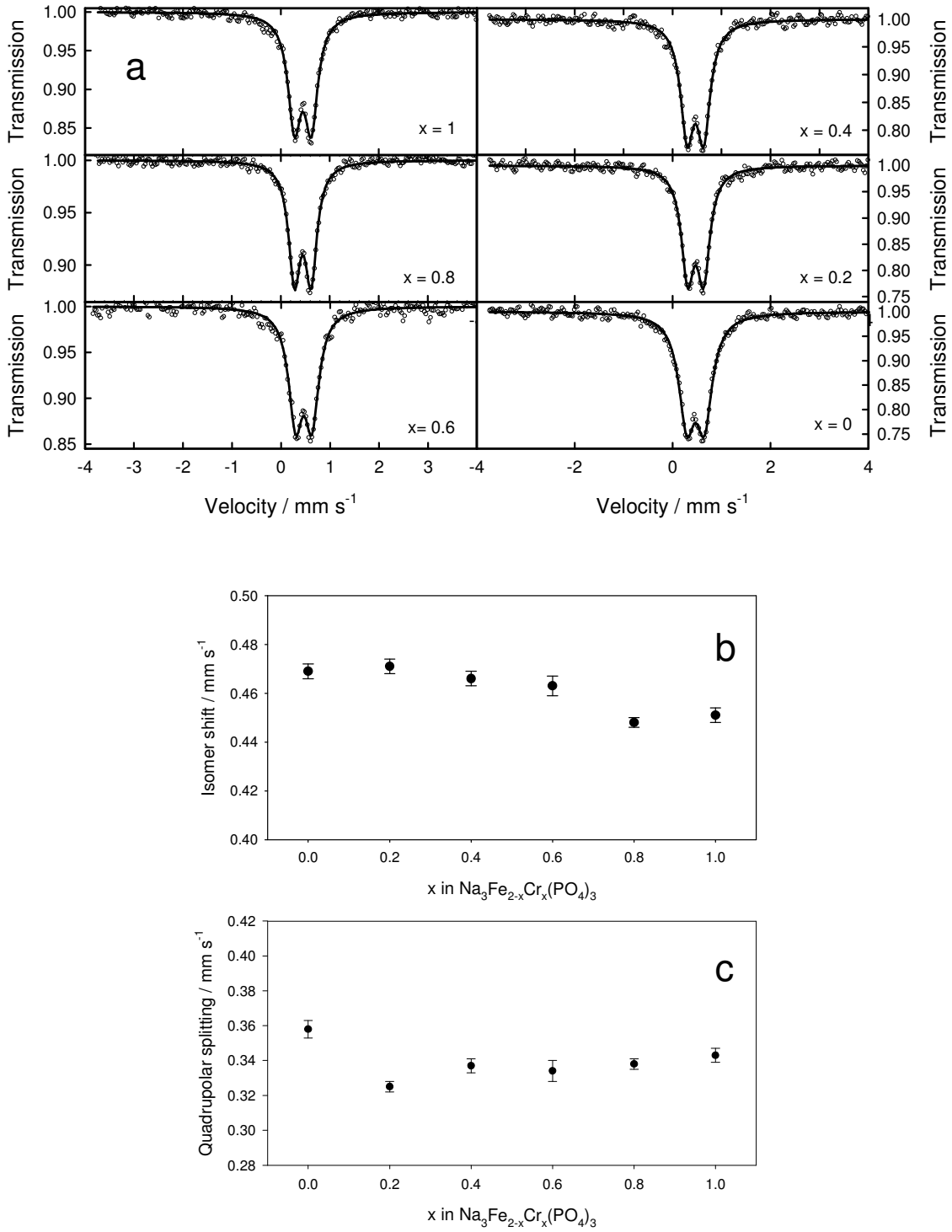

Figure 3.2.3. a) Mössbauer spectra of $Na_3Fe_{2-x}Cr_x(PO_4)_3$ series. Hyperfine parameters calculated from the fitted spectra: b) Isomer shift; c) Quadrupole splitting.

This effect can be interpreted in terms of the lower electronegativity of chromium as compared with iron. Thus, the introduction of chromium in the phosphate framework leads to an increase of electrons available for the neighbors Fe-O bonds. Consequently, the population of electrons surrounding the iron atoms would increase and, due to the negative sign of the ΔR/R ratio, a diminution of the isomer shift values is observed. Contrarily, a clear tendency could not be discerned from the analysis of the changes in quadrupole splitting vs. transition metal composition (Fig. 3.2.3c), which is probably indicative of a random distribution of iron and chromium atoms that averages the anisotropic distribution of charges surrounding the probe atom.

Lithium cells assembled with $Na_3Fe_{2-x}Cr_x(PO_4)_3$ samples were discharged and charged for several cycles (Fig. 3.2.4). During the electrochemical process Na^+ deinsertion and further Li^+ insertion from the electrolyte take place.[22] Discharge and charge curves are characterized by two insertion quasi-plateaus of similar extent. Masquelier et al. suggested a three phase system involving the existence of an intermediate composition.[23]

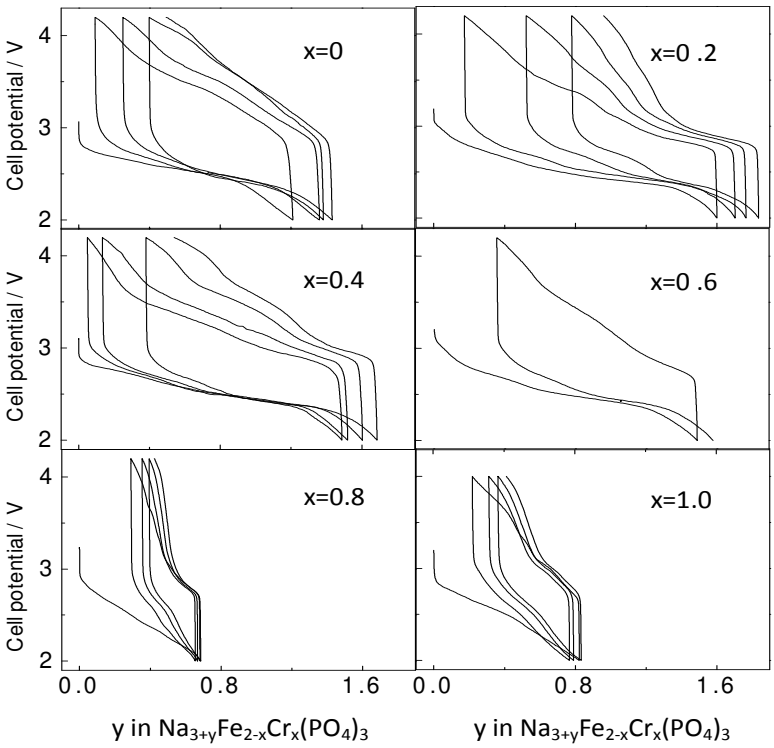

Figure 3.2.4. Galvanostatic plots for the of $Na_3Fe_{2-x}Cr_x(PO_4)_3$ series cycled at C/40.

This effect is preserved in chromium substituted solids. Also, it is clearly observed that the partial substitution of Fe by low Cr contents in $Na_3Fe_{1.8}Cr_{0.2}(PO_4)_3$ and $Na_3Fe_{1.6}Cr_{0.4}(PO_4)_3$ (Fig. 3.2.4b and c, respectively) decreases the polarization between charge and discharge branches as compared to $Na_3Fe_2(PO_4)_3$. Also, 1.6 and 1.5 Li could be inserted in the framework of $Na_3Fe_{1.8}Cr_{0.2}(PO_4)_3$ and $Na_3Fe_{1.6}Cr_{0.4}(PO_4)_3$ respectively during the first discharge. In contrast, only 1.25 Li^+ were inserted in $Na_3Fe_2(PO_4)_3$. Nevertheless, the electrochemical performance becomes poorer for samples with Cr contents higher than 0.6, as shown in figure 3.2.4d-f. These results agree fairly well with recent reports in which the beneficial effect of Cr doping in $LiFePO_4$ has been demonstrated.[24] Synchrotron-based in situ XRD analysis clearly showed that Cr doping facilitated the phase transformation during cycling and thus improved the rate performances of $LiFePO_4$/C. Also, some authors

have confirmed an enhancement of the electronic conductivity up to eight orders of magnitude from pure $LiFePO_4$ to $Li_{1-3x}Cr_xFePO_4$ with x = 0.01 and 0.03.[25] Contrarily, higher Cr contents do not lead to a further enhancement of the electrochemical performance. This result is not surprising and is the direct consequence of the electrochemical inactivity of chromium in the range of potentials here studied. Among the various Cr substituted samples, $Na_3Fe_{1.8}Cr_{0.2}(PO_4)_3$ offers the highest specific capacity for the first discharge of 88.3 $mAh.g^{-1}$. However, these cathode materials exhibit reduced specific capacity and rapid capacity fading, most probably as a consequence of the large Na^+ size as compared to Li^+, leading to a poor ionic diffusion.

The crystal structure of monoclinic $Na_3Fe_{2-x}Cr_x(PO_4)_3$ consists of a 3-D framework in which FeO_6 octahedra and PO_4 tetrahedra are connected to each other through all their vertices. In the real NASICON structure, the arrangement of MO_6 and XO_4 polyhedra results in an open structure which allows fast alkali-ion diffusion through the bottlenecks defined by eight-member rings.[23] In order to enhance the electrochemical behavior of these compounds, ion exchange reactions were used to replace the alkaline ions. The efficiency of the ion exchange process was checked by Energy Dispersive Spectroscopy (EDS). The analysis clearly shows the effective reduction of the sodium content. It leads to a $Li_3Fe_{2-x}Cr_x(PO_4)_3$ nominal stoichiometry. The EDS results are shown as Na/P ratios in Table 3.2.I.

Table 3.2.I. Atomic ratios of the $Na_3Fe_{2-x}Cr_x(PO_4)_3$ and $Li_3Fe_{2-x}Cr_x(PO_4)_3$ series.

X	Elements (ratio)	Theoretical atomic ratio of $Na_3Fe_{2-x}Cr_x(PO_4)_3$	Observed ratio	
			$Na_3Fe_{2-x}Cr_x(PO_4)_3$	$Li_3Fe_{2-x}Cr_x(PO_4)_3$
0	Na/P	1	1.16	0.11
0.2	Na/P	1	1.14	0.10
0.4	Na/P	1	0.80	0.16
0.6	Na/P	1	0.78	0.07
0.8	Na/P	1	0.99	0.07
1.0	Na/P	1	1.27	0.04

The XRD patterns of the $Li_3Fe_{2-x}Cr_x(PO_4)_3$ samples prepared by ion exchange of $Na_3Fe_{2-x}Cr_x(PO_4)_3$ are shown in figure 4.1.5. The peaks observed in the patterns can be indexed as rhombohedral $Li_3Fe_2(PO_4)_3$ with space group $R\bar{3}$.[26] Again, the peaks located around 17° and particularly, at 32° 2θ correspond to $Na_3Cr_3(PO_4)_4$ impurities. In addition, the low atomic scattering of lithium prevents the detailed Rietveld refinement of the patterns. However, the presence of impurities is unambiguous for x = 0.8 and 1.0, which may indicate the solubility limit of chromium in the structure. However, it should be noted that impurities may result from microinhomogeneities during the preparation of the samples, and thus their presence may not be directly related with solubility limits.

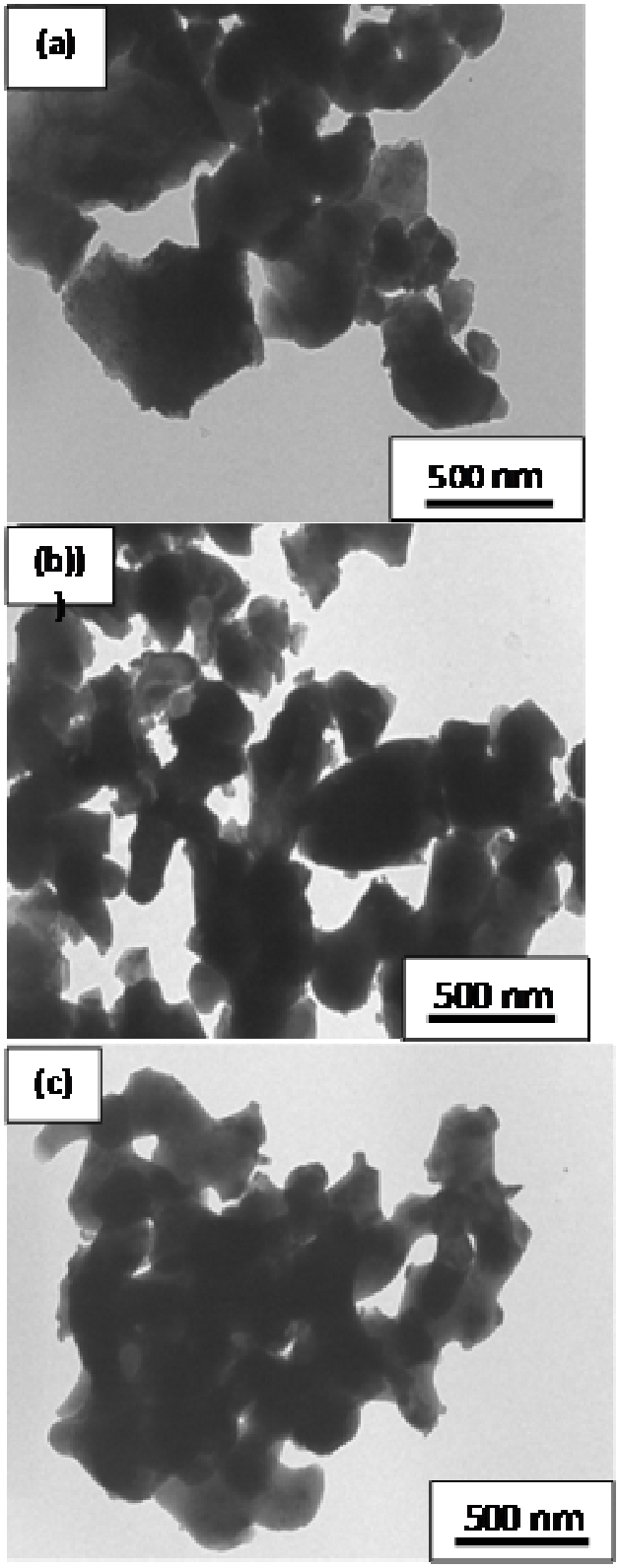

Figure 3.2.5. TEM images of (a) $Na_3Fe_2(PO_4)_3$, (b) $Na_3Fe_{1.8}Cr_{0.2}(PO_4)_3$ and (c) $Li_3Fe_{1.8}Cr_{0.2}(PO_4)_3$

A continuous decrease in the unit cell parameters was observed on increasing chromium content, except for the sample with x=1 (Table 3.2.II). These results agree with those of $Na_3Fe_{2-x}Cr_x(PO_4)_3$ where the partial substitution of Fe by Cr does not change the crystal structure and has a reduced effect on the lattice dimensions.

Table 4.1.II. Unit cell parameters of $Li_3Fe_{2-x}Cr_x(PO_4)_3$ series.

x in $Li_3Fe_{2-x}Cr_x(PO_4)_3$	a (Å)	b (Å)
0	8.3236(8)	22.512(2)
0.2	8.3163(6)	22.495(2)
0.4	8.3147(7)	22.488(2)
0.6	8.3027(6)	22.443(2)
0.8	8.2994(7)	22.397(2)
1	8.3045(5)	22.432(2)

Figure 3.2.6 shows TEM images of $Na_3Fe_2(PO_4)_3$, $Na_3Fe_{1.8}Cr_{0.2}(PO_4)_3$ and $Li_3Fe_{1.8}Cr_{0.2}(PO_4)_3$. A large inhomogeneity is observed in both particle size and shape. For $Na_3Fe_2(PO_4)_3$ and $Na_3Fe_{1.8}Cr_{0.2}(PO_4)_3$ samples, particle sizes were in the 125-750 nm and 200-850 nm ranges, respectively, in agreement with Figure 3.2.6a and b. For the $Li_3Fe_{1.8}Cr_{0.2}(PO_4)_3$ sample (Fig. 3.2.6c), it can be seen that the edges of the particles are more rounded as compared to $Na_3Fe_{1.8}Cr_{0.2}(PO_4)_3$. Most probably, the continuous stirring during the ion exchange process polished the sharp edges of the particles. The Mössbauer spectra of ion exchanged samples are characterized by a low splitting signal (Fig. 3.2.7a). This profile is similar to that obtained by Thomas et al. on rombohedral $Li_3Fe_2(PO_4)_3$.[7] The isomer shifts reveal that the oxidation state of iron remains unchanged upon the chemical exchange of the alkaline ions. However, metal substitution has a significant effect on

isomer shift. The observed decrease on increasing Cr content (Fig. 3.2.7b) may be interpreted in terms of the different electronegativity of chromium and iron.

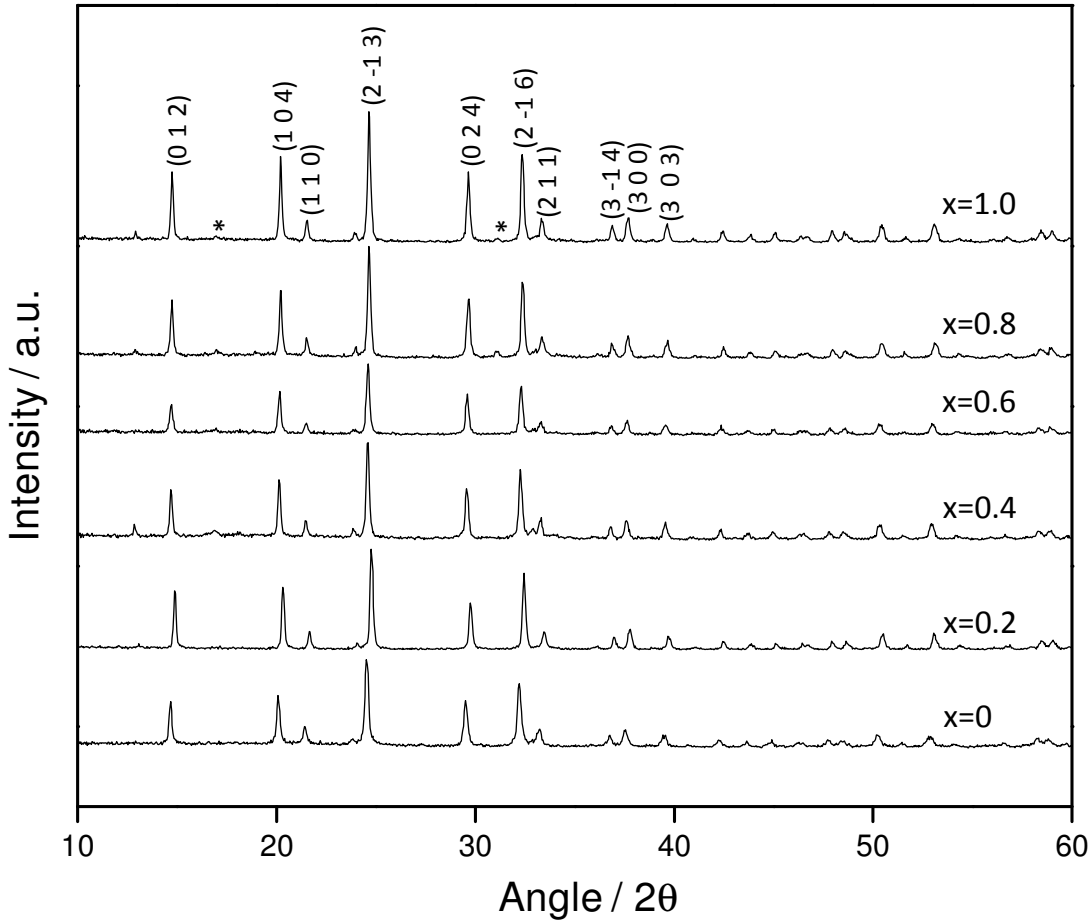

Figure 3.2.6. XRD patterns of $Li_3Fe_{2-x}Cr_x(PO_4)_3$; x = 0, 0.2, 0.4, 0.6, 0.8 and 1.0.

On the other hand, the effective reduction of the quadrupolar splitting on increasing Cr content (Fig. 3.2.7c) is a direct proof of the transition from the monoclinic system to the more symmetric rhombohedral system. Thus, the presence of chromium leads to a more isotropic distribution of charges around the probe atom.

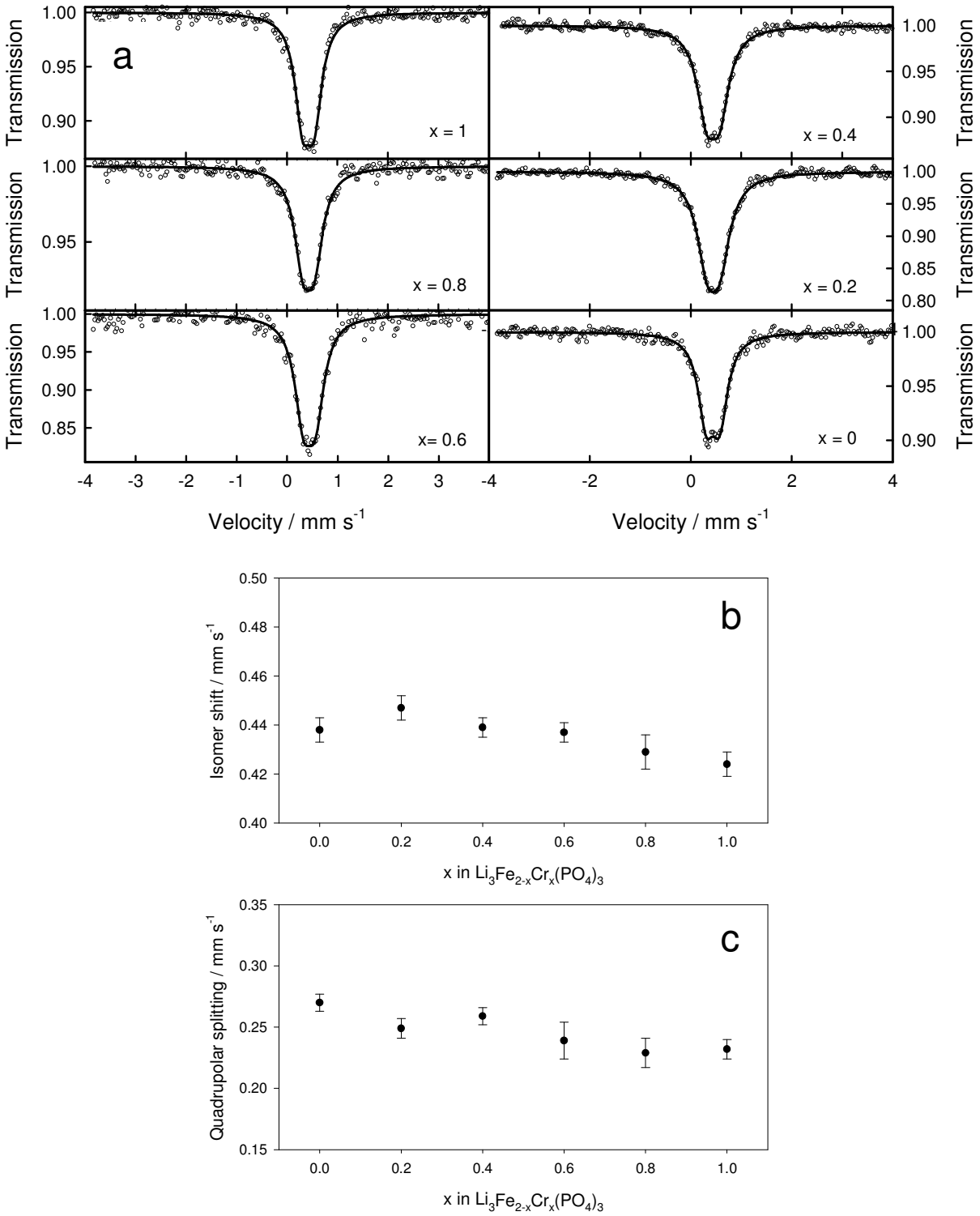

Figure 3.2.7. Mössbauer spectra of $Li_3Fe_{2-x}Cr_x(PO_4)_3$ series. Hyperfine parameters calculated from the fitted spectra: b) Isomer shift; c) Quadrupole splitting.

From figure 3.2.8, it is clear that the electrochemical performance of the different $Li_3Fe_{2-x}Cr_x(PO_4)_3$ samples improves significantly as compared to

the $Na_3Fe_{2-x}Cr_x(PO_4)_3$ series. Also, the polarization between charge and discharge profiles decreased, and a higher Li content is inserted upon discharge. This improvement can be ascribed to the more open framework of rhombohedral $Li_3Fe_2(PO_4)_3$ which results in the ease of Li insertion/extraction into/from the structure. Previous reports have shown that the insertion reaction proceeds as in a solid solution.[25]

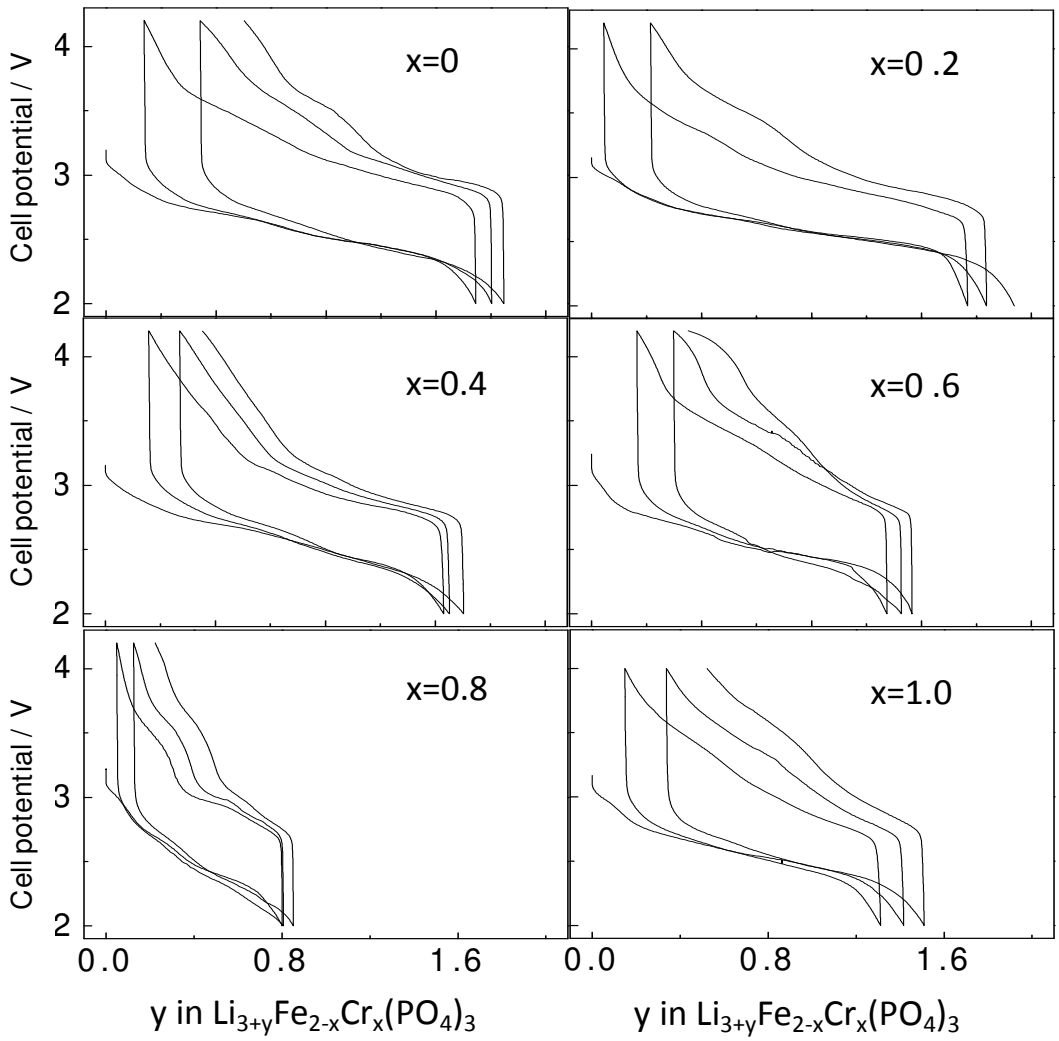

Figure 3.2.8. Galvanostatic plots for the series of $Li_3Fe_{2-x}Cr_x(PO_4)_3$ at C/40.

Among the different Cr-substituted samples, $Li_3Fe_{1.8}Cr_{0.2}(PO_4)_3$ shows the best efficiency, as evidenced in Figure 8b. Up to 1.7 Li per formula unit are inserted with a specific capacity of 105 $mAh.g^{-1}$ for the first

discharge. These results confirm the beneficial effect of Cr substitution on the electrochemical behavior and agree with the results obtained for $Na_3Fe_{2-x}Cr_x(PO_4)_3$. Thus, the sample with 0.2 Cr per formula unit is able to significantly enhance the insertion capacity as compared to the non substituted sample. In addition, the cycling efficiency was evaluated after the first discharge for selected samples. Thus, a 75.7 % of reversibility was calculated for the chromium free sample, while 96.7 % of the capacity of the first cycle was recovered for $Li_3Fe_{1.8}Cr_{0.2}(PO_4)_3$. Nevertheless, larger Cr contents did not involve further improvements of the electrochemical behavior. The rate capability of cathode materials with Cr ≤ 0.4 was also tested at a charge/discharge rate of C/10 (Fig. 3.2.9). It can be seen from the figure that the specific capacity of the first discharge drops as increasing in kinetic rates for all materials. However, $Li_3Fe_{1.8}Cr_{0.2}(PO_4)_3$ has the capability to maintain the discharge capacity at 97% after the first discharge when the rate is increased, as shown in figure 3.2.9b. For $Li_3Fe_2(PO_4)_3$ and $Li_3Fe_{1.6}Cr_{0.4}(PO_4)_3$, the capacity at the first discharge drops 18% and 14%, respectively, when the rates increase from C/40 to C/10.

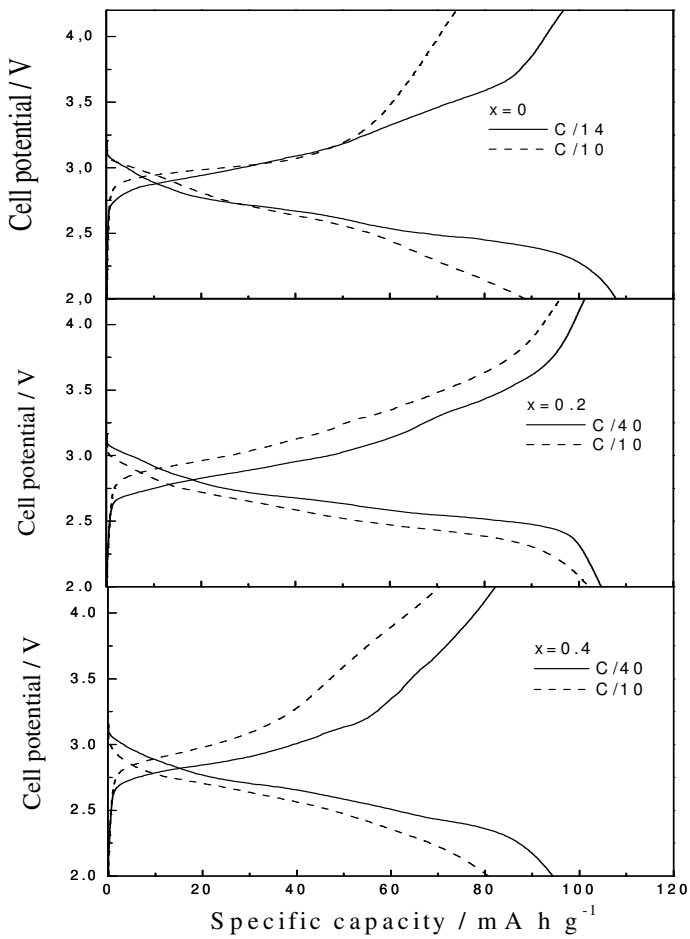

Figure 4.1.9. Discharge profiles at the kinetic rates of C/10 and C/40 (a) $Li_3Fe_2(PO_4)_3$, (b) $Li_3Fe_{1.8}Cr_{0.2}(PO_4)_3$ and (c) $Li_3Fe_{1.6}Cr_{0.4}(PO_4)_3$.

The different kinetic response of samples with a dissimilar level of substitution may also explain the divergences in the observed electrochemical performance. Figure 3.2.10 displays the Nyquist plots obtained for selected compositions. The spectra were recorded on pristine materials before lithium reaction, and after the first discharge for selected samples. The spectra were recorded at the end of the first discharge. The semicircle observed at medium frequencies is attributed to the charge transfer occurring when lithium migrates through the electrode/electrolyte interphase. The depression of the semicircles reveals a deviation from the ideal capacitor expressed in terms of a constant-phase element (CPE). The straight line at low frequencies

relates to the Warburg impedance which interpreted in terms of the lithium diffusion into the particles.[27,28] A semicircle at high frequencies, ascribable to the lithium migration through a passivating film, was not observed in these samples. Franger et al. have correlated the presence of this second semicircle to the use of propylene carbonate (PC) as a solvent component in the electrolyte composition, whose degradation product the formation of the polymer film. The absence of this organic solvent in our cells would justify the observed profile.[29]

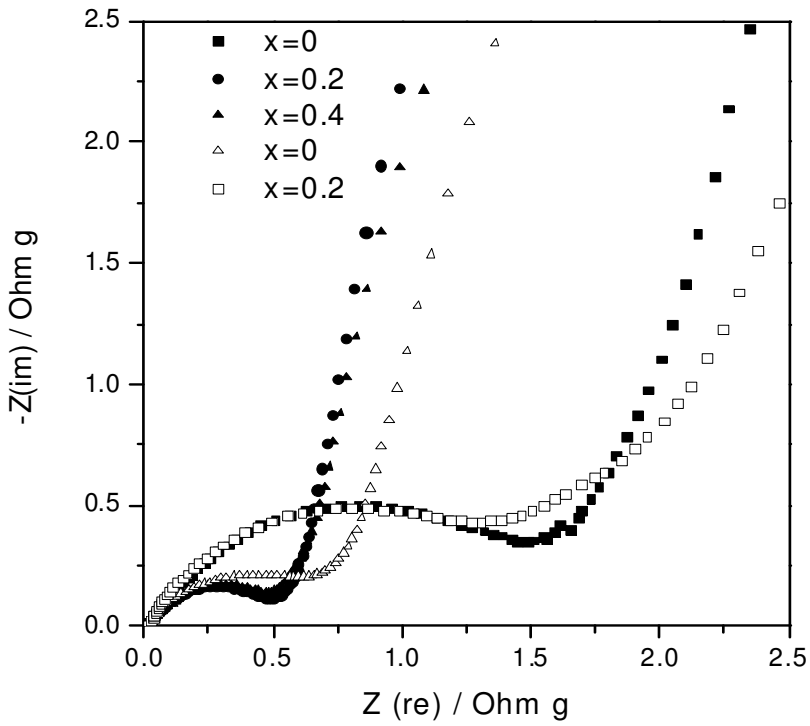

Figure 3.2.10. Impedance spectra of pristine $Li_3Fe_{2-x}Cr_x(PO_4)_3$ (x = 0, 0.2) (open symbols) and $Li_3Fe_{2-x}Cr_x(PO_4)_3$ (x = 0, 0.2, 0.4) electrodes after the first discharge at C/10 (closed symbols).

These plots evidence that the substitution of iron by chromium leads to a notorious decrease in the electrode impedance. It may justify the improvement in the electrochemical performance of Cr substituted

compounds, in spite of the lack of electroactivity of this transition metal.

4.1.4 *Conclusions*

A $Na_3Fe_{2-x}Cr_x(PO_4)_3$ ($0 \leq x \leq 1$) series was prepared by a single precipitation method and further annealing at 600 ºC. The XRD studies reveal that monoclinic phases are obtained with a slightly decrease in the unit cell parameters as increasing the Cr content. Mössbauer spectroscopy evidences the presence of Fe^{3+} ions which isomer shift values slightly decreased as the Cr content increased. This effect has been correlated to changes in the bond covalence due to the less electronegative character of chromium atoms. The electrochemical behavior of monoclinic $Na_3Fe_{2-x}Cr_x(PO_4)_3$ versus lithium showed that partial chromium substitution ($x \leq 0.4$) involves an increase in capacity and a decrease in polarization between charge and discharge branches. Nevertheless, the electrochemical performance becomes poorer for samples with Cr contents higher than 0.4. In order to improve this behavior, the samples were subjected to an ion exchange process in order to modify their compositional and structural properties.

A rhombohedral $Li_3Fe_{2-x}Cr_x(PO_4)_3$ series, where ($0 \leq x \leq 1$), were successfully prepared by ion exchange reaction of $Na_3Fe_{2-x}Cr_x(PO_4)_3$. Mössbauer studies revealed that the oxidation state of iron remains unchanged upon the chemical exchange of the alkaline ions. The electrochemical studies versus Li evidenced that the partial substitution of low Cr contents improved the electrochemical performance of $Li_3Fe_2(PO_4)_3$. The most promising performances corresponded to the

sample nominally containing 0.2 Cr per formula unit. For this sample, 1.7 Li ions per formula unit are inserted delivering a specific capacity of 105 $mAh.g^{-1}$ after the first discharge. The remarkable decrease in electrode impedance for Cr substituted samples may counterbalace the non-electroactivity of chromium, at least for low contents.

Acknowledgements

The authors are grateful to MICINN (MAT2008-05880) and Junta de Andalucía for financial support (Contract FQM-6017) We thank to SCAI (UCO Central Service for Research Support) and C. Vidal-Abarca is indebted to MCYT for his predoctoral grant.

References

1. Delmas C., Nadiri A., Soubeyroux J.L., *Solid State Ionics* 1988, 28-30 419.
2. Saidi M.Y., Barker J., Huang H., Swoyer J.L., Adamson G., *Electrochem. Solid State Lett.* **2002**, 5 , A149.
3. Yin S.C., Strobel P.S., Grondey H., Nazar L.F., *Chem. Mater.* **2004**, 16 1456.
4. Catti M., Comotti A., Blas S.D., Ibberson R.M., *J. Mater. Chem.* **2004**, 14, 835.
5. Anantharamulu N., Koteswara K., Rambabu R. G., Kumar B. V., Radha V., Vithal M., *J. Mater. Sci.* **2011**, 46, 2821.
6. Goñi A., Mesa J.L., Pizarro J.L., Fournés L., Wattiaux A., Olazcuaga R., Arriortua M.I., Rojo T., *J. Solid State Chem.* **2006**, 179, 81.
7. Andersson A.S., Kalska B., Eyob P., Aernout D., Häggström L., Thomas J.O., *Solid State Ionics* **2001**, 140, 63.
8. Patoux S., Wurm C., Morcrette M., Rousse G., Masquelier C., *J. Power Sources.* **2003,** 119-121, 278.
9. Sun J.K., Huang F.Q., Wang Y.M., Shan Z.C., Liu Z.Q., Liu M.L., Xia Y.J., Li K.Q., *J. Alloys Compd.* **2009,** 469, 327.
10. Patoux S., Rousse G., Leriche J.B., Masquelier C., *Chem. Mater.* **2003, 1**5, 2084.
11. Ramaraja P., Ramasamy, Ramadass P., Haran B. S., Popov B. N., *J. Power Sources.* **2003,** 124, 155.
12. Liu J., Wang Z., Li H., Huang X., Solid State Ionics **2006,** 177, 2675.

13. Myung S. T., Komaba S., Hirosaki N., Kumagai N., Arai K., Kodama R., Terada Y., Nakai I., *J. Power Sources* **2003,** 119–121, 211.
14. Şahan H., Göktepe H., Patat Ş., Ülgen A., *Solid State Ionics* **2010,** 181, 1437.
15. Arunkumar T.A., Manthiram A., *Electrochim. Acta.* **2005,** 50, 5568.
16. Pascual L., Gadjov H., Kovacheva D., Petrov K., Herrero P., Amarilla J. M.,. Rojas R. M, Rojo J. M., *J. Electrochem. Soc.* **2005,** 152, A301.
17. Sigala C., Guyomard D., Verbaere A., Piffard Y., Tournoux M., *Solid State lonic*s **1995,** 81, 167.
18. H. Ikuta, K. Takanaka, M. Wakihara, *Thermochim. Acta.* **2004,** 414, 227.
19. W. Kündig, *Nucl. Instr. Methods.* **1969,** 75, 336.
20. F. d'Yvoire, M. Pintard Screpel, E. Bretey and M. de la Ròchere, *Solid State Ionics* **1983,** 9/10, 851.
21. C. Masquelier, C. Wurm, J. Rodriguez-Carvajal, J. Gaubicher, L. Nazar, *Chem. Mater.* **2000,** 12, 525.
22. Ellis B., Makahnouk W. R. M., Makimura Y., Toghill K., Nazar L. F., *Nat. Mater.* **2007,** 6, 749.
23. Masquelier C., Padhi A. K., Nanjundaswamy K. S., Goodenough J. B., *J. Solid State Chem.* **1998,** 135, 228.
24. Shin H. C., Park S. B., Jang H., Chung K. Y., Cho W. I., Kim C. S., Cho B. W., *Electrochim. Acta* **2008,** 53, 7946.
25. Shi S., Liu L., Ouyang C., Wang D. S., Wang Z., Chen L., Huang X., *Phys. Rev. B: Condens. Matter Mater. Phys.* **2003,** 68, 195108/1.

26. Ait Salah A., Jozwiak P., Zaghib K., Garbarczyk J., Gendron F., Mauger A., Julien C.M., *Spectrochim. Acta, Part A* **2006,** 65, 1007.
27. Li X., Yang R., Cheng B., Hao Q., Xu H., Yang J., Qian Y., *Mater. Lett.* **2012,** 66, 168-171.
28. Jorcin J.-B., Orazem M. E., Pebere N., Tribollet B., *Electrochim. Acta* **2006,** 51, 1473.
29. Franger S., Bach S., Farcy J., Pereira-Ramos J.-P., Baffier N., *Electrochim. Acta.* **2003,** 48, 891.

Capítulo 4

Resumen y Conclusiones

5.1 Resumen

Dentro de los ánodos de conversión sintetizados, se han estudiado con detalle las espinelas $CoFe_2O_4$ y $NiFe_2O_4$. El compuesto de cobalto ha sido sintetizado mediante el método de micelas inversas basado en el uso de surfactantes aniónicos orgánicos que estabilizan *water-in-oil* micelas que actúan como pequeños reactores. Se han obtenido diversas muestras del material modificando variables como la concentración de los reactivos de partida (6M o 8M de NaOH), diferentes temperaturas de calcinación (800ºC ó 1000ºC), distintos surfactantes (Span80 o Tween85) a varios ratios de fase orgánica:fase acuosa (1:1 o 1:2).

La difracción de rayos X de las muestran presentaron un conjunto de reflexiones intensas que han sido ajustadas en el grupo espacial *Fd3m* y un buen nivel de pureza. La microscopía SEM reveló aglomerados de partículas submicrométricas para todos los casos. Independientemente de la relación fase orgánica:fase acuosa las muestras que se sintetizaron usando Span80 presentaban menor tamaño de partículas primarias que las muestras sintetizadas con Twenn85. El tamaño aumentaba cuanto mayor era la temperatura de calcinación

Como se desprende de lo expuesto durante la memoria, uno de los aspectos a optimizar dentro de los electrodos de conversión se trata de la pérdida de capacidad durante el ciclado. La técnica Mössbauer ha constituido una herramienta fundamental para la comprensión de los procesos involucrados en el ciclado galvanostático de las muestras estudiadas. La espectroscopía Mössbauer se ha llevado a cabo en muestras originales y en muestras que han sido descargadas. Las muestras prístinas de $CoFe_2O_4$ presentan un espectro que se descompone

en 5 sextetos solapados debido a los diferentes entornos locales de los átomos de hierro consecuencia de la presencia de dominios ferrimagnéticos en partículas cristalinas. Se ha descrito extensamente que los iones Co^{2+} ocupan preferiblemente huecos octaédricos mientras que los iones Fe^{3+} se distribuyen entre los huecos octaédricos y tetraédricos de la estructura espinela. Siguiendo el modelo ya descrito por otros autores se han atribuido 4 señales al hierro en coordinación octaédrica y la señal que aparece a menor desplazamiento isomérico al hierro en coordinación tetraédrica. El cociente Fe(Td)/Fe(Oh) es de 0.41 que está en concordancia con los valores de una espinela parcialmente inversa.

Las muestras descargadas presentan espectros con dobletes y singletes debido a la pérdida del carácter ferrimagnético inducido por la degradación estructural propia de las reacciones de conversión. Las señales se atribuyen a la presencia de Fe^{3+} y Fe^{2+} en las muestras descargadas a $2F.mol^{-1}$, sin embargo las muestras totalmente descargadas presentan señales que se atribuyen a hierro metálico mostrando la reducción efectiva del material en la reacción de conversión. Las medidas se efectuaron en muestras tras la primera y la sexta descarga. El ensanchamiento de la señal Mössbauer tras las sucesivas descargas puede asignarse al deterioro estructural provocado a medida que se cicla el electrodo. Probablemente el modelo empleado es una aproximación sencilla a la distribución de sitios más compleja que existe en el electrodo ciclado amorfo. Las dos señales que presentan los espectros de las muestras descargadas se atribuyen a los átomos de hierro en el interior de las partículas y a los átomos de hierro en la superficie de las partículas. La pérdida progresiva de la contribución de

la señal atribuida a los átomos hierro en el interior de las partículas está correlacionada con la pérdida de capacidad durante el ciclado de carga y descarga. La preservación de dichos átomos de hierro revela ser fundamental en el mantenimiento de la capacidad durante el ciclado. Las muestras calcinadas a 800ºC mostraron una mayor preservación de la señal correspondiente a los átomos de hierro del interior de las partículas y mejor comportamiento electroquímico.

La reacción electroquímica de conversión puede ser dividida en dos procesos diferentes: un proceso faradaico que implica la reducción completa de los átomos del metal de transición y que corresponde al plató observado en el perfil galvanostático y un proceso pseudo-capacitivo relacionado con la caída de voltaje al final de la descarga. Mediante SPES se ha podido relacionar la contribución relativa de ambas componentes a la capacidad total con respecto a la cinética de carga/descarga. Se observó que la contribución de los procesos faradaicos al mantenimiento de la capacidad durante el ciclado es esencial. Dicho efecto se correlaciona con la preservación de los átomos de hierro en el interior de la partícula completamente reducidos que no contribuyen a la formación de reacciones secundarias responsables de la componente pseudo-capacitiva y por tanto de la irreversibilidad durante el ciclado galvanostático.

El análogo de níquel, $NiFe_2O_4$ ha sido sintetizado mediante un proceso sol-gel usando dos temperaturas diferentes de calcinación, 600ºC y 1000ºC. La difracción de rayos X reveló la concordancia de las

reflexiones observadas con la estructura espinela al igual que el análogo de cobalto.

La microscopía SEM mostró agregados de partículas submicrométricas para ambas muestras, con tamaños mayores de partícula conforme aumenta la temperatura de calcinación. A través de las reflexiones obtenidas en la difracción de rayos X se calculó el tamaño de partícula. Los valores han sido 74 *nm* para la muestra calcinada a 600ºC y 405 *nm* para la muestra calcinada a 1000*ºC*.

Se realizó espectroscopía Mössbauer a las muestras originales y descargadas. Se observaron dos sextetos correspondientes al Fe^{3+} en huecos octaédricos y tetraédricos en el espécimen original debido al carácter ferrimagnético de las muestras cristalinas, mientras que se observaron dos dobletes en el caso de las muestras descargadas. Las dos señales son atribuibles a los dos tipos de hierro metálico, uno en el interior de la partícula y otro en la superficie. En la muestra calcinada a 1000*ºC* la señal correspondiente al hierro superficial aparece a menor desplazamiento isomérico indicando una reducción más efectiva y menor contribución de reacciones secundarias en la superficie de las partículas. como es de esperar al ser la muestra con mayor tamaño de partícula. Además se realizaron medidas a baja temperatura con el objetivo de observar la transición del carácter superparamagnético a carácter ferrimagnético cuando se alcanza la temperatura de bloqueo y los espines dejan de moverse libremente y se sujetan a las interacciones cooperativas. El análisis de dichas temperaturas permitió correlacionar el tamaño de las nanopartículas del metal reducido con la muestra de partida y el comportamiento electroquímico. Se observe una temperatura de bloqueo más alta para muestra calcinada a 1000 °C, lo

que se relacionó con partículas de hierro reducido más grandes. La disminución significativa de la temperatura de bloqueo observada en muestras cicladas puede relacionarse con una disminución en el tamaño de las partículas nanométricas de hierro reducido.

Se han sintetizado dos tipos de fosfatos diferentes para su uso cómo cátodos de intercalación. La síntesis de un composite $Na_{1.8}FePO_4F/C$ se llevó a cabo a través de un método cerámico usando carboximetilcelulosa de sodio como precursor de sodio y para originar un residuo carbonoso durante el proceso de calcinación en atmósfera inerte. Los análisis termogravimétricos revelaron un abrupto pico de pérdida de masa en torno a los 350-450ºC que corresponde con un 25% de carbón. El ajuste del difractograma de rayos X mediante el método Rietveld confirmó la pertenencia de una muestra de elevada pureza indexable en el grupo espacial *Pbcn* del sistema ortorrómbico. Las imágenes de microscopía SEM revelaron aglomerados de partículas primarias de tamaño submicrométrico. La presencia de Fe^{2+} fue confirmada mediante espectroscopía Mössbauer.

Las muestras fueron cicladas galvanostaticamente en las celdas de sodio $Na/1MNaPF_6(\boldsymbol{PC})/Na_{1.8}FePO_4F/C$ y $Na/1MNaPF_6(\boldsymbol{EC:DEC},1:1)/Na_{1.8}FePO_4F/C$ a C/20. Aproximadamente un ión sodio es reversiblemente intercalado a un voltaje de $3V$. Los valores de capacidad obtenidos están entre 100 y 120 $mAh.g^{-1}$. Las curvas de carga-descarga mostraban una inserción adicional de sodio que han sido explicadas a través de la presencia de Fe^{3+} en la muestra original y que ha sido confirmada mediante espectroscopía Mössbauer.

La estabilidad de los valores de capacidad durante un ciclado extendido depende del electrólito y la capacidad de la celda decrece debido a la descomposición del electrolito a voltajes límites. Dicho efecto es más pronunciado cuando se usa carbonato de propileno como disolvente. Los resultados revelaron una mejor retención de la capacidad en las celdas que contenían EC:DEC como disolvente para electrolito.

Un estudio XANES *ex situ* fue llevado a cabo en electrodos de $Na_{1.8}FePO_4F/C$ parcialmente cargados a sucesivos voltajes. El desplazamiento de los espectros a altas energías durante la carga confirma la oxidación de Fe^{2+} a Fe^{3+}. Los altos desplazamientos de energía durante la carga evidencian la importancia de los disolventes de los diferentes electrolitos, remarcando la idoneidad del uso de EC:DEC como disolvente en lugar de PC.

Por otro lado se exploró la familia de cátodos con estequiometria $Na_3Fe_{2-x}Cr_x(PO_4)_3$ y sus correspondientes compuestos litiados de la serie $Li_3Fe_{2-x}Cr_x(PO_4)_3$. Los compuestos de sodio se obtuvieron mediante el proceso sol-gel, mientras que los de litio se prepararon por intercambio iónico a partir de los primeros.

Los difractogramas de rayos X de $Na_3Fe_{2-x}Cr_x(PO_4)_3$ ($0 \leq x \leq 1$) se caracterizan por reflexiones estrechas correspondientes a fases bien cristalizadas. La mayor parte de las reflexiones se indexaron en el grupo espacial *C2C* del sistema monoclínico. Sin embargo, se observan pequeños picos a aproximadamente 17º y 32º en las muestras con alto contenido en cromo ($x \geq 0.8$) que se atribuyeron a algunas de las reflexiones más intensas de la fase $Na_3Cr_3(PO_4)_4$.

Los espectros Mössbauer de las muestras de la serie $Na_3Fe_{2-x}Cr_x(PO_4)_3$ se realizaron con el fin de obtener información precisa sobre el estado de oxidación y el entorno local de los átomos de hierro. Los espectros se caracterizan por una señal doblete con valor de desplazamiento isómero correspondiente a la presencia de iones Fe^{3+}, lo que sugiere un sitio único para los átomos de hierro en la estructura. La introducción de átomos de cromo no implica cambios significativos en el perfil del espectro, aunque se detectó una disminución del desplazamiento isomérico al aumentar el contenido en cromo.

Se prepararon celdas de litio con muestras de $Na_3Fe_{2-x}Cr_x(PO_4)_3$. Durante el proceso electroquímico se produce la desinserción de Na^+ y una posterior inserción de Li^+ proveniente del electrólito. Se observó claramente que la sustitución parcial de hierro por cromo a bajos contenidos en las muestras de $Na_3Fe_{1.8}Cr_{0.2}(PO_4)_3$ y de $Na_3Fe_{1.6}Cr_{0.4}(PO_4)_3$ disminuye la polarización entre las curvas de carga y descarga, en comparación con el $Na_3Fe_2(PO_4)_3$. Entre las diversas muestras sustituidas con cromo, el $Na_3Fe_{1.8}Cr_{0.2}(PO_4)_3$ ofrece la mayor capacidad específica para la primera descarga de 88,3 $mAh.g^{-1}$. Sin embargo, estos materiales catódicos no exhiben valores altos de capacidad y una disminución rápida de la capacidad con los ciclos probablemente como consecuencia del gran tamaño Na^+ iónico en comparación con el Li^+ iónico, dando lugar a una difusión iónica pobre.

Con el fin de mejorar el comportamiento electroquímico de estos compuestos, se realizaron reacciones de intercambio iónico para sustituir los iones alcalinos. La eficiencia del proceso de intercambio iónico se comprobó por espectroscopía dispersiva de energía (EDS) que revelaron una clara disminución del contenido de sodio.

Los difractogramas de difracción de rayos X de las muestras del $Li_3Fe_{2-x}Cr_x$ $(PO_4)_3$ preparadas por intercambio iónico a partir de $Na_3Fe_{2-x}Cr_x(PO_4)_3$ han sido indexados con el grupo espacial $R\bar{3}$ del sistema romboédrico del $Li_3Fe_2(PO_4)_3$. Se observó una continua disminución de los parámetros de celda unidad conforme el contenido de cromo aumentaba, excepto para la muestra con x = 1. Dichos resultados coinciden con los del $Na_3Fe_{2-x}Cr_x(PO_4)_3$, en los cuales la sustitución parcial de hierro por el cromo no cambia la estructura cristalina y tiene un efecto reducido sobre las dimensiones de la estructura.

Para las muestras de $Na_3Fe_2(PO_4)_3$ y $Na_3Fe_{1.8}Cr_{0.2}(PO_4)_3$ los tamaños de partícula estaban en los rangos 125-750 *nm* y 200-850 *nm*, respectivamente según reveló la microscopía TEM. Para la muestra de $Li_3Fe_{1.8}Cr_{0.2}(PO_4)_3$ se observó que los bordes de las partículas eran más redondeados, en comparación con $Na_3Fe_{1.8}Cr_{0.2}(PO_4)_3$ probablemente por la agitación continua a la agitación continua a la que se someten las muestras durante el proceso de intercambio iónico.

Las muestras de $Li_3Fe_{2-x}Cr_x(PO_4)_3$ presentaron una mejora significativa en comparación con la serie $Na_3Fe_{2-x}Cr_x(PO_4)_3$ en el comportamiento electroquímico mostrando una menor polarización entre la carga y la descarga y una mayor inserción de litio durante la descarga. Dicha mejora puede ser atribuida a que la estructura en la serie $Li_3Fe_{2-x}Cr_x(PO_4)_3$ es más abierta lo que se traduce en una mayor facilidad en el proceso de inserción/deinserción de Li^+ en la estructura.

Entre las diferentes muestras sustituidas con cromo, el $Li_3Fe_{1.8}Cr_{0.2}(PO_4)_3$ presenta el mejor rendimiento. Se logran insertar hasta 1.7 Li^+ por

fórmula unidad generando una capacidad específica de 105 $mAh.g^{-1}$ para la primera descarga.

5.2 Summary

Among the conversion anodes synthesized, $NiFe_2O_4$ and $CoFe_2O_4$ spinels have been studied in more detail. The cobalt compound has been synthesized by a reverse micelles method based on the use of organic anionic stabilizing water-in-oil micelles which act as small reactors We have obtained several samples of material modifying variables such as concentration of the starting reagents (6M or 8M NaOH), different annealing temperatures (800°*C* or 1000°*C*), various surfactants (Span80 or Tween85) at different ratios of organic phase: aqueous phase (1:1 or 1:2).

X-ray diffraction patterns showed an intense set of reflections that have been indexed in the space group *Fd3m* and a good level of purity. The SEM photographs revealed agglomerates of submicronic particles in all cases. Regardless of the ratio organic phase:aqueous phase samples that were synthesized using Span80 presented primary particle size smaller than those samples synthesized using Twenn85 as the surfactant. Higher annealing temperatures lead to an increase on the primary particle size.

An important aspect to optimize the electrochemical performance of the conversion electrodes is the capacity fading during cycling. The Mössbauer spectroscopy has become a fundamental tool for understanding the processes involved in galvanostatic cycling of the samples studied. Mössbauer spectroscopy was carried out on original and discharged samples. Pristine $CoFe_2O_4$ samples exhibit a spectrum which

is decomposed into 5 sextets overlapping due to different local environments of iron atoms consequence of the presence of ferrimagnetic domains in well crystallized particles. It has been widely reported that Co^{2+} ions preferably occupy octahedral sites whereas Fe^{3+} ions are distributed among octahedral and tetrahedral sites into the spinel structure. Following the model already described by other authors 4 signals have been attributed to iron in octahedral coordination and the signal appearing at lower isomer shift to iron in tetrahedral coordination. The ratio Fe(Td)/Fe(Oh) is 0.41 which is consistent with the values of a partially inverse spinel.

The discharged samples showed spectra with doublets and singlets due to the loss of the ferrimagnetic character induced by the characteristic degradation of the conversion reactions. The signals are attributed to the presence of Fe^{3+} and Fe^{2+} in the samples discharged $2F.mol^{-1}$, however fully discharged samples showed signals attributed to metallic iron showing the effective reduction of the material in the conversion reaction. Measurements were made on samples after the first and the sixth discharge. The Mössbauer signal widens after the successive discharges due to structural deterioration of cycled electrodes. The two Mössbauer signals of the samples totally discharged were attributed to iron atoms into the core of the particles and iron atoms at the surface of the particles. The progressive loss of the contribution attributed to reduced iron atoms inside the particles core is correlated with the loss of capacity during the charge and discharge processes. The preservation of these core iron atoms seems to be essential to maintain the electrochemical capacity during cycling. The samples annealed at $800°C$

showed greater preservation of the signal corresponding to the core iron atoms and better electrochemical behavior.

The electrochemical reaction of conversion can be divided into two different processes: a faradaic process which involves the complete reduction of the transition metal atoms which corresponds to the plateau observed in the galvanostatic profile at $1V$ and a pseudo-capacitive process related to the voltage drop at the end of the discharge. Using SPES has been correlated the relative contribution of both components to the total capacity with the rate of charge/discharge processes. It was observed that the maintaining of faradaic processes contribution during cycling is essential and that this effect is correlated with the preservation of iron atoms into the core of the particle while the pseudo-capacitive component is ascribable to the possible side reactions which provoke the irreversibility during the galvanostatic cycling.

The nickel analoga $NiFe_2O_4$ was synthesized by sol-gel method using two different annealing temperatures, $600°C$ and $1000°C$. X-ray diffraction revealed the matching reflections observed with the spinel structure as the analogue of cobalt.

SEM showed aggregates of submicronic particles for both samples, with particle sizes greater with increasing annealing temperature. Through reflections obtained in the X-ray diffraction was calculated particle size. The values were 74 nm for the sample annealed at $600°C$ and 405 nm for the sample annealed at $1000°C$.

Mössbauer spectroscopy was performed on pristine samples and discharged samples. The original specimen showed two sextets

corresponding to Fe^{3+} in octahedral and tetrahedral sites due to the ferrimagnetic nature of the well crystallized domains in the sample. For discharged samples two doublets were observed. The two signals are attributable to the two types of metallic iron, as was described for $CoFe_2O_4$, one into the core of the particle and one at the particle surface. In the sample annealed at 1000°*C* the signal which corresponds to surface atoms appears at a lower isomer shift indicating a more effective reduction and less prospering of secondary reactions at the surface of the particles as expected for samples with larger primary particle size. In addition measurements were performed at low temperature in order to observe the ferrimagnetic-superparamagnetic transition when reaching the blocking temperature. At this temperature the spins no longer move freely and are subject to cooperative interactions. The Mössbauer analysis at these temperatures allowed correlating the size of the nanoparticles of the reduced metal with the starting sample and the electrochemical behavior. Observing a blocking temperature higher for sample calcined at 1000 ° C, which was associated with larger reduced iron particles. The significant reduction in the blocking temperature observed in cycled samples may be related to a decrease in the size of nanometric particles of reduced iron.

.

Two types of phosphate compounds were synthesized for their evaluation as intercalation cathodes. A first compound - $Na_{1.8}FePO_4F$ – was uses in sodium test cells. The synthesis was carried out by ceramic methods using sodium carboxymethylcellulose as a sodium precursor and to originate *in-situ* carbon during the annealing process. Thermogravimetric analysis revealed an abrupt peak due to the mass

loss at 350-450°*C* which corresponds to a 25% carbon content. X-ray diffraction has been refined by the Rietveld method confirming the indexing of the fluorophosphate to the orthorhombic space group *Pbcn*. SEM revealed agglomerates of primary particles of submicronic size. The presence of Fe^{2+} was confirmed by Mössbauer spectroscopy.

The samples were cycled galvanostatically in sodium cells Na/1MNaPF_6(***PC***)/$Na_{1.8}FePO_4F$/C and Na/1MNaPF_6(***EC:DEC***,1:1)/$Na_{1.8}FePO_4F$/C at C/20. *Circa* one sodium is reversibly intercalated at a voltage of 3*V* showing capacity values of 100 and 120 $mAh.g^{-1}$. The stability of the cell depends on the electrolyte and the cell capacity decreases due to decomposition of the electrolyte at end voltages. This effect is more pronounced when using for PC as a solvent. The results revealed better capacity retention in cells containing EC: DEC as electrolyte solvent.

The charge-discharge curves showed additional insertion of sodium which has been explained through the presence of Fe^{3+} in the original sample and it has been confirmed by Mössbauer spectroscopy.

Ex-situ XANES study was conducted in the different cells at different cut-off voltages. The displacement of the spectra at high energies during charging confirms the oxidation of Fe^{2+} to Fe^{3+}. The high energy displacements during charging demonstrate the importance of the different solvents for the electrolyte highlighting the suitability of the use of EC: DEC as solvent for the electrolyte instead of PC.

On the other hand it was explored the family of cathode material with stoichiometry $Na_3Fe_{2-x}Cr_x(PO_4)_3$ and $Li_3Fe_{2-x}Cr_x(PO_4)_3$ by sol-gel and ion exchange, respectively.

The X-ray diffraction patterns of $Na_3Fe_{2-x}Cr_x(PO_4)_3$ ($0 \leq x \leq 1$) are characterized by narrow reflections for well-crystallized phases. Most of the reflections could be indexed with the monoclinic space group of $Na_3Fe_2(PO_4)_3$, *C2C*. However, the impurities are clearly evident by some weak peaks at approx. 17 º and 32 º in the samples with x = 0.8 and 1.0, attributable to some of the most intense reflections of $Na_3Cr_3(PO_4)_4$.

Mössbauer spectra of $Na_3Fe_{2-x}Cr_x(PO_4)_3$ samples were performed in order to obtain accurate information on the oxidation state and the local environment of iron atoms. The spectra are characterized by a doublet signal with isomer shift value corresponding to the presence of Fe^{3+} ions, suggesting a single site for the iron atoms in the structure. The introduction of chromium atoms does not involve significant changes in the profile of the spectrum.

$Na_3Fe_{2-x}Cr_x(PO_4)_3$ cells were assembled versus lithium. During the electrochemical process Na^+ is deintercalated and subsequent insertion of Li^+ from the electrolyte is produced. Was clearly observed that samples containing low content of chromium as $Na_3Fe_{1.8}Cr_{0.2}(PO_4)_3$ and $Na_3Fe_{1.6}Cr_{0.4}$ $(PO_4)_3$ decreases the hysteresis between the charge and discharge curves as compared with $Na_3Fe_2(PO_4)_3$. Among the various Cr-substituted samples, $Na_3Fe_{1.8}Cr_{0.2}(PO_4)_3$ offers the highest value of specific capacity for the first discharge (88.3 $mAh.g^{-1}$). However, these cathode materials do not exhibit high values of capacity and a rapid decrease of capacity is shown after few cycles. This fact could be a result of the larger size of Na^+ ion compared to Li^+ ion, leading to poor ion diffusion.

In order to improve the electrochemical behavior of these compounds, ion exchange reactions were performed to replace the alkali ions. The efficiency of ion exchange process was checked by energy dispersive spectroscopy (EDS) that showed a clear decrease in sodium content.

The X-ray diffraction patterns of the samples $Li_3Fe_{2-x}Cr_x(PO_4)_3$ prepared by ion exchange from $Na_3Fe_{2-x}Cr_x(PO_4)_3$ have been indexed with the space group $R\bar{3}$ of the rombohedral phase $Li_3Fe_2(PO_4)_3$. There was a continuous decrease in the unit cell parameters as the chromium content increased, except for the sample with x = 1. These results agree with those of $Na_3Fe_{2-x}Cr_x(PO_4)_3$, in which the partial substitution of iron by chromium does not change the crystal structure and has a small effect on the dimensions of the structure.

For the samples $Na_3Fe_2(PO_4)_3$ and $Na_3Fe_{1.8}Cr_{0.2}(PO_4)_3$ the particle sizes were in the ranges of 125-750 *nm* and 200-850 *nm*, respectively as revealed by TEM microscopy. For the sample of $Li_3Fe_{1.8}Cr_{0.2}(PO_4)_3$ was observed that the edges of the particles were more rounded, compared with $Na_3Fe_{1.8}Cr_{0.2}(PO_4)_3$ probably produced by the continuous stirring during the ion exchange process.

Samples $Li_3Fe_{2-x}Cr_x(PO_4)_3$ showed a significant improvement as compared with the series $Na_3Fe_{2-x}Cr_x(PO_4)_3$ in the electrochemical behavior showing less polarization between charge and discharge and further lithium insertion during discharge. The improvement can be ascribed to the fact that the structure in the series $Li_3Fe_{2-x}Cr_x(PO_4)_3$ is more open resulting in greater insertion/deinserción process of Li^+ into the structure.

Among the different samples replaced with chromium $Li_3Fe_{1.8}Cr_{0.2}(PO_4)_3$ has the best performance. It managed to add up to 1.7 Li^+ per formula unit generating a specific capacity of 105 $mAh.g^{-1}$ for the first discharge.

5.3 Conclusiones finales

Las conclusiones generales que hemos podido obtener a la vista de los resultados presentados y discutidos en esta memoria son las siguientes:

1. Ha sido posible la obtención de $CoFe_2O_4$ con alto nivel de pureza y morfología adecuada a través del método de micelas inversas. La selección apropiada de las condiciones de síntesis, es decir, el tipo de agente tensioactivo, la relación entre fase acuosa y fase orgánica, y la temperatura de calcinado del precursor conduce a materiales con optimizado rendimiento electroquímico optimizado.

2. Los resultados de espectroscopia Mössbauer de ^{57}Fe han revelado el carácter ferrimagnético de la muestra original. Los perfiles asimétricos son característicos del complejo entorno local de los átomos de hierro, rodeados por un número diferente de cobalto y hierro vecinos. Los espectros Mössbauer registrados para electrodos ciclados evidenciaban una disminución significativa de la población de átomos de Fe^0 en el interior de las partículas para las muestras que presentan un rendimiento electroquímico pobre. Se desprende del estudio la correlación de los átomos de hierro en el interior de las partículas con la reversibilidad de la reacción redox durante el ciclado y por lo tanto, su contribución a la componente faradaica de la carga almacenada.

3. La realización de SPES a diferentes velocidades de barrido permitió diferenciar las componentes faradaica y capacitiva de la capacidad total del material estudiado. La muestra sintetizada a 1000ºC presenta una contribución significativa capacitiva que permite una mejor capacidad de retención a tasas intermedias. Sin embargo, la gran contribución faradaica para la muestra preparada a 800°*C* contrarresta este efecto y los valores de capacidad son en general más altos (*ca.* 600 $mAh.g^{-1}$) para un mayor número de ciclos.

4. La muestra de $CoFe_2O_4$ preparada mediante el uso de Span 80 como un agente surfactante, una relación 1:1 de fases orgánica:acuosa calcinada a 800º*C* durante 15 horas ha mostrado los valores más altos de capacidad (614 $mAh.g^{-1}$) después de un gran número de ciclos convirtiéndolo en un posible candidato para su uso cómo ánodo de conversión en baterías de ión litio.

5. Las muestras de $NiFe_2O_4$ han sido preparadas mediante sol-gel que ha demostrado ser una metodología bajo coste mediante la cual se consigue una morfología particular de aglomerados, en los cuales las partículas primarias están interconectadas para asegurar una buena conductividad eléctrica y resistencia mecánica para un largo ciclado electroquímico. Todas las muestras revelaron morfología similar discordando en tamaño de partículas primarias que aumentó en el caso de las muestras calcinadas a mayor temperatura.

6. Los espectros Mössbauer de ^{57}Fe de electrodos descargados en celdas de litio de las muestras $NiFe_2O_4$ mostraron la efectividad de la reducción del hierro en el proceso de descarga. Frente a los espectros de las muestras prístinas de $NiFe_2O_4$ con carácter ferrimagnético, las muestras litiadas mostraron relajación superparamagnética.

7. Los espectros Mössbauer registrados a 12 *K* demostraron la recuperación del carácter ferrimagnético. La asignación de los sextetos aparecidos bajo la temperatura de bloqueo a átomos de hierro superficiales e interiores se verifica por la concordancia de sus contribuciones con la de los dobletes superparamagnéticos registrados a temperatura ambiente. De acuerdo con la contribución el diámetro de la partícula hierro metálico se calculó que era aproximadamente. 5 nm.

8. Se ha mostrado una nueva ruta de preparación de Na_2FePO_4F/C composite a través del uso de carboximetilcelulosa de sodio como doble precursor. En primer lugar, siendo la fuente de sodio y además como generador del carbón *in situ* durante la calcinación de la muestra.

9. El material resultante contiene el fluorofosfato en su forma ortorrómbica ya conocida, siendo aprox. 10% sub-estequimétrico en sodio debido a una reducción parcial de hierro.

10. El mecanismo de oxidación del hierro en Na_2FePO_4F se realizó sobre muestras prístinas y descargadas en celdas de sodio a diferentes voltajes. Para ello se empleó la espectroscopia XANES *ex situ* basada en la absorción de rayos X cercano al umbral de emisión. Se observó un desplazamiento de los espectros a altas energías durante la carga confirmando la oxidación de Fe^{2+} a Fe^{3+}. Los cambios estructurales de la $Na_{1.8}FePO_4F$ a NaFePO4F en carga, y luego a Na_2FePO_4F en la posterior descarga son pequeñas generando tan sólo ligeros cambios en la intensidad de la línea blanca.

11. Los espectros XANES también mostraron altos desplazamientos de energía durante la carga evidenciando la importancia de la elección del disolvente adecuado para la preparación del electrolito. Se concluyó la idoneidad del uso de EC:DEC como disolvente para electrolito en lugar de PC. Los valores de capacidad y la retención de la misma son asimismo mayores para las celdas de sodio utilizando EC:DEC como disolvente y $NaPF_6$ como sal de electrólito.

12. Una nueva familia de materiales catódicos para baterías de litio con estequiometría nominal $Li_3Fe_{2-x}Cr_x(PO_4)_3$ ($0 \leq x \leq 1$), han sido sintetizados a través de reacciones de intercambio iónico usando la familia $Na_3Fe_{2-x}Cr_x(PO_4)_3$ como precursores. El proceso de intercambio iónico conlleva una transición estructural de una fase monoclínica a una fase romboédrica con una estructura más abierta que facilita la difusión de litio. La sustitución de cromo se reflejó en una disminución en los

parámetros de celda tanto en las fases de sodio como en las fases de litio.

13. La sustitución parcial con un bajo contenido de cromo mejoró el rendimiento electroquímico de las muestras $Li_3Fe_{2-x}Cr_x(PO_4)_3$. La muestra $Li_3Fe_{1.8}Cr_{0.2}(PO_4)_3$ es capaz de insertar de manera reversible, hasta 1,7 iones de Li^+ por formula unidad generando una capacidad específica de 105 $mAh.g^{-1}$ tras la primera descarga.

Las conclusiones 1, 2 ,3 y 4 se desprenden de las publicaciones expuestas en los puntos 2.1 y 2.3 de la presente memoria.

Las conclusiones 5 y 6 se desprenden de las publicaciones expuestas en el punto 2.2.

Las conclusiones 7, 8, 9, 10 y 11 se desprenden de las publicaciones expuestas en el apartado 3.1 de la presente memoria.

Las conclusiones 12 y 13 se desprenden de las publicaciones expuestas en el apartado 3.2 de la presente memoria.

4.4 Final conclusions

The general conclusions that we have obtained from the results presented and discussed in this report are:

1. It has been possible to obtain $CoFe_2O_4$ with high purity and controlled morphology through the reverse micelle method. Adequate selection of the synthesis conditions, *i.e.*, the type of surfactant, the ratio aqueous phase: organic phase, and the annealing temperature of the precursor materials resulted in optimized electrochemical performance.

2. ^{57}Fe Mössbauer spectroscopy revealed a ferrimagnetic pattern due to the nature of the pristine material, and nonsymmetrical profiles resulting from the complex local environment of iron atoms surrounded by a different number of cobalt and iron neighbors. Mössbauer spectra recorded for discharged electrodes evidenced a significant decrease in the population of core Fe^0 atoms for samples which exhibit a poor electrochemical performance. The Mössbauer study shows the correlation of the core iron atoms in with the reversibility of the redox reaction during cycling and thus their contribution to the faradaic component of the stored charge.

3. SPES performed at different rates allowed the differentiation of faradaic and capacitive components of the total capacity for $CoFe_2O_4$ material. The sample synthesized at $1000°C$ presents a significant capacitive contribution which allows a better retention of the capacity at intermediate rates. However, the

major faradaic contribution to the capacity of the sample annealed at 800°*C* counteracts this effect and the capacity values are generally higher (ca. 600 $mAh.g^{-1}$) for a greater number of cycles.

4. $CoFe_2O_4$ sample prepared using Span 80 as a surfactant, at 1:1 ratio of organic:aqueous phase and annealed at 800°*C* for 15 hours showed the highest values of capacity (614 $mAh.g^{-1}$) after a large number of cycles making it a possible candidate for its use as conversion anode in lithium ion batteries.

5. $NiFe_2O_4$ samples have been prepared by sol-gel method which is a low cost methodology. A particular morphology of agglomerates was achieved wherein the primary particles are interconnected to ensure good electrical conductivity and mechanical strength for a long electrochemical cycling. All samples showed similar morphology diverging in primary particle size, which increased in the case of the samples annealed at higher temperature.

6. ^{57}Fe Mössbauer spectra for discharged electrodes of $NiFe_2O_4$ in lithium cells showed the effectiveness of the reduction of iron during the discharge process as evidenced by the superparamagnetic relaxation observed in the spectrum.

7. Mössbauer spectra recorded at 12K showed the recovery of the ferrimagnetic character. The sextet contribution of surface and core atoms is in good agreement with those of the superparamagnetic doublets recorded at room temperature.

According to the contribution values the diameter of the metallic reduced particle was calculated to be *ca*. 5 nm.

8. The Na_2FePO_4F/C composite has been successfully synthesized by exploring a new route that uses sodium carboxymethylcellulose as a double precursor: Sodium source and *in-situ* generating carbon during the annealing process.

9. The resulting fluorophosphate material was indexed in its known orthorhombic form, being approx. 10% sodium sub-stoichiometric due to a partial reduction of iron.

10. Local structures discharged electrodes of $Na_{1.8}FePO_4F$ at different voltages in sodium cells were studied using *ex-situ* XANES showing a shift of the spectra at high energies during charging confirming the oxidation of Fe^{2+} to Fe^{3+}. Structural changes in the transition of $Na_{1.8}FePO_4F$ to $NaFePO_4F$ when charging, and then to Na_2FePO_4F at the subsequent discharge are small producing only slight changes in the intensity of XANES white line.

11. XANES studies also revealed high energy displacements during charging showing the importance of the solvents in different electrolytes, highlighting suitability of the use of EC: DEC as solvent for the electrolyte in place of PC. Values of capacity and its retention area higher for sodium cells using EC: DEC as a solvent and $NaPF_6$ salt as electrolyte.

12. A new family of cathode materials with stoichiometry $Li_3Fe_{2-x}Cr_x(PO_4)_3$ ($0 \leq x \leq 1$) have been successfully prepared through ion exchange reactions using the family $Na_3Fe_{2-x}Cr_x(PO_4)_3$ as precursors. The chemical exchange process involves a structural transition from a monoclinic to a rhombohedral phase with an open structure that facilitates the diffusion of lithium. The replacement of chromium was evidenced by a decrease in cell parameters in both phases of sodium as in the phases of lithium.

13. The partial substitution with a low content of chromium improved the electrochemical performance of samples $Li_3Fe_{2-x}Cr_x(PO_4)_3$. The sample $Li_3Fe_{1.8}Cr_{0.2}(PO_4)_3$ is able to insert reversibly, up to 1.7 Li^+ ions per formula unit generating a specific capacity of 105 $mAh.g^{-1}$ after the first discharge.

Conclusions 1, 2, 3 and 4 are derived from the publications described at 2.1 and 2.3 chapters.

Conclusions 5, 6, and 7 are derived from the publications described at 2.2 chapter.

Conclusions 8, 9, 10 and 11 are derived from the publications described at 3.1 chapter.

Conclusions 12 and 13 are derived from the publications described at 3.2 chapter.

Capítulo 5

Otras aportaciones científicas

A continuación se exponen los abstracts, a modo de resumen de varias publicaciones adicionales. Dichos trabajos han sido descartados para constituir el cuerpo de la tesis por haber sido desarrolladas en el periodo de formación del doctorado o por ser pequeñas colaboraciones. Sin embargo todas están estrechamente relacionadas con la tesis que se ha desarrollado y completan los estudios expuestos en el capítulo 2 de la presente memoria.

5.1 Sol–gel preparation of cobalt manganese mixed oxides for their use as electrode materials in lithium cells

P. Lavela, J.L. Tirado, C. Vidal-Abarca*

Laboratorio de Química Inorgánica, Universidad de Córdoba, Campus de Rabanales, 14071 Córdoba, Spain

Electrochimica Acta 52 (2007) 7986–7995

Abstract

An ethanol dehydration procedure has been used to precipitate gel-like citrate precursors containing cobalt and manganese transition metal ions. Further annealing led to the $Mn_xCo_{3-x}O_4$ spinel oxide series (x: 1, 1.5, 2, 3). Annealing temperature and treatment time were also evaluated to optimize the performance of the oxides as active electrode materials in lithium cells. The manganese–cobalt mixed oxides obtained by this procedure were cubic or tetragonal phases depending on the cobalt content. SEM images showed spherical macroporous aggregates for $MnCo_2O_4$ and hollow spheres for manganese oxides. The galvanostatic cycling of lithium cells assembled with these materials demonstrated a simultaneous reduction of cobalt and manganese during the first discharge and separation of cobalt- and manganese-based products on further cycling. As compared with binary manganese oxides, a notorious electrochemical improvement was observed in the mixed oxides. This behavior is a consequence of the synergistic effect of both transition metal elements, associated with the in-situ formation of a nanocomposite electrode material when cobalt is introduced in the manganese oxide composition. Values higher than 400 $mAh.g^{-1}$ were sustained after 50 cycles for $MnCo_2O_4$.

**corresponding author*

5.2 Cobalt Oxide Nanoparticles Prepared from Reverse Micelles as High-Capacity Electrode Materials for Li-Ion Cells

C. Vidal-Abarca, P. Lavela*, and J. L. Tirado

Laboratorio de Química Inorgánica, Universidad de Córdoba, Edificio Marie Curie, Campus de Rabanales, 14071 Córdoba, Spain

Electrochemical and Solid-State Letters, **11** (11) A198-A201(2008)

Abstract

A reverse-micelles procedure followed by annealing is developed to prepare Co_3O_4 materials with controlled particle size and microstructure. The single-phase products occur as submicrometric particles that interconnect into larger aggregates with spherical shape and no porosity. Two types of electrochemical response are found in lithium cells depending on annealing time and temperature. Reversible capacities of up to ca. 800 mAh g−1 are observed in intermediate annealing, while lower capacities and better capacity retention are found for short treatments at 600°C. These differences are related to the changes in charge-transfer resistance.

**corresponding author*

5.3 On the use of the reverse micelles synthesis of nanomaterials for lithium-ion batteries

María José Aragón & Pedro Lavela & Bernardo León &Carlos Pérez-Vicente & José Luis Tirado & Candela Vidal-Abarca*

J Solid State Electrochem (2010) 14:1749–1753

Abstract

The reverse micelles procedure is a convenient route for the preparation of nanomaterials. Chemical reactions in aqueous media are carried out within a

restricted volume, limited by the array of surfactant molecules. The versatility of this technique allows its use in the preparation of different electrode materials for lithium-ion batteries. The thermolysis of the reagents in aqueous solution in the micellar volume by contact with hot kerosene allows the preparation of $LiCoO_2$, $LiMn_2O_4$, and $LiNi_{0.5}Mn_{1.5}O_4$ fine powders with good electrochemical behavior. The conversion electrode material Co_3O_4 was prepared with controlled particle size and microstructure by a precipitation reaction in the micellar volume. The electrochemical response found in lithium cells was excellent after optimizing the annealing procedure. Cobalt and iron oxalate nanoribbons and submicrometric rhombic

particles of manganese carbonate have been prepared by the reverse micelles procedure and partially behave as conversion oxide electrodes. The electrochemical reaction with lithium of these new oxysalt materials takes place by a different conversion reaction than the corresponding oxide, and a surface capacitive contribution has also been detected.

**corresponding author*

5.4 Unfolding the role of iron in Li-ion conversion electrode materials by ^{57}Fe Mössbauer spectroscopy

José L. Tirado · Pedro Lavela · Carlos Pérez Vicente · Bernardo León · Candela Vidal-Abarca*

Hyperfine Interact

DOI 10.1007/s10751-011-0421-6

Abstract

^{57}Fe Mössbauer spectroscopy is particularly useful in the study of oxide and

oxalate conversion anode materials for Li-ion batteries. After reduction in lithium test cells, all these materials showed Mössbauer spectra ascribable to iron atoms in two different environments with superparamagnetic relaxation. The spectra recorded at 12 K revealed the ferromagnetic character in agreement with particle sizes of ca. 5 nm. The two types of iron can be ascribed then to surface and core atoms. Core iron atoms play an important role to retain high faradic capacity values for a large number of cycles. These atoms are preserved from irreversible reactions with the electrolyte and hence they promote a high reversibility and rate capability.

**corresponding author*

Capítulo 6

Trabajo pendiente de publicación

En la actualidad se están desarrollando paralelamente varios trabajos de los cuales se están obteniendo resultados positivos para su posible publicación.

Dichos trabajos se enmarcarían dentro del capítulo 3 de la presente memoria ya que se tratan de fosfatos para su uso como cátodos de inserción. A continuación se expone un breve resumen de los resultados que se desprenden de dichos trabajos.

6.1 Electrochemical performance of the lithium insertion in $Mn_{1-x}Co_xTi_2(PO_4)_3/C$ composites (x= 0, 0.25, and 0.5) as electrode material for lithium batteries.

Abstract

A number of $Mn_{1-x}Co_xTi_2(PO_4)_3/C$ composites with x= 0, 0.25, and 0.5 have been examined as electrode materials for lithium batteries. A solid solution was observed in the whole range of substitution of manganese by cobalt. $Co_{0.50}Ti_2(PO_4)_3$ is characterized by a high capacity value of 183.85 $mAh.g^{-1}$ after the first discharge which is above the theoretical capacity for Ti^{4+}/Ti^{3+} reduction. Irreversible cobalt reduction may justify the progressive capacity fading. In turn, the substitution by manganese enhances the cycling stability by avoiding the irreversible manganese reduction at the lower cut off voltage. Capacities of 110 $mAh.g^{-1}$ were kept after 40 cycles for the cobalt compound.

6.2 In-situ X-ray diffraction study of the electrochemical insertion in $Mg_{0.5}Ti_2(PO_4)_3$ as electrode material for lithium and sodium batteries.

Abstract

Lithium and sodium insertion has been evaluated on $Mg_{0.5}Ti_2(PO_4)_3$. ^{31}P MAS NMR spectrum revealed distinct local environments for phosphorous atoms, which were ascribed to the exchange of Mg and Ti atoms between M_1 and M_2 sites. The *in-situ* XRD patterns recorded during the first cycle evidenced a solid solution system. The cell volume remained constant while M_1 sites were filled. Otherwise, cell parameters monotonically increased when the M_2 sites are occupied by the incoming lithium ions. The high reversibility of the deinsertion process led to the recovery of the initial cell parameters at the end of the charge. The lithium cell delivered 119 mAh/g after the first discharge and values as high as 110 mAh/g were kept after 15 cycles. Moreover, the capability of inserting sodium ions was demonstrated, although a loss of capacity was inevitable recording 97 mAh/g for the first discharge.

6.3. Application of transition metal phosphates Nasicon as electrodes for lithium batteries

Abstract

The transition metal phosphates with Nasicon-type structure presents interconnected empty cavities that allow the diffusion of alkaline ions inside. We have recently shown that the substitution of chromium in Li_3Fe_2 (PO_4) $_3$ has beneficial consequences for the behavior of this phosphate as an electrode in lithium batteries. $Li_{1+x}Ti_{2x}Fe_x$ (PO_4) $_3$ ($0 \leq x \leq 0.4$) series have been prepared in order to determine the influence of partial substitution of titanium by iron, maintaining the rhombohedral structure, on the electrochemical performance of the reversible insertion of lithium . To improve the electrical conductivity of the materials was generated containing carbon in-situ using citric acid during the synthesis.

The Rietveld refinement of X-ray diffractograms show a main phase rhombohedral (sg: R-3c). The gradual replacement of Ti by Fe induces a phase transformation to orthorhombic (sg: Pbca). The ^{13}P NMR spectra of iron-substituted samples revealed changes in the local environment of the atom probe.

The profiles of the derivative curves shows that substitution causes a reduction signal at 2.45 V and intense closer to x = 0.2. Higher iron content induces an increased extension of the set voltage to 2.8 V while the reduction to 2.5 V extends over several small peaks between 2.2 and 2.5 V. The symmetry of the anodic and cathodic curves shows the high reversibility of the process. Samples with x = 0.2 and 0.3 of iron

contents showed higher capacity than the unsubstituted compound during the cycling of the cell under various kinetics.